LBNL-49515

ERNEST ORLANDO LAWRENCE
BERKELEY NATIONAL LABORATORY

Dynamics of Electrons Photoinjected into Organic Semiconductors and Aromatic-Metal Interfaces

Kelly J. Gaffney

Chemical Sciences Division

December 2001

Ph.D. Thesis

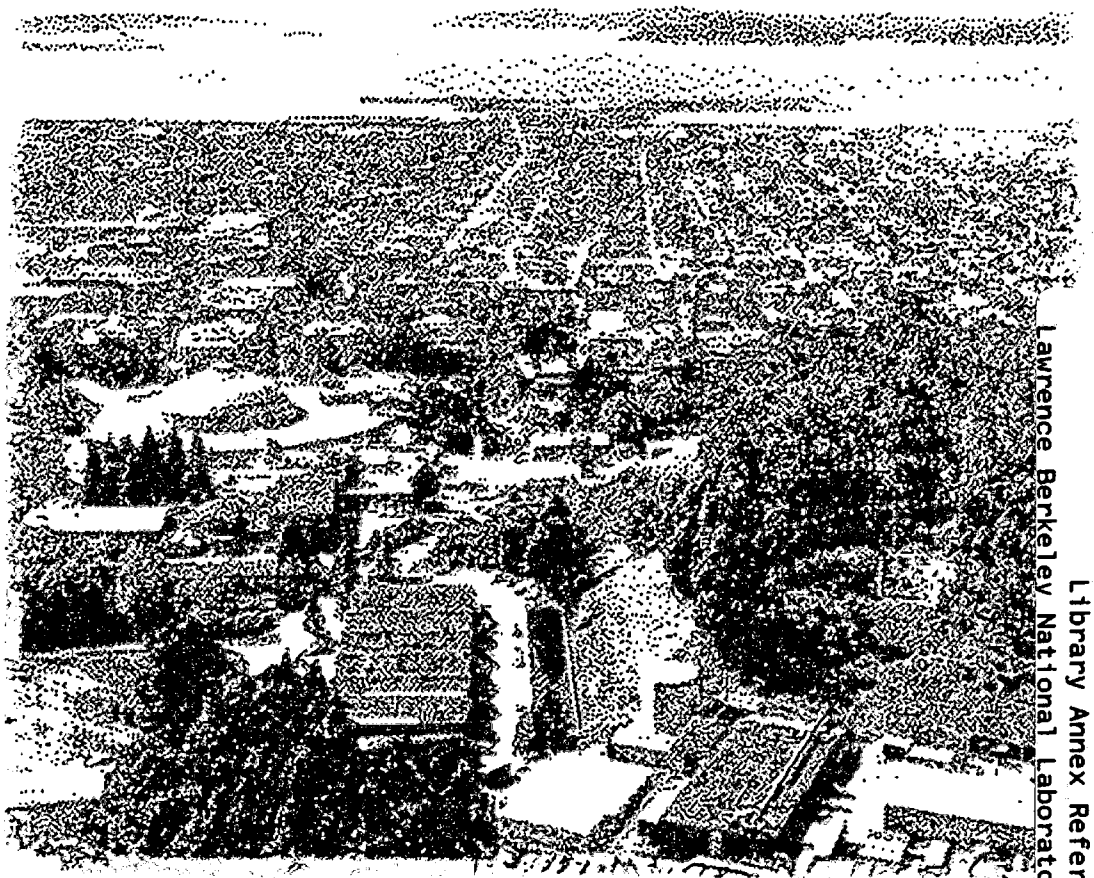

DISCLAIMER

LBNL-49515

Dynamics of Electrons Photoinjected into Organic Semiconductors and Aromatic-Metal Interfaces

Kelly Joseph Gaffney
Ph.D. Thesis

Department of Chemistry
University of California, Berkeley

and

Chemical Sciences Division
Ernest Orlando Lawrence Berkeley National Laboratory
University of California
Berkeley, CA 94720

December 2001

This work was supported by the Director, Office of Science, Office of Basic Energy Sciences, Chemical Sciences Division, of the U.S. Department of Energy under Contract No. DE-AC03-76SF00098.

Abstract

Dynamics of Electrons Photoinjected into Organic Semiconductors at Aromatic-Metal Interfaces

by

Kelly Joseph Gaffney

Doctor of Philosophy in Chemistry

University of California at Berkeley

Professor Charles B. Harris, Chair

The dynamics of electrons at aromatic-metal interfaces have been investigated with time and angle resolved two photon photoemission. The layer by layer evolution of the image potential state energies and dynamics have been measured for benzene, naphthalene, and anthracene physisorbed on a Ag(111) surface. The binding energies and lifetimes of the image potential states for anthracene differ significantly from those for benzene and naphthalene. These differences demonstrate the tremendous variation in the coupling between the image potential and the electron affinity levels of anthracene, and those for benzene and naphthalene. Firstly, the binding energies at the benzene/Ag(111) and the naphthalene/Ag(111) interfaces exceed those of the anthracene/Ag(111) interface, even though anthracene has a larger electron affinity than naphthalene. Secondly, the 1.1 picosecond lifetime for the $n = 1$ image potential state for a bilayer of anthracene exceeds the $n = 1$ lifetime for a bilayer of naphthalene by over an order of magnitude. Theoretical calculations demonstrate that the transition from a near resonant to a non-resonant interaction between the image potential and the adsorbate electron affinity levels results in the significant variation in binding energies and lifetimes for these interfaces.

The dynamics of electron localization have also been measured for a bilayer of anthracene on Ag(111). A series of three localized peaks appear in the kinetic energy spectra and have been attributed to a a vibronic progression. This series of peaks results from vibrational excitation during electron photoemission, not electron localization. The localized peaks all possess the same parallel momentum independent population dynamics,

while the delocalized image potential states exhibit strong parallel momentum dependent population dynamics. The momentum dependence of the dynamics have been attributed to energy dependent rates of localization. In addition to population dynamics, the energies and widths of the localized peaks have time dependence. The localized peaks narrow and shift to lower kinetic energies with increasing time delay. The magnitude and time scale of the energetic shift in the localized peak position, as well as the presence of the vibronic progression, have been utilized in a theoretical description of the delocalized state localization dynamics. This analysis indicates that electron localization occurs adiabatically and involves both the reorganization of low energy lattice and high energy molecular vibrations.

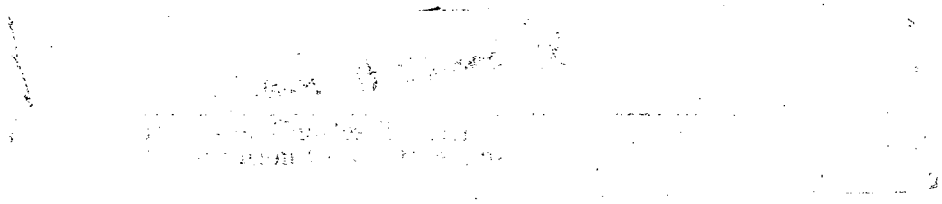

Dynamics of Electrons Photoinjected into Organic Semiconductors and Aromatic-Metal Interfaces

by

Kelly Joseph Gaffney

Contents

List of Figures

List of Tables

Acknowledgements

I wish to thank family, friends, and colleagues for their assistance in the completion of my doctoral thesis. My advisor, Charles Harris, has stimulated my intellectual growth as a scientist by emphasizing conceptual understanding over technical expertise. I would also like to thank him for his patience. The work of my thesis represents the continuation and extension of the work of Jason McNeill and Nien-Hui Ge. Their contributions do not go unappreciated. Chung Wong and I matured as scientists together. Chung guided my growth as an experimentalist when I most needed assistance, for which I will always be indebted. I could not have chosen more agreeable colleagues than Simon Liu and André Miller. Paul Szymanski, Sean Garrett-Roe, and Ilya Bezel have all proven to be conscientious and helpful contributor to group research. Ken Kotz has proven to be a valued friend, as well as a coworker. Haw Yang provided a daily reminder of the boundless potential of talent, driven by hard work and intellectual curiosity. I have learned from all of my close collaborators in the past and look forward to doing so in the future.

I dedicate my thesis to my wife, C.J. Hafner. I could not have endured the frustration and insecurity of research without her support. My sister Shannon and brother Ash helped C.J. and I make Oakland our home. I cannot image being here without them. I wish to thank my parents for stimulating and supporting my intellectual curiosity. I wish my father had lived to see me graduate. I would also like to thank the most recent additions to the family, my daughter Kathleen and my niece Uma. I embrace the joy and changed priorities you have brought to my life.

This work was supported by the Director, Office of Science, Office of Basic Energy Sciences, Chemical Sciences Division of the U.S. Department of Energy, under Contract No. DE-AC03-76SF00098. The authors acknowledge NSF support for specialized equipment used in the experiments described herein.

Chapter 1

Introduction

The dynamics of electronic excited states influence a wide range of fundamental and technologically significant processes at interfaces. Electro- and photochemical reactions [1–11] and the efficient function of electronic devices [12–21] depend critically on the energetic and dynamic properties of electrons at interfaces. This diverse range of applications rely on two important fundamental events: the injection of an electron from a conductor into a molecular adsorbate and the dynamic response of the molecular material to the injected electron.

Electron injection can be thought of as a heterogeneous electron transfer. The efficiency of the transfer depends critically on the interfacial electronic structure, with a few features being of particular importance. These include (1) the energy difference between the metal electron donor and the molecular electron acceptor, (2) the strength of the coupling between the donor and the acceptor, (3) the chemical interaction between the adsorbate and substrate, and (4) the interfacial image potential and image potential states. While the first two issue influence the rate of all electron transfer reactions, the latter two reflect the unique nature of electron transfer reactions at interfaces.

The characterization of electron injection must begin with the experimental investigation of the interfacial electronic structure. The important energy levels involve the valence and conduction bands of the metal and molecular adsorbate. These can be alternatively thought of as the highest occupied and lowest unoccupied molecular orbitals, commonly termed the HOMO and the LUMO. The relevant experimental measures of these properties are the ionization potential and the electron affinity. The energy spacing between the valence band of the substrate and the conduction band of the adsorbate determines the

energetic barrier to charge injection, while the coupling between these bands can greatly influence the rate of injection. For molecules that chemically adsorb to the substrate, the HOMO and LUMO that result from the chemisorption may become the relevant donor and acceptor states for electron injection, with electronic properties quite distinct from those of the bulk materials joined at the interface. For physically adsorbed systems the electronic structure of the adsorbate and substrate often have only a limited influence on one another. Under these circumstances the electronic properties change abruptly from those of the substrate to those of the adsorbate. For both physi- and chemisorbed systems, the image potential will stabilize the interfacial electron affinity levels and ionization potentials, reducing the energy spacing between the donor and acceptor states.

While electron injection initiates a variety of processes at interfaces, the response of the adsorbate to the excess electron will influence the energy, lifetime, effective mass, and spatial extent of the excited electron. The interdependence of the electronic and nuclear dynamics has a profound influence on electron transport and electron stimulated chemistry at interfaces. The presence of the electron will distort the nuclear coordinates of the adsorbate layer, which can lead to a layer phase transition, dynamic electron localization, and molecular bond dissociation.

The time scales for the nuclear response to an injected electron can be estimated from the period of the relevant vibrational motions of the molecules and the lattice. These range from 10 femtoseconds for high frequency intramolecular vibration to a few picoseconds for acoustic phonons. The electronic excited state lifetimes also significantly influence the observed dynamics. The rate of electron transfer back to the metal substrate determines the electronic lifetime and also ranges from a few femtoseconds to multiple picoseconds.

The influence of interfacial electronic structure on electron injection and the dynamic response of an adsorbate layer to an injected electron represent the phenomenological emphasis of the present investigation. The desire to understand how these events manifest themselves in photochemistry and molecular electronics led to the investigation of aromatic adsorbates on a metal surface. Benzene, naphthalene, and anthracene provided a series of aromatic molecules with which to study the influence of the adsorbate electronic states on the interfacial electronic structure. By choosing the inert substrate Ag(111), this influence could be investigated without the complicating influence of adsorbate chemisorption. These studies utilized time and angle resolved two photon photoemission (TPPE) as the primary experimental tool. TPPE provides a versatile experimental technique for the study of both

interfacial electronic structure and electron dynamics. The value of angle resolved TPPE derives largely from its ability to interrogate both the occupied valence bands and unoccupied conduction bands of the substrate and adsorbate that comprise the interface under investigation. The ability to directly monitor interfacial electron dynamics represents the critical advantage of time resolved TPPE.

Chapter 2

Background

An introduction to the unoccupied electronic states at surfaces and interfaces will proceed the results and discussion section. In addition, an overview of the relevant experimental techniques for the investigation of electronic structure at surfaces will also follow with particular emphasis placed on the range of systems and phenomena that have been studied with two photon photoemission.

2.1 Unoccupied Electronic states at Surfaces

Image potential states and molecular electron affinity (EA) levels appear prominently in the present investigations. Image potential states result from the abrupt change in polarizability that can occur at an interface. The interface between a metal and vacuum represents an example of particular relevance to the present account. The first electron affinity level represents the energy difference between an electron with no kinetic energy in vacuum and the energy of an excess electron in the lowest unoccupied electronic level of an atom or molecule. Positive electron affinities result when attachment of an excess free electron results in a reduction in the electronic energy. The electron affinity reflects the exchange and correlation of the excess electron with all other electrons. For this reason, the electron affinity level and the lowest unoccupied molecular orbital do not have an equivalent energy.

2.1.1 Image Potential States

An electron near a polarizable surface induces a redistribution of charge at the surface, as shown in Figure 2.1(a). This induced polarization can be modeled as an image charge with a magnitude of $+\beta q$, where the static dielectric constant ϵ determines the value of $\beta = (\epsilon - 1)/(\epsilon + 1)$. For an electron a distance z from the surface, the image charge will appear at $-z$. the interaction between the electron and its image results in a Coulomb potential. For a metal, where $\beta = 1$, the potential equals

$$-\frac{q^2}{16\pi\epsilon_0 z}, \tag{2.1}$$

exactly one fourth that of the Hydrogen atom. Two criteria result in the factor of 4 reduction in the potential: the distance between the electron and its image changes as $2z$ not z, and no electron fields exist in the metal so the integration proceeds from the surface to $+\infty$, not from $-\infty$ to $+\infty$. This Coulomb potential supports an infinite series of hydrogenic states that converge to the vacuum energy, termed image potential states. In the hydrogenic model, which ignores substrate band structure effects, the factor of 4 in the denominator of the potential results in a factor of 16 reduction in the binding energies,

$$E_b = -\frac{13.6}{16n^2}\,\text{eV} \tag{2.2}$$

when compared to the Hydrogen atom. The wavefunction for the image potential states only differ from the hydrogen atom radial wavefunction in two respects; the image potential state wavefunction is the product of the distance z from the surface and the radial wavefunction and the exponential in the radial wavefunction has an additional factor of 4 in the denominator. The probability density for the first two image potential states appears in Figure 2.1(b). The expectation value for these hydrogenic image potential states result in an excited electronic state localized a few Ångstroms outside the surface:

$$\langle z \rangle = 3.17n^2\ \text{Å}. \tag{2.3}$$

The close proximity of the electron density to the metal surface make image potential state energies and lifetimes sensitive to the unoccupied electronic states of an adsorbate. This will prove to be a critical feature of image potential states in the present investigation. A more detailed account of the hydrogenic model of image potential states can be found in the thesis of W.R. Merry [22].

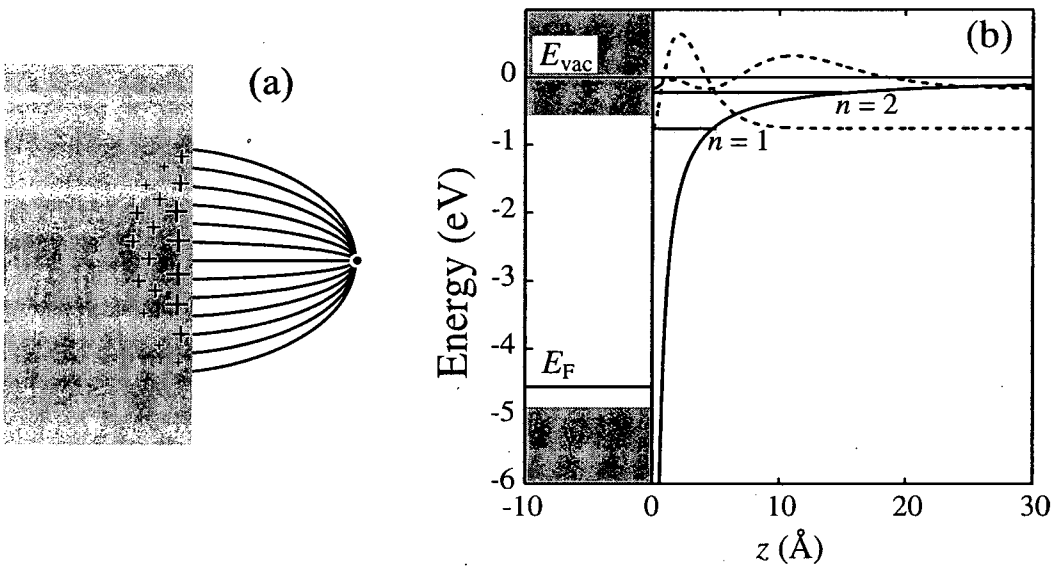

Figure 2.1: (a) Schematic diagram of the electron surface polarization interaction. (b) The image potential results in a hydrogenic series of bound states, termed image potential states. The electron density of $n = 1$ and the $n = 2$ reside only a few Ångstroms outside of the metal surface, making them sensitive to changes in the interfacial electronic structure.

While the hydrogenic model gives a reasonable introduction to the general properties of image potential states, quantitative predictions of image potential state binding energies and lifetimes require more sophisticated treatments. For image potential states on bare metal surfaces, the substrate band structure must be accounted for to achieve quantitative agreement between theory and experiment. Multiple reflection theory represents the simplest of theoretical models utilized to date and has demonstrated that the position of the substrate band gap with respect to the image potential states determines the binding energies and lifetimes of image potential states [23]. The theory uses the two band nearly free electron model to account for the influence of the substrate band structure on image potential states. The theses of W.R. Merry [22] and J.D. McNeill [24] give tractable accounts of this theory, as does the review of Echenique and Pendry [23].

Image Potential State Lifetimes at Metal Surfaces

The lifetime of image potential states at clean metal surfaces reflect two quantities: the round trip time in the image potential and the wavefunction overlap with the substrate. The classical round trip time indicates that image potential state lifetimes will be propor-

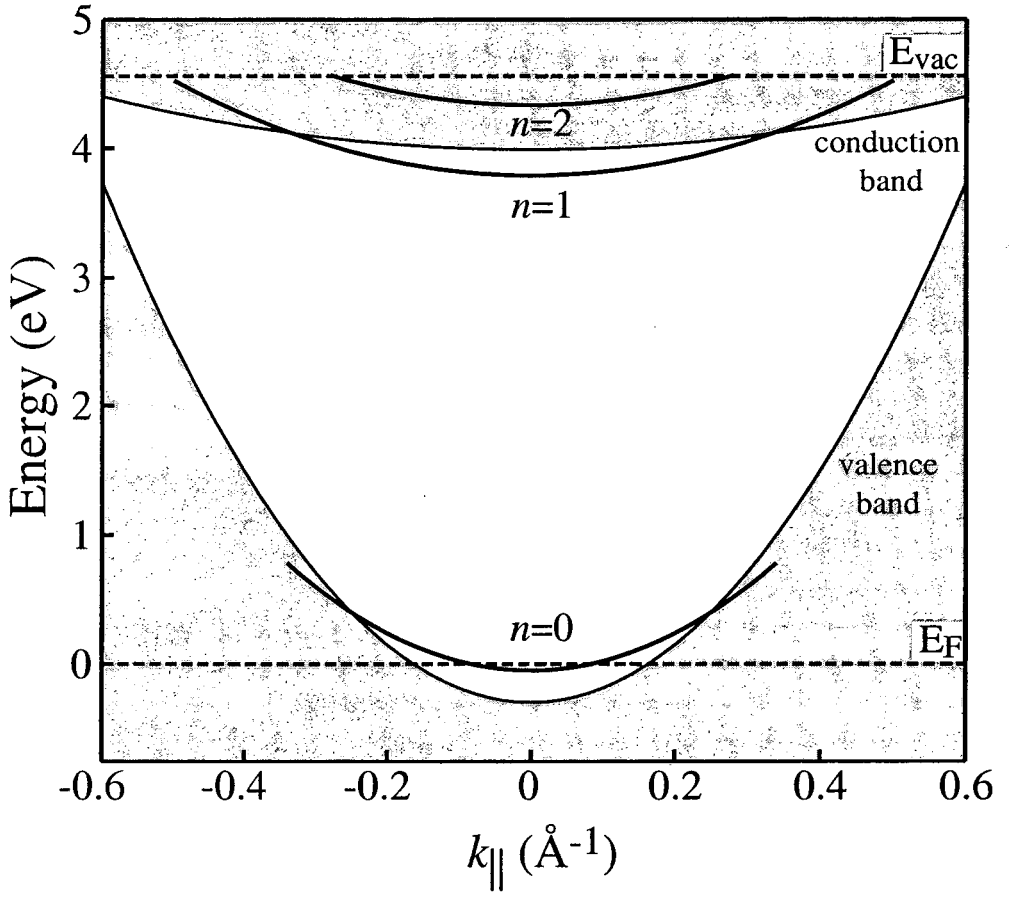

Figure 2.2: The surface projected bulk band structure of Ag(111). The shaded regions correspond to allowed energy levels in the substrate, while the unshaded region corresponds to the surface projected band gap. The $n = 0$ and $n = 1$ surface states reside in the Ag(111) band gap at the Brillouin zone center, while the $n = 2$ and higher image potential states are degenerate with the conduction band.

tional to n^3 [25, 26]. Extensive experimental data has demonstrated the proportionality of image potential states and the electronic wavefunction penetration into the metal substrate [27, 28]. This demonstrates that the energetic position of the image potential state, relative to the band gap, will influence the lifetime. The exponential decay of the image potential state wavefunction in the metal will be fastest near the center of the band gap and will result in the longest lifetimes. For this reason, the lifetime of image potential states at the Ag(100) [26] surface exceed those at the Ag(111) surface. The calculation of the wavefunction in the metal substrate will be discussed in Section 2.2.2.

The Ag(111) surface provides a system where the round trip time and the wave-

function penetration explanations become incompatible. Only the $n = 1$ image potential state resides in the band gap, as shown in Figure 2.2. This results in an $n = 1$ lifetime longer than that of $n = 2$. For $n = 2$ and higher, the lifetimes do increase as n^3 (Figure 2.3). The experimental lifetimes indicate that the higher image potential states undergo multiple oscillations in the image potential, despite the degeneracy of the state with the substrate conduction band. This result cannot be reconciled with the wavefunction penetration description. By matching the wavefunction in the vacuum to an undamped plane wave in the substrate, the normalized wavefunction probability density will all reside in the substrate and the lifetime will be comparable to that of a substrate electron at the same energy. This would predict lifetimes of a few femtoseconds (fs) and little variation with quantum number, in direct conflict with the observed dynamics. These results may indicate that the wavefunction in the substrate and that in the vacuum couple non-adiabatically, where the weak coupling of the image potential state to the substrate electronic states reduces the transition rate.

2.1.2 Excess Electrons in Aromatic Molecular Crystals

The unique electronic properties of aromatic molecules derive from the π bonded molecular orbitals that are delocalized throughout the carbon atom backbone of the molecule. As the size of the aromatic molecule increases, the energy spacing between the highest occupied molecular orbital (HOMO) and the lowest unoccupied molecular orbital (LUMO) decreases. Upon formation of a molecular crystal, the HOMO and LUMO of the single molecule evolve into the valence and conduction bands of the crystal. Consequently, the decreased energy spacing between the HOMO and LUMO results in a band gap reduction and the transition from an insulating to a semiconducting material. The valence and conduction bands also determine the electron transport properties of the material. For these reasons, the function of molecular electronic devices depends critically on the valence and conduction band properties of the molecular semiconductor.

The linear acenes benzene, naphthalene, and anthracene provide a useful series of molecules for the study of electron injection and transport in organic semiconductors for a variety of reasons. The adsorbate electron affinity can be changed systematically, without significantly changing the interfacial chemistry or the electron mobilities. They have the most thoroughly characterized electron transport properties of the molecular semicon-

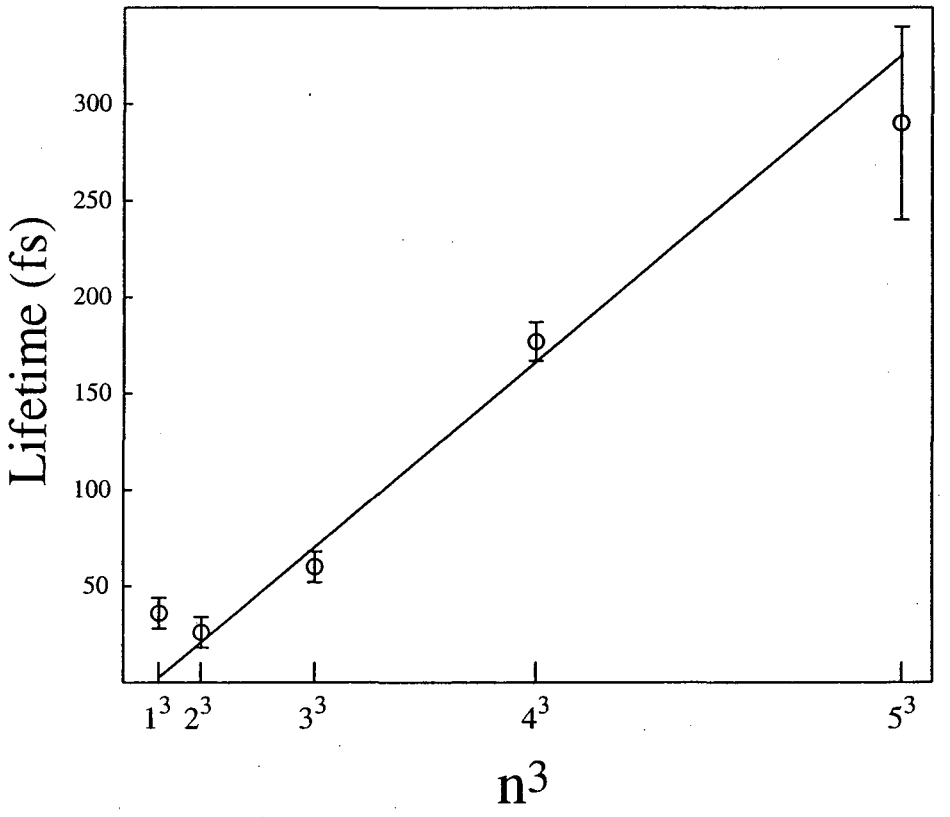

Figure 2.3: Plot of the $n = 1$ to $n = 5$ image potential state lifetimes versus n^3. The $n = 1$ image potential state resides in the Ag(111) band gap, while the higher image potential states are degenerate with the conduction band. For the degenerate image potential states, the lifetime has an n^3 dependence. The $n = 1$ lifetime does not follow this trend due to coincidence with the Ag(111) band gap. These results highlight the significance of the substrate band structure in determining the dynamics of image potential states.

ductors [29]. From an applications perspective, light emitting diodes [30] and field effect transistors [20] have been constructed from linear acene semiconductors. These field effect transistors have exhibited numerous interesting properties, including ambipolar charge injection [20], superconduction [31], lasing [32], and the fractional quantum Hall effect [33].

A few features of the electronic structure and transport properties of aromatic molecular crystals deserve mention. In the gas phase benzene and naphthalene have negative or repulsive electron affinities [34], while anthracene has an positive or attractive electron affinity [35]. The electron affinities of the crystals of these molecules have not been measured directly, but Silinsh and Čápek provide a phenomenological method for calculating the crystal EA levels from the gas phase electron affinity levels and the electronic polarizability of the crystal [29]. The electron affinity will increase in the solid state for two reasons. The molecular anion will be stabilized by the polarization of the neighboring molecules in the crystal and the gas phase EA levels become conduction bands in the solid state. Within the tight binding approximation [36], the overlap integral between nearest neighbors determines the energetic stabilization of the excess electron. Band formation also results in the delocalization of the electron over many molecules.

Linear acene molecular crystals also have well characterized transport properties [29,37]. Two aspects of the electron transport should be mentioned: the mobility is highly anisotropic and has a large temperature dependence. The anisotropy reflects the anisotropy of the crystal structure. The crystal can be thought of as stacked planes of quasi-hexagonally arranged molecules. The electron mobility in the planes exceed the mobility between planes, similar to electrons in graphite. The temperature dependence of the mobility has proven to be much more challenging to understand [29,37–40]. The decreasing mobility with increasing temperature often indicates a band conduction model with coherent transport across many lattice sites. The temperature dependent mobility measurements of Schön et al. indicate that conduction in linear acenes does occur via band conduction at low temperatures, and transition to hopping conduction at higher temperatures [37].

2.2 Theoretical Studies of Image Potential States at Dielectric-Metal Interfaces

The electronic structure at an interface reflects the contributions of multiple, distinct regions. Minimally, the electronic structure will reflect the influence of three regions: the metal substrate, the molecular adlayer, and the vacuum. The surface projected band structure has a significant influence on image potential state properties, as demonstrated by the significantly different energies and lifetimes of image potential states at the Ag(111) and the Ag(100) surfaces (see Section 2.1.1. These substrate band structure effects can be accounted for with the two band nearly free electron model [23, 36]. Two approaches have been utilized for the potential in the layer, the first being a dielectric continuum model presented by Jackson [41] and the second being the two band nearly free electron model utilized for the substrate [22, 36]. The adsorbate layer also modifies the image potential in the vacuum. An analytic solution for the image potential in vacuum, outside of a dielectric covered metal has been derived by Cole [42]. These potentials have been utilized to calculate image potential state energies and wavefunctions. A brief introduction to the two band nearly free electron model and the dielectric continuum model will follow, while the results of the calculations will be addressed in Chapter 4.

2.2.1 Dielectric Continuum Model

The dielectric continuum model accounts for the electronic properties of an adsorbate with a dielectric constant, ϵ, and an electron affinity, EA. The potential in the layer, as derived by Jackson [41], has the following form:

$$V_{in} = -\frac{e^2}{\epsilon z} - EA + \frac{e^2\beta}{4\epsilon(t-z)} - \frac{e^2\beta(t+2z)}{4\epsilon t(t+z)} + \delta V_{in}(z), \tag{2.4}$$

where z is the distance from the metal surface, t is the layer thickness, and $\beta = \frac{\epsilon-1}{\epsilon+1}$. The correction term, $\delta V_{in}(z)$, is given by the infinite series,

$$\delta V_{in}(z) = -\frac{e^2 z^2}{2\epsilon t^3} \sum_{k=2}^{\infty} \frac{(-1)^k}{k(k^2 - z^2/t^2)} \beta^k. \tag{2.5}$$

This infinite series has the following numerical approximation,

$$\delta V_{in}(z) \approx \delta V_{in}(t) \times \frac{z^2}{t^2}\Big[1 - 0.55(1 - z/t) + 0.30(1 - z/t)^2\Big], \tag{2.6}$$

where $\delta V_{in}(t)$ can be explicitly summed to yield,

$$\delta V_{in}(t) = \frac{e^2}{4\epsilon t}\left[\frac{(1+\beta)^2}{\beta}\ln(1+\beta) - \frac{3}{2}\beta - 1\right]. \tag{2.7}$$

The dielectric continuum model potential in the vacuum has the following functional form [42],

$$V_{vac}(z) = -\frac{e^2}{2(\epsilon+1)z} - \frac{e^2\beta}{4(z-t)} + \delta V_{vac}(z), \tag{2.8}$$

with the correction term equal to,

$$\delta V_{vac}(z) = -\frac{e^2\epsilon t}{(\epsilon+1)^2 z}\sum_{k=1}^{\infty}\frac{(-1)^{k-1}k}{kt+z}\beta^k. \tag{2.9}$$

As for the correction term in the layer, this infinite series can be approximated numerically:

$$\delta V_{vac}(z) \approx \frac{2t^2}{z(t+z)} \times \frac{\delta V_{vac}(t)}{1 + 0.222\beta \times \ln(z/t)}, \tag{2.10}$$

where $\delta V_{vac}(t)$ can be summed to give

$$\delta V_{vac}(t) = -\frac{e^2}{t}\left[\frac{\epsilon}{(\epsilon^2-1)} \times \ln\left(\frac{2\epsilon}{\epsilon+1}\right) - \frac{1}{2(\epsilon+1)}\right]. \tag{2.11}$$

In the limit of an infinite dielectric layer, these potentials have a simple form. In the layer, the potential becomes a screened image potential offset by the layer EA,

$$V_{in}(z) = -\frac{e^2}{\epsilon z} - EA. \tag{2.12}$$

The energies of the image potential states at the interface between the metal and dielectric can be calculated using the hard wall assumption of the hydrogenic model:

$$E_b = -\frac{13.6}{16\epsilon^2 n^2}\,\text{eV} - EA. \tag{2.13}$$

In an infinite dielectric, the image potential states converge to the EA level, not the vacuum level. The magnitude of the binding energies with respect to EA for image potential states in an infinite layer also differ from the magnitude of the binding energies with respect to the vacuum energy for image potential states in the vacuum by a factor of $1/\epsilon^2$. In the vacuum, the potential simply reduces to the standard image potential,

$$V_{vac}(z') = -\frac{e^2\beta}{4z'}, \tag{2.14}$$

where $z' = z - t$. For a hard wall dielectric, the energies will be,

$$E_b = -\frac{13.6\beta}{16n^2}\,\text{eV}. \tag{2.15}$$

For an infinite dielectric adsorbed on a metal two infinite series of image potential states can coexist, one at the metal-dielectric interface and one at the dielectric-vacuum interface. For a positive electron affinity layer of finite thickness an issue arises; will image potential states be observed in the screened image potential in the layer, the image in the vacuum, or both.

2.2.2 Two Band Nearly Free Electron Model

The two band nearly free electron model provides an alternative description of the layer electronic structure, as well as the model of choice for the metal substrate. In the two band NFE model, the influence of the ion core potential on the free electron is treated as a perturbation [36]. The perturbation V_g equals one half of the band gap at the Brillouin zone boundary. Solving the following secular equation gives the electronic energies:

$$\begin{vmatrix} (\hbar^2/2m^*)k^2 - \varepsilon & V_g \\ V_g & (\hbar^2/2m^*)(k-g)^2 - \varepsilon \end{vmatrix} = 0 \tag{2.16}$$

with k being the wavevector, $g = \frac{\pi}{2a}$ being the reciprocal lattice vector, and a being the lattice constant. The resultant wavefunction for a state energetically coincident with the band gap consists of an exponentially damped evanescent wave,

$$\psi_c = e^{qz}\cos(pz + \delta), \tag{2.17}$$

with the real, p, and imaginary, q, parts of the wavevector k being determined by the energy of the state. The value of p ranges from zero to π/a at the Brillouin zone boundary, while the energy dependence of q has the following functional form:

$$q = \sqrt{\hbar^2/2m_e}\left(\sqrt{[\varepsilon E_g + V_g^2]} - \varepsilon - E_g\right)^{1/2} \tag{2.18}$$

For states degenerate with an adsorbate band, $q = 0$ and the wavefunction consists of an undamped plane wave. In the band gap, q will be positive with a maximum value of

$$q_{max} = \frac{2m^*V_g}{g\hbar^2} \tag{2.19}$$

near the middle of the band gap. The symmetry and orientation of the orbitals out of which the bands form determines the phase, δ, of the wavefunction.

2.3 Principles of Two Photon Photoemission

The electronic states of solids and surfaces have been widely investigated with photoelectron spectroscopy [43]. With photoemission, the occupied electronic structure can be studied from the Fermi energy to the core electronic shells. With inverse photoemission [44], the unoccupied electronic levels can be studied from the Fermi energy to tens of eV above the vacuum energy. Two photon photoemission has the distinction of being able to investigate both the occupied and the unoccupied electronic structure. For an electron to be photoemitted, the energy of the photon, or 2 photons for TPPE, must exceed the workfunction of the material being studied. For the primary source of the signal to be electrons photoemitted with two photons, the energy of a single photon cannot exceed the workfunction. This limits the range of electronic states that can be investigated by TPPE to 5 eV below the Fermi level to 5 eV above the vacuum energy for a sample with a workfunction of 5 eV. Fortunately, this covers much of the energy range relevant to surface chemistry and charge transport.

A schematic depiction of TPPE appears in Figure 2.4. The first of the two photons excites an electron from an occupied state to an excited state, while the second photon photoemits the excited electron into the vacuum. Peaks in the TPPE kinetic energy spectrum can result from initial, intermediate, and final states. These different electronic states can be distinguished by measuring the photon energy dependence of the photoelectron kinetic energy. For single color TPPE, the plot of the photoelectron kinetic energy of an initial state peak versus the photon energy will have a slope of two. For an intermediate state, the slope will be one. For a final state, the photoelectron kinetic energy will not change with photon energy. Peaks due to initial, intermediate and final electronic states have all been observed with TPPE.

2.3.1 Angle Resolved Two Photon Photoemission

With angle resolve TPPE, the three dimensional electronic structure can be monitored. For electrons in vacuum or periodic solids, the wavefunction will be periodic, with the periodicity being determined by the wavevector, k. This wavevector represents the principle quantum number for electrons in periodic solids. The electronic dispersion, or the wavevector dependence of the electronic energy, characterizes the electronic structure of periodic solids. In angle resolved photoemission, the relation between the energy and the

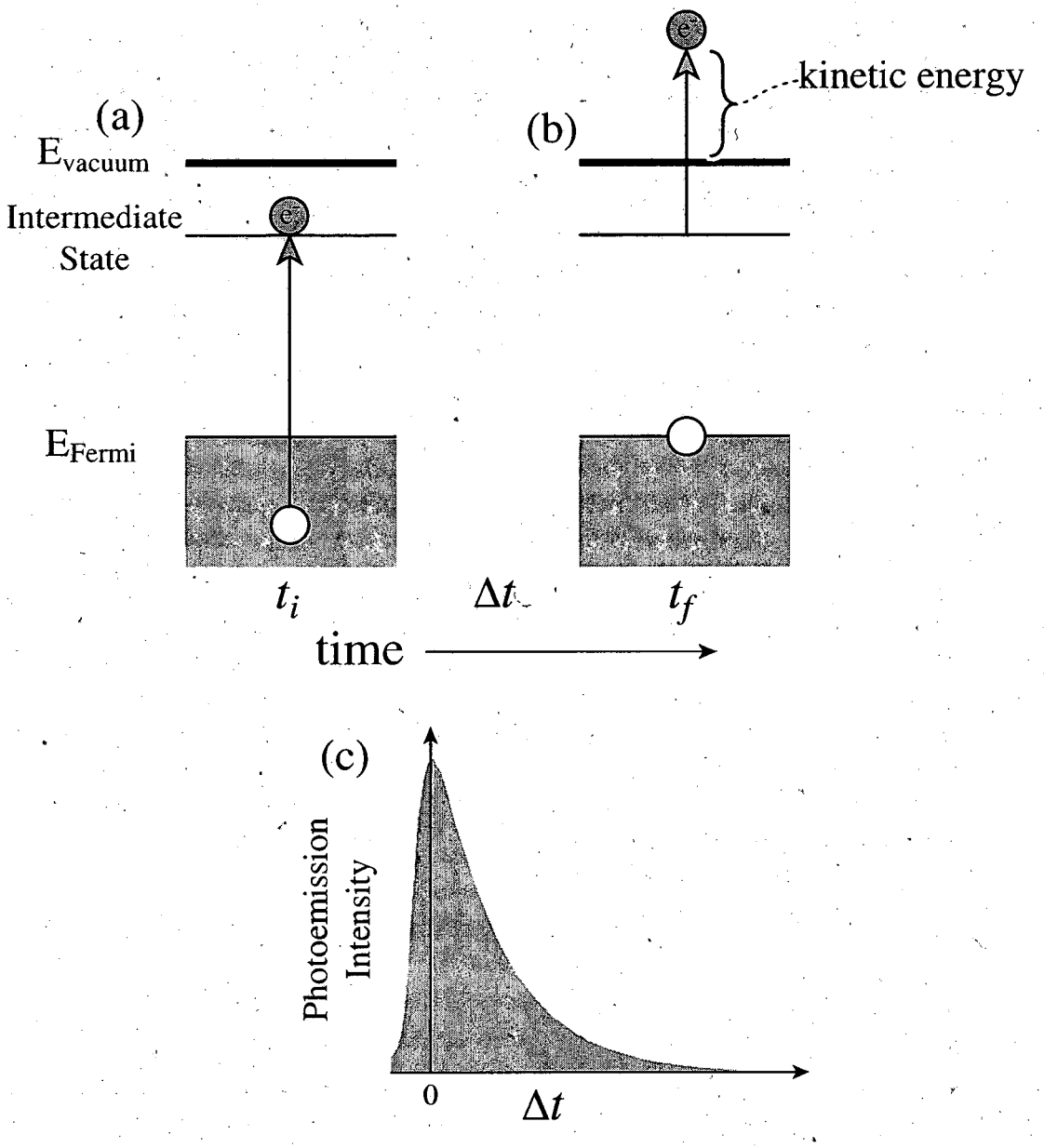

Figure 2.4: Schematic presentation of time resolved two photon photoemission. (a) At time t_i a pump pulse excites an electron from the occupied valence band of the substrate into an unoccupied surface state. (b) After a delay time of $\Delta t = t_i - t_f$, a second probe pulse photoemits the surface state into vacuum, where the kinetic energy of the electron is measured via time of flight analysis. (c) Monitoring the intensity of the detected signal as a function of Δt provides direct access to excited state dynamics.

parallel component of the wavevector, $k_{||}$, can be measured. This represents the parallel dispersion of the electronic band structure.

The photoemission process conserves $k_{||}$, but not the perpendicular wavevector, $k_{\perp}$. In the photoemission process, the electron must cross a surface. In the direction normal to the surface, $k_{\perp}$ provides a good quantum number for the initial and final states, but does not define the electronic wavefunction at the aperiodic surface. For this reason, photoemission does not conserve $k_{\perp}$. In the direction parallel to the surface, the potential retains its periodicity with the amplitude of the potential oscillations decreasing to zero in the vacuum. For this reason, the photoemission process conserves $k_{||}$. The lack of $k_{\perp}$ conservation limits the ability of photoemission to measure the normal dispersion of the electronic band structure. This does not effect the study of surface electronic states, which have no dispersion normal to the surface.

By measuring the photoelectron kinetic energy, E_{kin}, as a function of the angle, θ, between the surface normal and the detector, the two dimensional band structure parallel to the surface can be measured. A schematic representation of angle resolved TPPE appears in Figure 2.5. The angle dependence of the kinetic energy provides a direct measure of $k_{||}$,

$$k_{||} = \sqrt{\frac{2m_e E_{kin}}{\hbar^2}}\,\sin\theta, \tag{2.20}$$

where m_e represent the free electron mass. Nearly free electronic states possess parabolic dispersions given by

$$E(k_{||}) = E_{||} + E_0, \tag{2.21}$$

where $E_{||} = \hbar^2 k_{||}^2/2m^*$, E_0 is the kinetic energy at zero degrees, and the effective mass, m^*, is a parameterized measurement of the curvature of the dispersion. Image potential states generally have parabolic dispersions, though non-dispersive image potential states have been observed for both benzene and anthracene adsorbates. The dispersion of image potential states will be discussed in detail in Chapter 5.

2.3.2 Time Resolved Two Photon Photoemission

The ability to directly monitor the dynamics of excited electronic states at surfaces provides the primary advantage of TPPE over inverse photoemission. For laser pulses with time durations comparable to or shorter than the excited state dynamics, the excited state

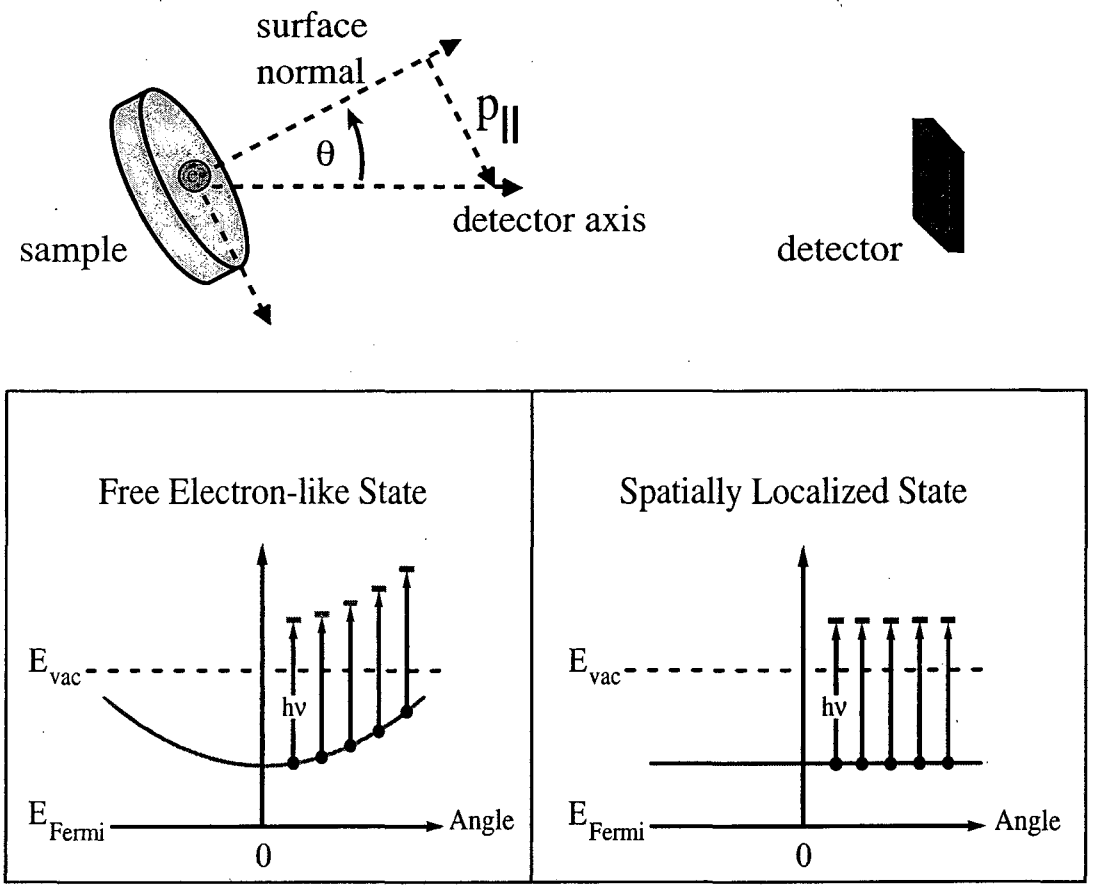

Figure 2.5: Schematic diagram of angle resolved two photon photoemission. For an electron to be detected when $\theta > 0$, the electron must have a component of momentum parallel to the surface, $p_{||} = \hbar k_{||}$. As θ increases, so does $p_{||}$. By measuring the parallel dispersion, the $p_{||}$ dependence of the photoelectron kinetic energy, the interfacial band structure can be determined. The quantum number $k_{||}$ characterizes nearly free electronic bands. For nearly free electron bands, $p_{||}$ determines the energy and the dispersion will be parabolic. These states with well defined momenta are spatially delocalized, in accordance with the Heisenberg uncertainty principle. For spatially localized electronic states, $k_{||}$ will not be a good quantum number, and the energy will no longer depend on $p_{||}$. Such states will have flat dispersions.

lifetime can be directly monitored by measuring the peak intensity as a function of delay time between the arrival of the pump pulse and the probe pulse (Figure 2.4). The excited state dynamics can also be accessed in the frequency domain, by monitoring the peak widths and shapes. Extracting population dynamics from the peak widths in the TPPE photoelectron kinetic energy can be problematic for a variety of reasons. The linewidth in an absorption experiment gives the dephasing time, not the lifetime. In the case of TPPE, which involves two electronic transitions, the linewidth reflects the dephasing times for both transitions, as well as the system inhomogeneity. These complications do not limit themselves to the frequency domain. Coherence effects in time resolved TPPE have been addressed by Petek, Wolf, Fauster, and Höfer [26, 45–47]. The necessity of both an exponential rise and decay time characterizes the dynamics of image potential states at a variety of metal surfaces. While the necessity of a rise time has been assigned to coherence effects, the delay in the signal maximum may also result from image potential state intraband relaxation. The thesis of C.M. Wong gives a thorough account of these issues [48]. A detailed study of the momentum resolved dynamics at the Ag(100) surface should be able to conclusively determine the significance of intraband relaxation in image potential state dynamics. Section 5.3 discusses the advantages of using a Ag(100) surface, as opposed to a Ag(111) surface, for studying intraband relaxation.

2.3.3 Polarization Dependent Two Photon Photoemission

The symmetry of the intermediate electronic states can be determined by measuring the probe pulse polarization dependence of the signal [43, 49]. The detector lies along the surface normal in the TPPE spectrometer used in the present thesis. For an electron to be detected with this experimental configuration, the final state must not have a nodal plane parallel to the detector normal and the transition dipole matrix element must contain the totally symmetric irreducible representation of the appropriate point group. At 0°, the detector normal lies parallel to the surface normal. The features of a polarization study can be seen by considering electronic states that have the symmetry of the C_{3v} point group with the surface normal being the high symmetry axis. The final state must be symmetric with respect to σ_v, limiting it to the A_1 irreducible representation. P polarized light also has A_1 symmetry, while S polarized light has E symmetry. The symmetry of the final state and the laser polarization limits the symmetry of the initial state to A_1 for P polarization

and E for S polarization.

The polarizability of the nearly free electron gas in the metal complicates polarization measurements at metal surfaces [50]. The electric field of the incoming light induces a polarization in the metal. This polarization results in an electric field that cancels the electric field of the incoming light in the metal. For P polarized light this results in an amplification of the electric field on the vacuum side of the surface, while for S polarized light this results in the cancellation of the electric field at the surface. This effect has been termed the surface selection rule. The frequency dependent dielectric constant of the metal provides the lone parameter in the theoretical explanation of this effect. The surface selection rule depends on the frequency of the light. For frequencies above the low energy plasmon frequency of Ag, roughly 10^{15} Hertz, the surface selection rule no longer applies and S polarized light will have sufficient intensity at the surface. For this reason polarization studies must be conducted with light well into the UV. Polarization studies at interfaces with small workfunctions cannot be conducted with TPPE, because the photon energies cannot exceed the workfunction as discussed above.

2.3.4 Applications of Two Photon Photoemission

Time and angle resolved two photon photoemission has been applied to a wide range of experimental systems. The initial investigations focused on carrier dynamics at semiconductor surfaces [51]. Mode locked Ti:sapphire based solid state lasers have provided wider range access to fs laser pulses. This has transformed the experimental investigation of electron dynamics in metals and at metal surfaces, where excited state lifetimes range from picoseconds to a few fs.

A large number of the researchers in the field of time resolved TPPE have studies hot electron dynamics in metals [52–55]. The short lifetimes of excited electrons in metals places a premium on short pulse durations. The majority of investigations have utilized laser pulses with time durations of 50 to 100 fs. These pulse durations make accessing lifetimes shorter than 20 fs difficult, at best. The work of H. Petek and coworkers deserves particular notice. His investigations utilized phase resolved pulses with time durations of 15-20 fs. The phase resolution allows direct access to electronic dephasing dynamics [53, 56, 57], while the shorter pulses make for more accurate measurements of hot electron population dynamics in metals [52]. The phase resolved studies do access an increased

range of dynamic information, but they do not identify the cause of the dephasing. To distinguish between homogeneous and inhomogeneous dephasing mechanisms, as well as spectral diffusion, photon echo measurements must be made. Deviations from Fermi liquid theory dynamics have been observed. The scattering and screening of excited electrons with d band electrons has been invoked to explain these deviations. The spin dependent dynamics of hot electrons in ferromagnetic materials have also been measured, with the majority spin states having longer lifetimes.

In addition to electron dynamics in metals, TPPE has been widely used to study the dynamics of electrons photoattached to atomic and molecular adsorbates. Alkali atom adsorbates on metal surfaces have been widely studied. Small coverages of alkali metals result in large reductions in the workfunction, which can be very beneficial for TPPE studies utilizing the second harmonic of a Ti:sapphire laser. The studies of the Cs/Cu(111) interface by H. Petek and coworkers have been among the most interesting [58, 59]. These investigations represent the first state and time resolved investigation of electron photodesorption at a metal surface, a process widely invoked to explain photochemistry at metal surfaces [1, 2].

The investigation of photoelectron attachment to molecules has also been conducted at metal surfaces. The primary system of study has been carbon monoxide on the low Miller index surfaces of Cu. The CO/Cu(111) interface has been widely studied by M. Wolf and associates [60, 61]. While excess electrons from a scanning tunneling microscope have resulted in CO desorption, no evidence exists for CO photodesorption during two photon photoemission. The study of Reuß et al. on the CO/Cu(100) interface determined the coverage dependent linewidth of the $n = 1$ image potential state [62]. They did not report the appearance of the CO electron affinity level in the TPPE kinetic energy spectrum, though they attributed the large linewidth to scattering of the image potential state with the CO electron affinity level. This should be contrasted with the work of Wolf et al., where the first electron affinity level and the $n = 1$ state appear in roughly the same area in the spectrum [61]. The different symmetry of the $n = 1$ image potential state and the π^* electron affinity level of CO made the polarization dependence of the photoelectron kinetic energy spectrum essential to the identification of both $n = 1$ and the π^* state [61]. The low intensity and asymmetry of the peaks, as well as the large background signal, make linewidth analysis of the TPPE spectrum difficult for CO on copper. While the Lorentzian width of a peak can be related to a dephasing time, the total linewidth may primarily reflect

the heterogeneous distribution of energies at the interface, not the dynamics. Reuß et al. associate the total linewidth with the inverse lifetime, not just the Lorentzian width [63]. For an incomplete coverage, the surface will have a significant workfunction heterogeneity, which will broaden peaks in the photoelectron kinetic energy spectrum. This provides an alternative explanation for coverage dependent linewidths that has not been addressed by Reuß et al.

A variety of physically adsorbed materials have also been investigated. Detailed studies of dielectric-metal interfaces demonstrate the importance of the adsorbate electron affinity in determining the unoccupied electronic structure and the excited state dynamics at interfaces [64]. Repulsive electron affinity materials exclude excess electrons from the adsorbate layer and effectively decouple image potential states from the metal substrate. This results in reduced binding energies and longer lifetimes [65]. These longer lifetimes allow the image potential state electron to induce structural changes in the adsorbate layer, resulting in dynamic electron localization [66]. For positive electron affinity materials, the electron can reside in the layer. This results in quantum well formation at the Xe/Ag(111) interface [27]. A review of these results has been written by C.B. Harris et al. [64]. A thorough account of alkane adsorbates can be found in the thesis of N.-H. Ge [67], while the theses of J.D. McNeill [24] and C.M. Wong [48] address Xe adsorption of Ag(111). A variety of physisorbed aromatic molecules have also been investigated, but these studies will be addressed in the Chapter 4.

Chapter 3

Experimental

The time and angle resolved two photon photoemission results reported in this thesis relied on a wide range of experimental techniques and technology. The experimental apparatus can be partitioned into three primary regions: a solid state ultrafast laser system for the generation of visible and ultraviolet laser pulses of roughly 100 fs duration, an ultrahigh vacuum chamber for sample preparation and preservation, and the data acquisition electronics. Many aspects of this apparatus have been addressed in detail in prior theses. The thesis of W.R. Merry gives a detailed description of the ultrahigh vacuum system and the time-of-flight energy analyzer [22]. The thesis of J.D. McNeill [24]thoroughly described the data acquisition hardware and software, while the thesis of C.M Wong [48] addresses the low energy electron diffraction and Auger electron spectrometer. The present thesis will focus on the ultrafast laser system, and sample preparation.

3.1 Experimental Apparatus

The diagram of the time and angle resolve two photon photoemission spectrometer appears in Figure 3.1. The experiments described in this thesis utilized a Coherent laser system. An Innova 425 Ar ion laser operating at 48 Amps produces a multiline output of 22 Watts. Roughly a third of this continuous wave output pumps a Coherent Mira 900-F Ti:sapphire oscillator, with the remaining power used to pump a Coherent RegA 9000 Ti:sapphire regenerative amplifier.

The primary cause of laser system instability results from instability in the Ar ion laser mode and pointing. Increases in the current in excess of 0.3 Amps, while under

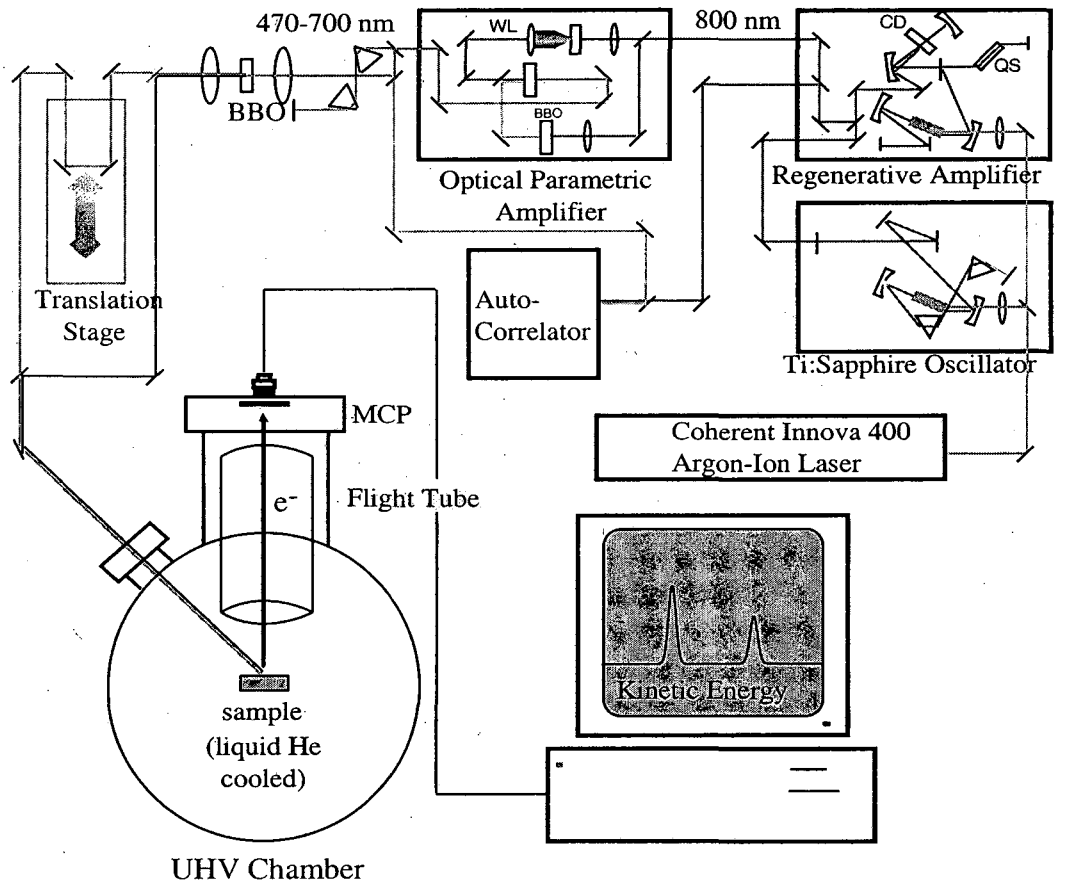

Figure 3.1: Schematic depiction of the time and angle resolved two photon photoemission spectrometer.

constant power operation, represents an important diagnostic for identifying problems with the Ar ion laser performance. This does not, however, provide a reliable diagnostic for mode degradation. Problems with the Ar ion laser can often be alleviated by cleaning the Brewster window in the laser cavity, as well as the output coupler.

The Mira 900-F oscillator uses Ti:sapphire as the gain medium. A birefringent filter in the oscillator determines the wavelength of the laser. The oscillator operates at 800 nm with the current set-up. Large changes in the wavelength require a different set of optics for the laser cavity. The stability of the oscillator alignment make the Mira 900-F continuous wave power a reliable indicator of Ar ion performance. While day to day fluctuations in peak power of five percent do occur, a decrease in power of over five percent generally indicates a problem with the pump laser. The oscillator operates at a repetition rate of 76 MHz, has a mode locked power of 1.2 Watts, and generates pulses with 150 fs time durations.

The RegA 9000 regenerative amplifier uses about 50 mW of the oscillator output as a seed. The amplifier has an aucostoptic cavity dumper and Q-switch. The cavity dumper injects a single seed pulse into the amplifier cavity. The injected seed pulse undergoes multiply round trips in the amplifier before the cavity dumper emits an amplified pulse. The regenerative amplifier has an optimal performance at 200 kHz and a wavelength of 800 nm. Generally, the output of the regenerative amplifier has the least shot to shot noise when the amplified power in the cavity reaches and remains at a maximum for two round trips before dumping the pulse from the cavity. This can be best achieved with more round trips and a lower repetition rate, but increasing the round trips and reducing the repetition rate have other consequences that negatively effect laser performance. Increasing the round trips broadens the pulses in time. When the round trips exceed roughly 25, the pulses cannot be fully recompressed by the four pass holographic grating compressor in the RegA 9000. This results in less efficient second harmonic and white light generation in the optical parametric amplifier. The TPPE signal reaches a maximum at roughly 250 kHz, so reducing the repetition rate negatively effects the signal. A range of regenerative amplifier setting can work and choosing parameters within this functional operation range should be determined by the particular study being conducted. Stability should be emphasized when collected electron dynamics data, while TPPE signal can be emphasized when the relative amplitudes of peaks in multiple kinetic energy spectra do not need to be compared.

The OPA 9400 uses the output of the RegA 9000 to generate visible light tunable

from 470 nm to 730 nm. The optical parametric amplification results from the mixing of the second harmonic of the Ti:sapphire with a white light continuum in a Barium Borate (BBO) nonlinear optical crystal. Focusing of half the amplifier output in a sapphire crystal produces the white light, while focusing the other half of the amplifier output in a BBO crystal produces the second harmonic. By adjusting the angle of the BBO mixing crystal with respect to the white light and second harmonic, the frequency of the visible light can be selected. The first pass through the BBO crystal chooses the frequency, while a second pass amplifies the output. Instability in the OPA 9400 output usually results from instability in the white light continuum. When observing the continuum in the far field, the intensity should not flicker. The second harmonic power provides another important diagnostic. A minimum second harmonic power of 140 mW must be achieved to generate enough power to conduct TPPE experiments. When the laser system functions effectively, 160 mW should not be difficult to achieve and second harmonic powers as high as 180 mW can occur. The focusing of the second harmonic into the mixing crystal must be adjusted as the second harmonic power varies. For low second harmonic power, tight focusing results in higher OPA power and adequate mode quality. Tight focusing of the second harmonic when the power is high results in poor mode quality. The OPA 9400 power should be about 25 mW, though powers as high as 40 mW have been achieved and successful experiments have been conducted with powers as low as 18 mW. The output power does vary with wavelength, increasing as the wavelength increases.

The pulses generated by the OPA have to be compressed with a prism pair to minimize the pulse width. Doing so results in nearly transform limited pulses of about 70 fs FWHM (full width at half maximum). The pulse width does have a wavelength dependence, with the widths increasing with decreasing wavelengths. Pulse widths closer to 130 fs FWHM result at 530 nm. Pulse compression reduces the power by a factor of two. After compression, the pulses are focused into a BBO crystal to generate the second harmonic of the OPA output. About a third of the incoming pulse is doubled. At the sample, the laser has a per pulse power of roughly 20 nJ for the visible pulses and 10 nJ for the UV pulses.

A dichroic mirror separates the UV light from the visible light. The path of the visible light contains a computer operated translation stage. The stage can be moved in one micron steps. This results in a 6.66 fs change in the arrival time of the visible light pulses at the sample. A second dichroic mirror spatially overlaps the visible and UV light

pulses, while a lens focuses the pulses at the sample surface. The laser pulses impinge on the surface at 60° off normal.

The energy and temporal resolution of the spectrometer can be characterized experimentally. Gaussian features as narrow as 20 meV FWHM have been observed for monolayers Xe adsorbed on the Ag(111) surface. These studies indicate that the course graining of the time of flight by the detector determines the energy resolution of the peaks in the energy range we usually observe signal. Generally the Gaussian widths of the peaks in the spectrum significantly exceed 20 meV, indicative of inhomogeneous broadening. Peaks generally have a Lorentzian width as well on the order of 10 to 100 meV. The peaks often can be fit to a Voight function, which consists of a Gaussian convolved with a Lorentzian. Peak asymmetry and a kinetic energy dependent background signal generally compromises the quality of the peak fitting and makes lineshape analysis difficult.

Measuring the temporal instrument function that determines the time resolution of the experiment plays a critical role in data analysis. The cross correlation of the pump and probe pulses determines the time resolved TPPE instrument function. Identifying a transient signal with no intermediate state population dynamics proves to be the key step to measuring the instrument function experimentally. Two complementary approaches have been used for the Ag(111) surface. The dynamics of the occupied surface state, when photoemitted via a virtual state with zero lifetime, can be used to determine the instrument function. Alternatively the dynamics of the non-resonant background can be used to determine the instrument function. Both approaches have been shown to give the same instrument response function.

3.2 Sample Preparation

The first step to sample preparation involves the cleaning and characterization of the Ag(111) substrate. Sputtering with Ar at 500 K and annealing at 725 K preceded every experiment. With low energy electron diffraction (LEED), the order and orientation of the surface can be verified. With Auger electron spectroscopy the presence of contaminants on the surface can be identified. Aromatic molecules only adsorb on Ag(111) at cryogenic temperatures. A liquid He cryostat achieves sample temperatures as low as 50 K. A leak value introduces the gaseous contents of a high vacuum sample line into the UHV chamber. The sample line has a base pressure of 5×10^{-7} Torr, while the pressure of the sample gas

being dosed varied from a few Torr for benzene to a couple 100 mTorr for anthracene. Solid anthracene had to be heated to achieve these pressures.

The adsorption of benzene on Ag(111) has been investigated with a multitude of techniques and many aspects of benzene layer growth have been determined. These previous studies, in conjunction with in situ LEED and TPPE analysis, are used to determine the benzene coverage. Benzene physisorbs molecularly on Ag(111) with the plane of the molecule parallel to the interface [68,69]. Ordered LEED patterns for benzene appear below 160 K in the presence of a 5×10^{-8} torr benzene back pressure, consistent with the work of Somorjai and Firment [70]. The adsorption temperature for the monolayer determined from LEED does not agree with that determined from temperature programmed desorption studies (TPD). A scanning tunneling microscopy study of benzene adsorption on the Cu(111) surface may provide an explanation for this discrepancy. As seen for Ag(111), a peak in the TPD intensity occurs at about 220 K with a peak maximum that shifts to lower temperature as the coverage increases. In the TPD studies at both of these surfaces, this peak has been attributed to monolayer desorption and the coverage dependent shift in the peak maximum to repulsive interactions between adsorbed benzene molecules. The STM study provides an alternative explanation for these observations. Benzene prefers to chemisorb to step edges on the Ag and Cu surfaces. The benzene desorbing at 220 K corresponds to the desorption of benzene chemisorbed at step edges, while the shift to a lower adsorption temperature as coverage increases occurs when the surface defects have been saturated.

The growth of a monolayer and a bilayer is determined by monitoring the dose dependent LEED pattern at 120 K. For a dosage of 1 to 4 Langmuir at 120 K no overlayer LEED pattern is observable, while a dosage of 5 to 6 Langmuir results in a LEED pattern consistent with the (3×3) benzene monolayer LEED pattern reported by Dudde et al. for a dosage of 5 Langmuir [69]. An additional 12 Langmuir results in a new hexagonal LEED pattern commensurate with the substrate and possessing a larger unit cell than the monolayer pattern. The pattern cannot be due to a more densely packed monolayer because the unit cell increases, rather than decreases, in size. This pattern results from the formation of a stable bilayer at 120 K. Neither the LEED pattern nor the TPPE spectra change when the benzene dosage exceeds 18 Langmuir, leading to the conclusion that only a bilayer will persist at 120 K. This is the first observation of a stable bilayer of benzene absorbed on Ag(111), though a stable bilayer has been observed on Cu(111) [71]. Benzene coverage in

excess of a bilayer was grown at 80 K. The change in the workfunction and the $n = 1$ effective mass signal the transition from a bilayer to a trilayer of benzene. To increase the benzene coverage from a bilayer to a trilayer requires an additional 15 Langmuir. Coverage in excess of a trilayer is estimated from the dose dependence of the trilayer.

The adsorption of naphthalene and anthracene on Ag(111) has also been investigated with multiple techniques, and many aspects of aromatic layer growth on the Ag(111) surface have been determined. Naphthalene and anthracene physisorb with the plane of the molecule parallel to the Ag(111) surface [72,73]. LEED studies confirm that adsorption results in ordered monolayers [70, 72, 73]. The multilayer coverages also result in ordered crystal structures as determined by LEED. In situ monitoring of layer growth with TPPE confirms that multilayer naphthalene and anthracene grow in a layer by layer fashion. With each successive layer, the increase in image potential state signal from the new layer coincided with the depletion of the image potential state signal from the old coverage, the signature of epitaxial growth as seen previously with TPPE [74, 75]. The simultaneous observation of image potential states corresponding to the clean surface and a monolayer coverage do not occur. This indicates that the monolayers initially adsorb diffusively on the surface, rather than in islands. LEED analysis confirms the accuracy of the TPPE determined coverage. Annealing of the mono-, bi-, and trilayer of naphthalene occurred at 180 K, 130 K, and 110 K, while the corresponding temperatures for the anthracene mono- and bilayer are 175 K and 140 K.

Workfunction determination must be achieved to determine the binding energy of the transient electronic states in the TPPE kinetic energy spectra. The workfunction of a material results from two contributions: the electrochemical potential of the material and the surface dipole layer that an electron must cross during photoemission. Molecular adsorbates alter the surface dipole layer, which results in adsorbate induced changes in the workfunction. Adsorbate induced changes in the workfunction result in a contact potential difference between the sample and detector that causes changes in the photoelectron kinetic energy in the flight tube. A bias voltage can be applied to counteract the contact potential difference once the workfunction change has been measured. This was achieved with two approaches. The first approach involves fitting the image state energy separations to a quantum defect parameter a, $E = -0.85/(n + a)^2$ eV, which in turn gives the image state binding energies. The extent by which the image state binding energies differ from the predicted values gives the change in workfunction. This method could not be applied to

the naphthalene monolayer because the binding energies do not fit a hydrogenic series. The second method involves determining the TPPE kinetic energy width for an accelerating voltage bias between the sample and the detector so that both a high and a low energy cut-off appear in the kinetic energy spectra. Only UV light at a frequency that disallows single photon photoemission is used and the TPPE kinetic energy width is subtracted from the energy of two UV photons to determine the workfunction. A cumulative changes in the workfunction a mono-, a bi-, and a trilayer of benzene are -0.65±0.02 eV, -0.72±0.02 eV, and -0.68±0.02 eV. The cumulative changes in the workfunction for a mono-, a bi-, and a trilayer of naphthalene are -0.62 ± 0.07 eV, -0.72 ± 0.02 eV, and -0.75 ± 0.02 eV. The corresponding changes for anthracene are -0.68 ± 0.02 eV for the monolayer and -0.74 ± 0.02 eV for the bilayer. All cited binding energies reflect the results of quantum defect determined changes in workfunction, except for the naphthalene monolayer. The photoemission width measurements give similar values. The change in workfunction measured for benzene lies between the values of Zhou et al. [76], -0.7 eV for a monolayer of benzene and -0.9 eV for multilayer benzene, and Dudde et al. [69], -0.3 eV for a monolayer of benzene. Frank et al. measured similar workfunction changes of -0.5 ± 0.1 eV for both naphthalene and anthracene [72].

Chapter 4

Heterogeneous Electron Transfer at Aromatic/Metal Interfaces

A systematic investigation of the unoccupied electronic structure at aromatic/metal interfaces has been conducted. Many criteria support the investigation of aromatic adsorbates on an inert metal surface. (1) The electron affinity of aromatic molecules can be varied systematically by changing the size of the molecule. This has been achieved with a series of aromatic molecules, namely benzene, naphthalene, and anthracene, adsorbed on an inert Ag(111) metal surface. (2) Field effect transistors constructed from aromatic molecular crystals deposited on gold electrodes have exhibited a wide range of interesting and potentially useful electronic properties, providing context and motivation for the characterization of two dimensional charge transport at inert metal/aromatic interfaces. (3) The weak chemical interaction between the substrate and the aromatic adsorbates greatly simplifies the theoretical explanation of the experimental results.

4.1 Prior Studies of Electronic Excited States of Aromatic-Metal Surfaces

Previous investigations of the excited electronic structure of benzene, naphthalene, and anthracene physisorbed on noble metal surfaces provide key information that complements and enhances the interpretation of our time and angle resolved TPPE results. Frank et al. conducted inverse photoemission spectroscopy (IPS) studies of the excited

electronic states of 2-3 layers of these molecules adsorbed on Ag(111) [72]. They found the energy spacing between the electron affinity levels of these aromatic molecules adsorbed on Ag(111) to be similar to the energy spacing between the same electron affinity levels in the gas phase, supporting the conclusion that the silver substrate only weakly perturbs the electronic structure of aromatic adsorbates. The shift to larger electron affinities for adsorbed, as opposed to gas phase, molecules reflects stabilization of the anion by the polarizable adlayer and the silver substrate image potential. A more detailed comparison of the TPPE results contained in this thesis with the IPS results of Frank et al. will follow the description of the TPPE results.

Recent studies have utilized TPPE to investigate benzene and naphthalene adsorbed on Cu(111). Munakata et al. studied 0.3 Langmuir of benzene dosed at 100 K with static TPPE [77]. The TPPE study identified the ionization potential of the first triplet excited state of benzene adsorbed on Cu(111) and possibly a vibrational progression, but did not report any benzene anion states or image potential states. A second TPPE study conducted by Velic et al. has also been conducted on the benzene/Cu(111) interface [74]. This study did not observe any intramolecular excitations of benzene. The Velic et al. study focused on a coverage of 1.5 layers of benzene on Cu(111) with time and angle resolved TPPE. This coverage simultaneously supports $n = 1$ image states for both monolayer and bilayer benzene, as well as the benzene first electron affinity level 0.6 eV above the vacuum level. This marks the first observation of a final state resonance with TPPE. Why the first electron affinity level of benzene lies 1.2 eV higher in energy for physisorption on Cu(111) than it does for physisorption on Ag(111) [72] remains unclear. The $n = 1$ lifetime for the monolayer and bilayer $n = 1$ state were measured to be 40 fs and 20 fs, respectively. The image state binding energies and lifetimes were modeled with a dielectric continuum model. The model calculation suggests that the $n = 1$ bilayer lifetime should be three orders of magnitude longer than the $n = 1$ monolayer lifetime, rather than halved. The TPPE study conducted by Wang et al. on the naphthalene/Cu(111) interface assigned the peaks in the TPPE kinetic energy spectrum to be image potential states, not electron affinity levels.

Other studies confirm that the aromatic adsorbate interacts weakly with the Ag(111) surface, leaving the majority of benzene electronic properties only weakly perturbed. Molecular orbital calculations by Anderson et al. indicate that benzene and the Ag(111) surface have a non-bonding interaction [78]. The electron energy loss spectroscopy (EELS) studies of benzene, pyridine, and pryazine on a Ag(111) surface conducted by

Avouris and Demuth found that the electronic transition energies are only weakly perturbed from their gas phase values by the Ag(111) substrate [68], while the UV photoemission spectra of benzene and anthracene adsorbed on Ag(111) strongly resembles that of gas phase benzene [69,73]. The lack of electronic perturbation of the adsorbate by the substrate allows comparisons between the electronic properties of aromatic molecular crystals and the electronic properties of the adsorbed layers. This greatly simplifies the theoretical description of the interfacial electronic structure and validates the use of adsorbate bulk parameters in the model calculations to be described shortly.

4.2 Energies of Image Potential States

The energetic position of the first EA level with respect to the hydrogenic $n = 1$ image potential state critically influences the properties of the interfacial $n = 1$ image potential state. Figure 4.1 shows the relative energies of these states. The kinetic energy spectra for a monolayer, a bilayer, and a trilayer of benzene physisorbed on Ag(111) appear in Figure 4.2. The peaks observed in the spectra fit all fit Hydrogenic progressions, substantiating their assignment as image potential states. The photon energy dependence of the monolayer spectra indicates that the occupied surface state also persists for the benzene monolayer. Layer adsorption generally moves the Ag(111) occupied surface state above the Fermi level due to quantum confinement, though the Ag(111) surface state does persist in the presence of a Kr monolayer. Table 4.2 lists these binding energies for the $n = 1$ image potential state as a function of layer thickness. The adsorption of a monolayer of benzene results in an increase in the binding energy of the $n = 1$ image state The $n = 1$ binding energy of -0.68 eV for benzene coverage in excess of a monolayer is less than the $n = 1$ binding energy of -0.77 eV for the Ag(111) surface. The $n = 1$ binding energy remains constant from a bilayer to 5 layers of benzene. The $n = 1$ binding energy of -0.80 eV for a monolayer and -0.65 eV for a bilayer of benzene on Cu(111) differ little from those of the current study [74]. Velic et al. did not report results for benzene coverage greater than a bilayer.

Figure 4.3 shows the kinetic energy spectra for naphthalene physisorbed on Ag(111), while Table 4.2 contains the measured binding energies. Adsorption of a monolayer of naphthalene increases the binding energy of the most bound excitation in the TPPE spectra from -0.77 eV for the clean Ag(111) surface to -0.96 eV, due to the strong coupling

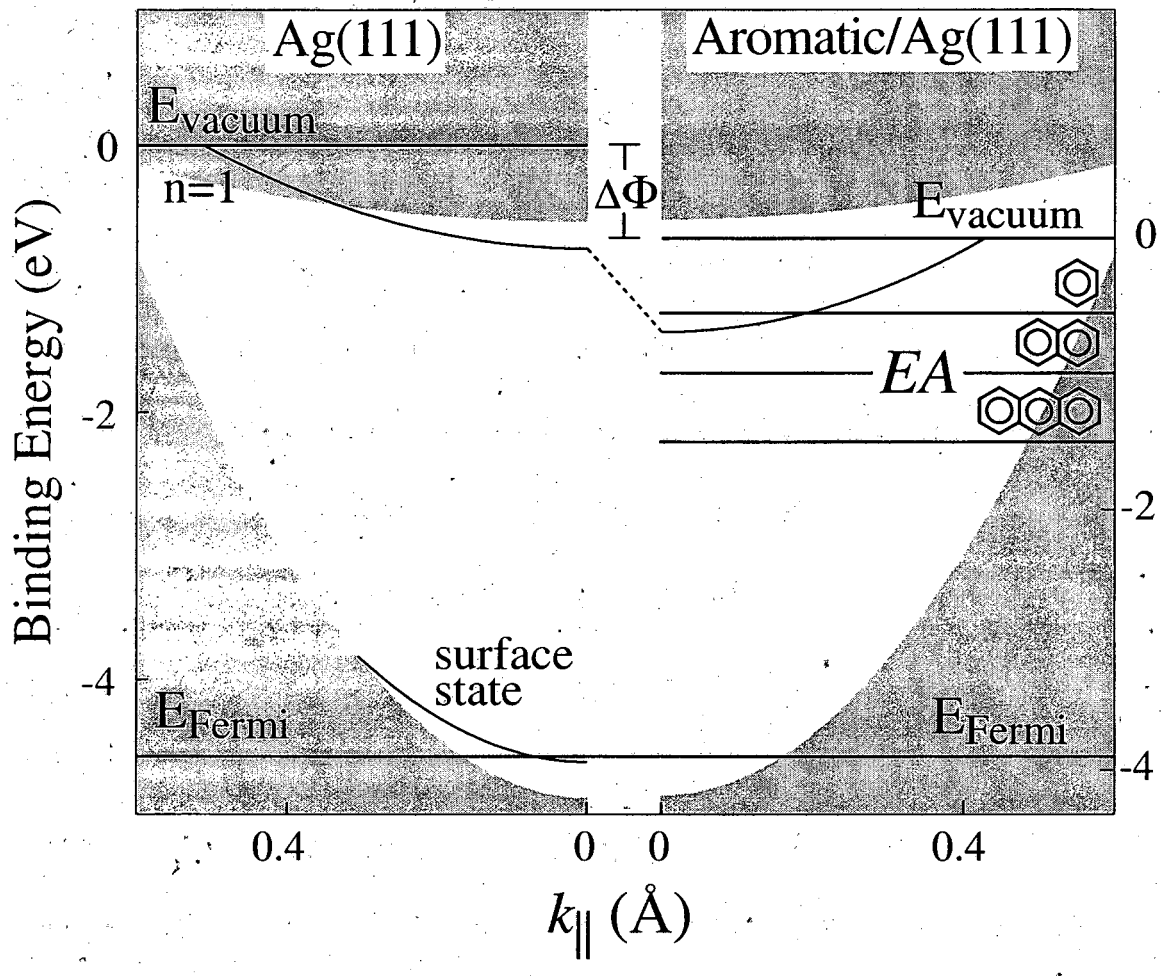

Figure 4.1: Projected bulk band structure for Ag(111) and aromatic adsorbate covered Ag(111). The change in workfunction, $\Delta\Phi$, moves the vacuum energy, E_{vac}, toward the center of the substrate band gap. The first electron affinity level, EA, of benzene, naphthalene, and anthracene appear to the right with binding energies of -0.6 eV, -1.0 eV, and -1.5 eV respectively. The $n = 1$ image potential state with the Ag(111) binding energy of -0.77 eV is shown as well.

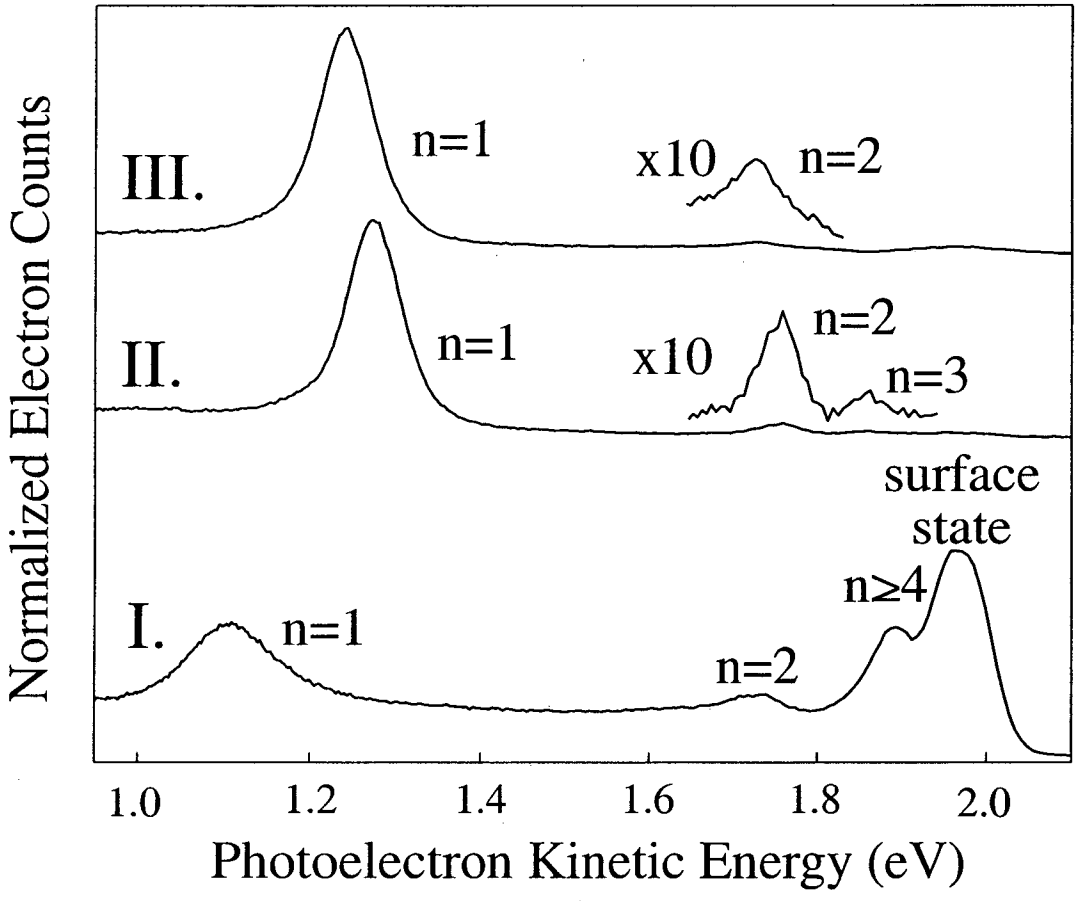

Figure 4.2: Photoelectron kinetic energy spectra for a monolayer I., a bilayer II., and a trilayer III. of benzene adsorbed on Ag(111). Variations in the photoelectron kinetic energy reflect variations in wavelength, workfunction, and binding energy. The persistence of the occupied surface state for the monolayer coverage results in the resonant excitation of $n \geq 4$ with 3.9 eV photons. Image state binding energies are reported in Table 4.2.

between the adsorbate first EA level and the $n = 1$ image potential state. The enhanced signal for the second and third excitations relative to the first peak in the naphthalene monolayer spectrum suggests that $n = 2$ and $n = 3$ interact strongly with the adsorbate second EA level. While a series of three peaks occur for the naphthalene monolayer, they do not fit an image potential state progression. The energy spacing between the first two excitations in the naphthalene monolayer, 0.74 eV, closely resembles the 0.71 eV energy spacing between the first two EA levels for gas phase naphthalene [34]. These results indicate that the excitations result from strong coupling between the image potential states and EA levels and cannot be classified as simply one or the other. While the excitations for the naphthalene monolayer do not correspond to image potential states, they will be referenced by the quantum number, n, throughout the remainder of this account for convenience. Adsorption of a second and then a third naphthalene layer result in reduced binding energies for all the excitations, as shown in Table 4.2. The peaks observed for the bi- and the trilayer of naphthalene do fit an image potential state progression. This indicates that the strongest interaction between the adsorbate EA levels and the interfacial image potential states occurs for the monolayer. A TPPE study of the naphthalene/Cu(111) interface observed similar trends in $n = 1$ binding energies [79].

The kinetic energy spectra for a mono- and a bilayer of anthracene adsorbed on Ag(111) appear in Figure 4.4. The adsorption of a monolayer of anthracene decreases the binding energy of $n = 1$ from -0.77 eV for clean Ag(111) to -0.70 eV. This should be contrasted with naphthalene and benzene, where the $n = 1$ state has binding energies of -0.96 eV and -0.84 eV [28]. Adsorption of the anthracene bilayer results in further reduction in the image potential state binding energies. The series of peaks for the monolayer and the bilayer fit hydrogenic progressions. While anthracene has a larger first EA level than either benzene or naphthalene, the peaks at the anthracene/Ag(111) interface have the smallest binding energies.

The $n = 1$ image potential states for monolayers of benzene, naphthalene, and anthracene all have significantly asymetric lineshapes. This asymetry may reflect the ultrafast dephasing of the image potential states [80]. For a two level system, the dephasing time, often termed T_2, results in a Lorentzian lineshape for the absorption spectrum,

$$\sigma(\omega) \propto \omega \,\mathrm{Im}\left[\frac{1}{(\omega_{eg} - \omega) - i\Gamma} + \frac{1}{(\omega_{eg} + \omega) - i\Gamma}\right] \tag{4.1}$$

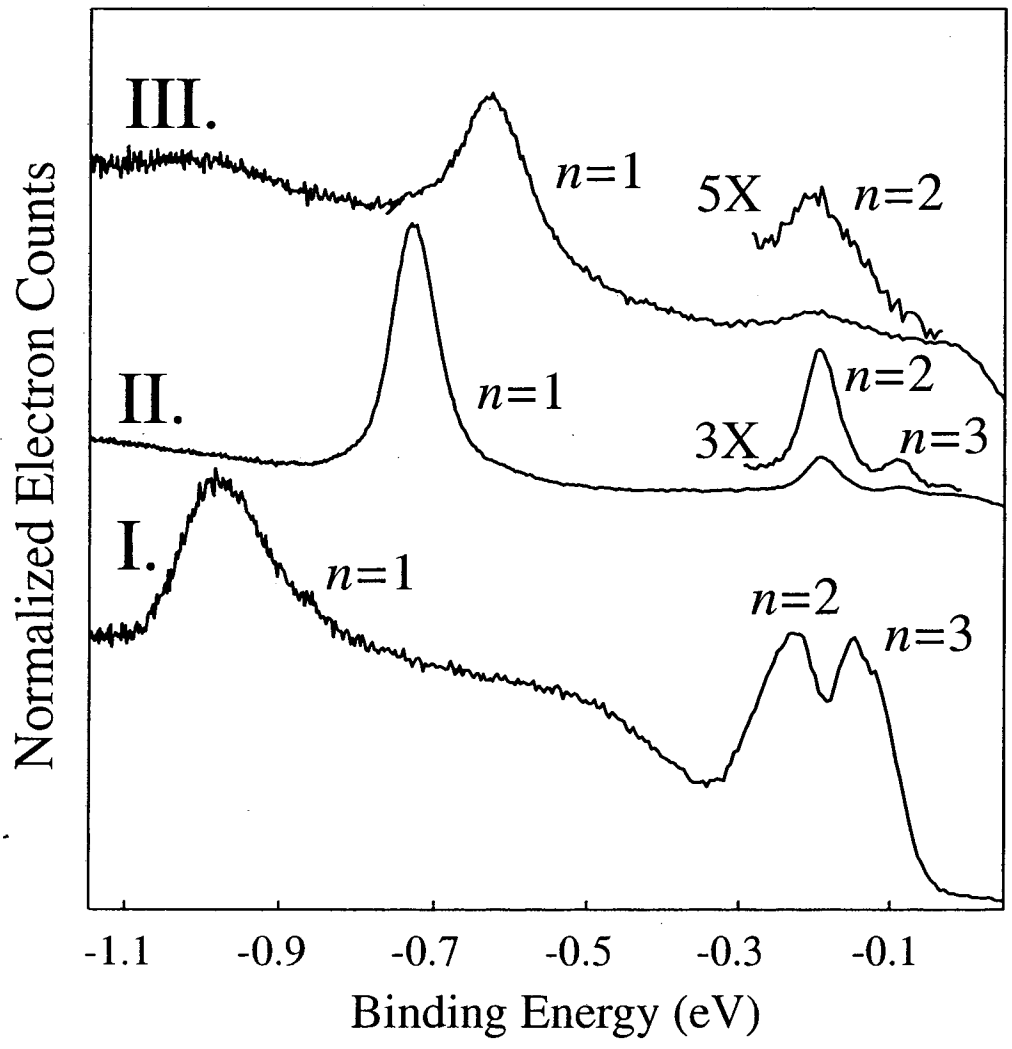

Figure 4.3: Photoelectron kinetic energy spectra for naphthalene. Spectra labeled I., II., and III. refer to mono-, bi-, and trilayer coverages. The binding energies can be found in Table 4.2.

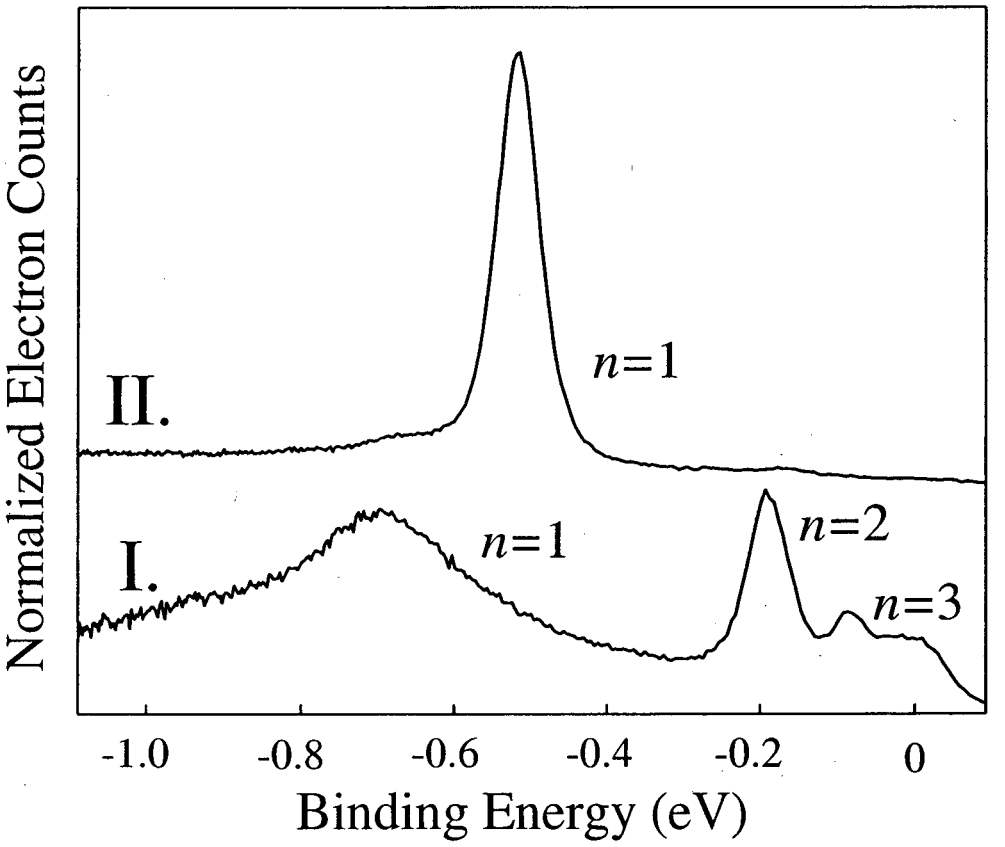

Figure 4.4: Photoelectron kinetic energy spectra for anthracene. Spectra labeled I. and II. refer to monolayer and bilayer coverages. The binding energies can be found in Table 4.2.

Table 4.1: Experimental and calculated image potential state binding energies (eV)

	$n=1$		$n=2$		$n=3$	
	Experimental	Calculated	Experimental	Calculated	Experimental	Calculated
naphthalene						
monolayer	-0.96	-0.94	-0.22	-0.23	-0.14	-0.11
bilayer	-0.74	-0.73	-0.20	-0.17	-0.09	-0.11
trilayer	-0.62	-0.64	-0.18	-0.16	–	–
anthracene						
monolayer	-0.70	-0.68	-0.19	-0.20	-0.09	-0.10
bilayer	-0.52	-0.53	-0.16	-0.17	–	–

$$\sigma(\omega) \propto \frac{4\omega^2\Gamma^2}{(\omega_{eg}^2 - \omega^2 - \Gamma^2)^2 + 4\omega^2\Gamma^2}, \tag{4.2}$$

where $\Gamma = 1/T_2$, w_{eg} is the transition frequency, and ω is the frequency of the electric field. The rotating wave approximation amounts to rejecting the second term in the adsorption line shape,

$$\sigma(\omega) \propto \frac{\Gamma^2}{(\omega_{eg} - \omega)^2 + \Gamma^2}, \tag{4.3}$$

resulting in a Lorentzian line shape. The second term usually makes an inconsequential contribution to the adsorption due to the lack of resonance, validating the rotating wave approximation. An acception occurs when Γ has a magnitude similar to $\hbar\omega_{eg}$. This acception will be most pronounced for a low energy transition with a very fast dephasing time.

While these ideas provide a potential explanation for the asymetric lineshapes observed for the aromatic monolayers, any application of these lineshape formulas must account for the fact that two photon photoemission minimally requires a three state system. For this reason, the linewidth at any given energy reflects the dephasing of both the pump and the probe excitations. Fortunately, a more detailed look at the TPPE process supports the use of a two level system for the appropriate conditions. the 4 eV pump pulse consists of the second harmonic of the 2 eV probe pulse. The linewidths would need to be larger than those observed dephasing of the pump excitation to invalidate the rotating wave approximation. For this reason, dephasing of the initial excitation cannot lead to the asymetric lineshape. The lineshape also narrows as the delay time between the pump and probe pulses increases. When the time delay between the pump and probe pulses exceeds

Table 4.2: Energies and Lifetimes for $n = 1$ at the Benzene/Ag(111) Interface

	Binding Energy(eV)		Lifetime(fs)	
	Experimental	Calculated	Experimental	Calculated
1 ML	-0.84	-0.89	20	16
2 ML	-0.68	-0.71	45	61
3 ML	-0.68	-0.68	50	45
4 ML	-0.68	-0.71	50	45
5 ML	-0.68	-0.72	50	51

the pulse widths, the $n = 1$ intermediate state must be in a population, rather than a coherence, to lead to photoemission by the probe pulse. For these longer delay times the linewidth will reflect only the dephasing of the probe step. These two factors strongly indicate that for a time delay longer than the pulse widths, the asymetric lineshape would result from dephasing of the coherence between the image potential state and the free electron final state. These experiments have the potential to further our understanding of the dynamic scattering of image potential states with the unoccupied electronic states of the adsorbate, as well as provide a more thorough understanding of how the dynamics of the electronic states under study manifest themselves in the TPPE kinetic energy spectrum.

An asymetric distribution of image potential state energies due to static inhomogeneity in the surface potential provides an alternative explanation. A transient hole burning experiment can distinguish between homogeneous and inhomogeneous broadening [81–83]. For inhomogeneously broadened peaks with widths significantly larger than the energy width of the laser pulse, a subset of the excited state population can be excited. For two photon photoemission, where a continuum of initial states populate the intermediate state, the resonance conditions differ from those of a two level system. Despite this important distinction, a psuedo-hole burning TPPE experiment can be conducted by decreasing the photon energy. For the case of an inhomogeneously broadened transition, a subset of the excited state ensemble can be populated by choosing a photon energy that can only populate the lower energy fraction of the population. Stated succinctly, the high energy side of the peak can be cut-off by choosing a small enough photon energy. If the inhomogeneity reflects static variations in local environment, the cut-off lineshape will not change as a function of delay time between the pump and probe pulses. For a homogeneously

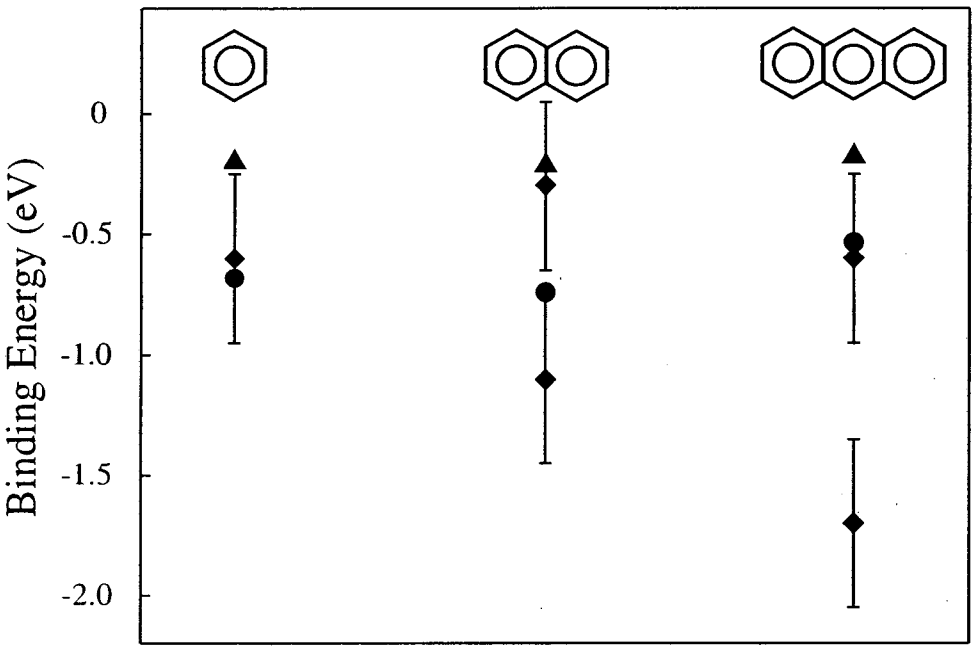

Figure 4.5: Comparison of the IPS and TPPE experimental binding energies [28, 72]. The results for benzene, naphthalene, and anthracene appear from left to right. The diamonds correspond to the IPS results for 2-3 adsorbate layers and the vertical lines represent the uncertainty of these measurements. The Figure also shows the TPPE results for adsorbate bilayers. The circles represent the $n = 1$ binding energies and the triangles represent the $n = 2$ binding energies. While the two techniques produce similar results for benzene and naphthalene, the IPS and TPPE results for anthracene differ significantly.

broadened peak, the lineshape will not change as a function of the photon energy, only the intensity of the signal. This technique would also be sensitive to dynamics intermediate between the static and fast modulation limits. For fluctuation times slow compared to the inverse of the frequency width of the peak, but fast compared to the decay of the excited state, the shape of the peak will change as a function of delay time between the pump and the probe pulses, a process often termed spectral diffusion. The validity of this approach has yet to be demonstrated, but may be applicable to all systems that exhibit linewidths on the order of tenths of an eV. This may apply to the early stages of electron localization, where the localized FWHM can exceed a third of an eV, and to polar adsorbate systems such as acetonitrile.

A comparison of the IPS results of Frank et al. and the TPPE results appear in Figure 4.5 [28, 72]. For benzene, naphthalene, and anthracene, peaks with similar binding energies are assigned as EA levels in the IPS study and image potential states in the TPPE

study. Additionally, the IPS spectra for anthracene contains a peak clearly absent from the TPPE spectra. Whether the different assignments correctly reflect different excitations remains unclear at this time. The absence of the first EA level in the TPPE spectra appears to indicate that the two techniques need not observe the same excitations. The excitation of substrate electrons, present in TPPE and absent from IPS, provides the primary distinction between the two techniques. Guided by this distinction, the cross section for excitation of image potential states with substrate electrons would appear to exceed that for excitation of an EA level.

4.3 Dynamics of Image Potential States

In addition to monitoring the layer dependent electronic structure, time resolved TPPE allows for the measurement of excited state lifetimes. The determination of the time scale for electron relaxation indicates the extent of coupling between the excited interfacial electron and the Ag(111) substrate. A physisorbed insulator, such as benzene on Ag(111), should lack low lying unoccupied electronic levels into which image state electrons can decay. To first approximation, the image state electron relaxation will be dominated by electron hole excitation in the metal, resulting in lifetimes proportional to the the image state wavefunction overlap in the metal. Partially occupied surface states also provide a decay path for image state electrons, but accounting for this effect involves a more sophisticated theoretical description of surface electron relaxation than the one presented in Sections 4.4.2 and 4.4.3 [84, 85].

Table 4.2 details the layer dependent evolution of the image state lifetimes for the benzene/Ag(111) interface. The $n = 1$ lifetime for a monolayer of benzene on Ag(111) is shorter than the $n = 1$ lifetime of 36 fs for the clean Ag(111) surface. This result suggests that adsorption of a benzene monolayer moves the $n = 1$ image state closer to the Ag(111) surface. The adsorption of a benzene monolayer also increases the $n = 1$ binding energy, which also supports the conclusion that the adsorption of the monolayer moves the $n = 1$ electron closer to the Ag(111) surface. The $n = 1$ lifetime increases to 45 fs for a bilayer of benzene. This result should be contrasted with that of Velic et al., where the bilayer $n = 1$ lifetime is half that of the monolayer lifetime. The 20 fs and 45 fs $n = 1$ lifetimes for mono- and bilayer benzene on Ag(111) measured in the current study are roughly the reverse of those for mono- and bilayer benzene on Cu(111) reported by Velic et al., 40 fs and 17 fs

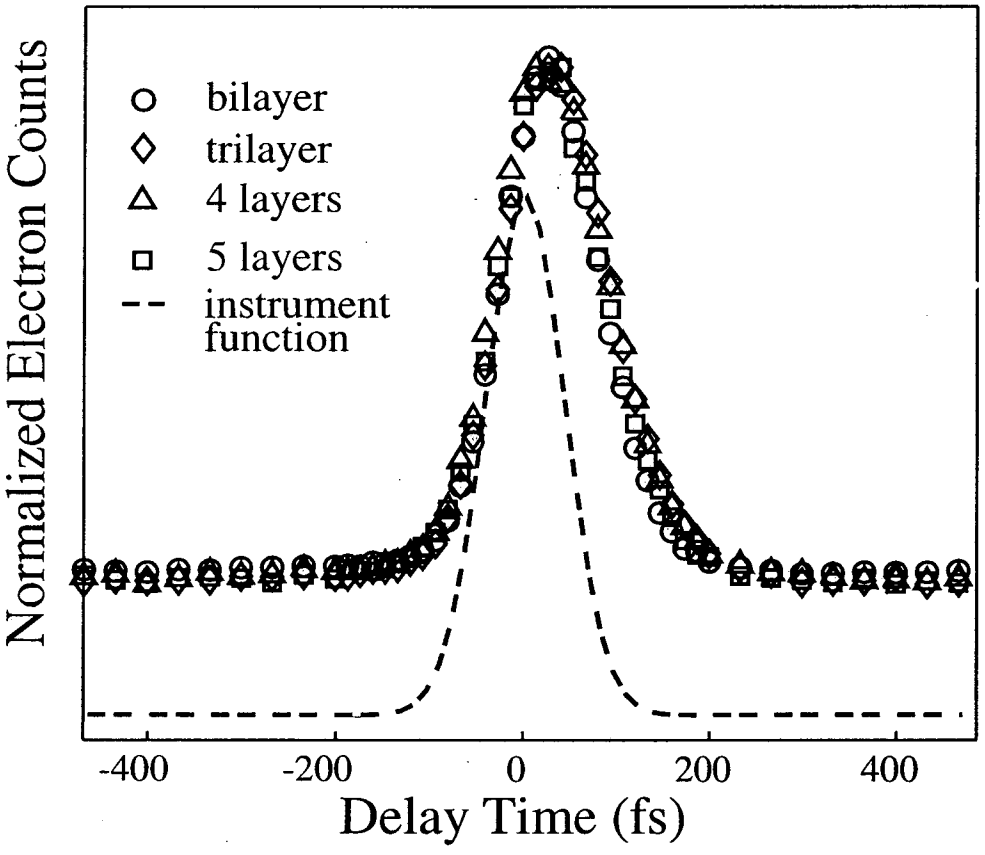

Figure 4.6: The instrument function and fs population dynamics of the $n = 1$ image state for 2 to 5 layers of benzene adsorbed on Ag(111). The dynamic traces clearly show the similarity of the $n = 1$ population dynamics for 2 to 5 layers of benzene. The $n = 1$ dynamics are fit by convolving the instrument function with an exponetial decay. The $n = 1$ lifetimes are reported in Table 4.2.

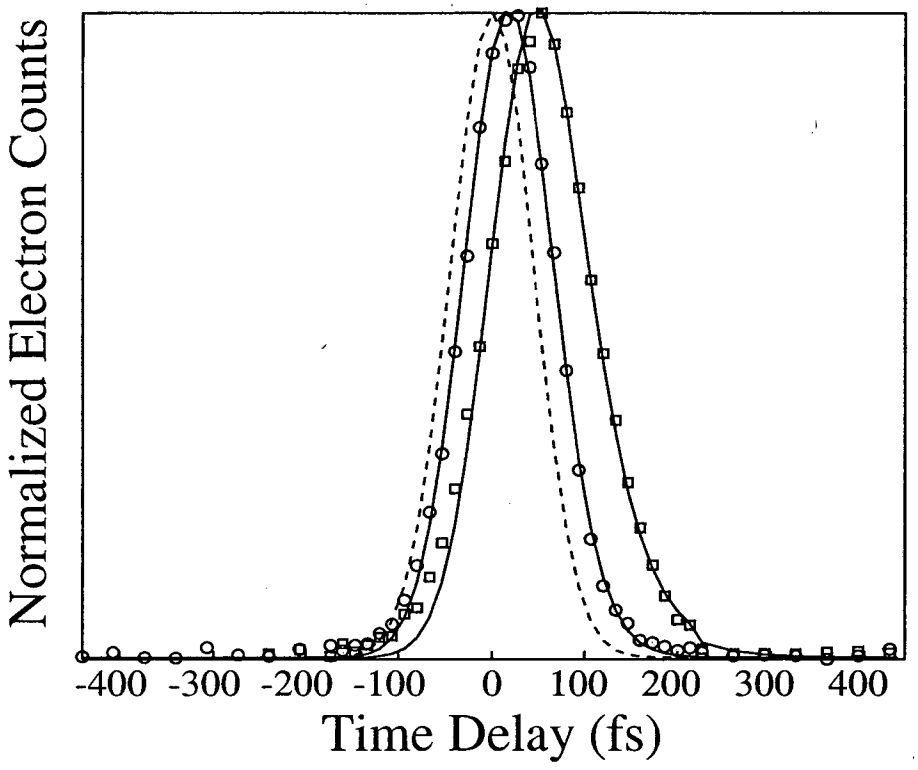

Figure 4.7: The population dynamics of the $n = 1$ image potential state for mono- and bilayer naphthalene. The circles refer to the monolayer data points and the squares to the bilayer data points. The fits to the experimental data appear as solid lines, while the dashed line represents the instrument function. The data clearly shows the similarity between the mono- and bilayer $n = 1$ dynamics for naphthalene. The lifetimes can be found in Table 4.3.

respectively [74]. Figure 4.6 illustrates the lack of change in the $n = 1$ lifetime when the benzene coverage increases from a bilayer to 5 layers. Lifetimes comparable to the clean Ag(111) surface and the lack of decay channels within the benzene layer necessitate a large electron density near the benzene/Ag(111) interface.

The $n = 1$ dynamics for mono- and bilayers of naphthalene and anthracene appear in Figures 4.7 and 4.8, while Table 4.3 contains the measured decay constants. The lifetimes of the excited states at the naphthalene/Ag(111) interface slowly increase with both the quantum number, n, and the layer thickness. While the lifetimes do increase with n, they exhibit a less pronounced n dependence that the n^3 increase in lifetime found for metal surfaces [26]. The gradual increase in lifetime with naphthalene coverage resembles neither the results for anthracene nor those for benzene [28]. The multilayer $n = 1$ lifetime does not vary from 2 to 5 layers of benzene, while the $n = 1$ lifetime for a bilayer of anthracene

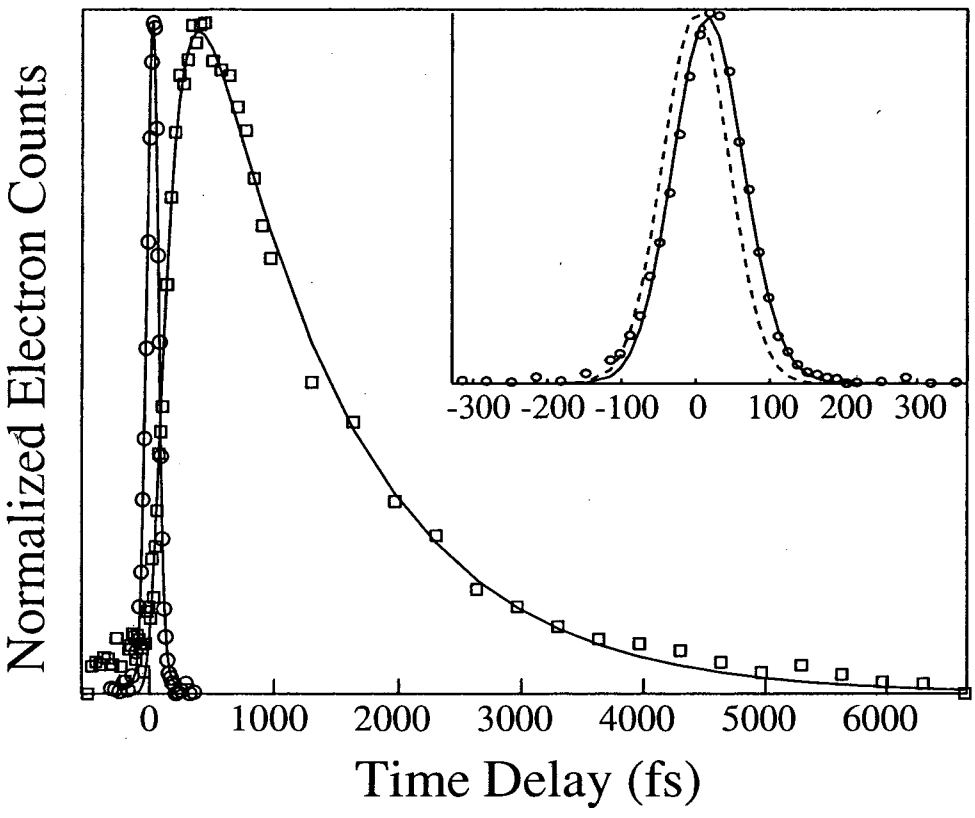

Figure 4.8: The population dynamics of the $n = 1$ image potential state for mono- and bilayer anthracene. The circles refer to the monolayer data points and the squares to the bilayer data. The data clearly shows the tremendous increase in $n = 1$ lifetime upon the adsorption of a second layer of anthracene. The inset shows the anthracene monolayer $n = 1$ dynamics along with the instrument function. The lifetimes can be found in Table 4.3.

exceeds that of a monolayer by a factor of 60. The comparatively long $n = 1$ lifetime provides the necessary interaction time between the electron and the anthracene layer for dynamic localization of the $n = 1$ image potential state electron [66]. The 1.1 picosecond decay constant for the bilayer refers to the lifetime of the localized state.

4.4 Theoretical Modeling of Image Potential States

Meaningful theoretical calculation of interfacial unoccupied electronic structure and electron dynamics requires an appropriate treatment of the adsorbate layer electronic structure. While the dielectric continuum model effectively accounts for the influence of an adsorbate with a single attractive EA level, such as Xe and benzene, the model cannot

Table 4.3: Experimental and calculated image potential state lifetimes (fs)

	$n = 1$		$n = 2$		$n = 3$	
	Experimental	Calculated	Experimental	Calculated	Experimental	Calculated
naphthalene						
monolayer	20 ± 10	25	30 ± 10	125	70 ± 10	90
bilayer	40 ± 10	32	80 ± 10	280	120 ± 20	90
trilayer	60 ± 10	44	100 ± 30	440	–	–
anthracene						
monolayer	20 ± 10	100	49 ± 4	220	110 ± 10	230
bilayer	1100 ± 200	1000	–	–	–	–

account for the presence of two attractive EA levels separated by a band gap [28, 86–88]. Anthracene and naphthalene, which both have two attractive EA levels, require a more sophisticated treatment of the layer electronic structure. The present study uses the two band nearly free electron (NFE) model in the layer for anthracene and naphthalene.

4.4.1 Numerical Procedures

Numerical integration of the time-independent Schrödinger equation provides the energies and wavefunctions for image potential states at interfaces. For the solution of the dielectric continuum model the amplitude and slope of the two band NFE model for the projected bulk band structure of Ag(111) provides the initial boundary condition at the metal/dielectric interface. The vanishing of the wavefunction at infinity provides the second boundary condition. For a given energy, the slope and amplitude of the wavefunction at the metal/dielectric interface can be determined analytically. These values are then numerically propagated through the dielectric layer out into the vacuum. The eigen vectors of the Hamiltonian correspond to the wavefunctions that vanish by 200 Å outside the dielectric layer, while the eigen values correspond to the initial energies that provide the eigen vectors.

The initial conditions for the two band NFE layer on a two band NFE substrate provide the sole distinction between the two models. For the two band NFE layer on a two band NFE substrate, the slope and amplitude of the wavefunction at the metal/layer interface is matched to the slope and amplitude of the wavefunction in the adlayer. These can be determined analytically. The matching of the wavefunctions at the metal/layer interfaces uses the wavefunction phase as a fitting parameter. This then determines the slope and amplitude of the wavefunction at the layer/vacuum interface, which provides the

initial conditions for the numerical integration through the dielectric continuum potential in the vacuum.

The dielectric continuum model potential must be modified to avoid singularities at the metal/dielectric and the dielectric/vacuum interfaces. To avoid the singularity at the metal/dielectric interface, the potential is cut-off at the Fermi energy near the metal surface. The singularity at the dielectric/vacuum interface is eliminated by linearly interpolating the potential between $V(t-b/2)$ and $V(t+b/2)$, where t represents the layer thickness and b is the width of the interpolation. The calculations reported herein set b to 3 Ångstroms(Å). A singularity at the layer/vacuum interface must also be avoided for the two band NFE on a two band NFE model as well. This was achieved by cutting off the potential in the vacuum 1.3 Å outside the layer for naphthalene and 2.3 Å for anthracene. These values give the best agreement between calculation and experiment.

The lifetime of the image potential state can also be estimated from the calculated wavefunctions. The lifetime of the image state is estimated from the product of the calculated electron density in the metal and an experimentally determined lifetime for an excited electron in bulk silver at the energy of the image potential state [89,90]. While this does not explain how scattering events in the metal cause image potential state decay, it does provide a powerful tool for testing the validity of the electrostatic potentials used to describe the electrons interaction with the layer.

4.4.2 Applications of the Dielectric Continuum Model

The benzene layer thickness, dielectric constant, and electron affinity represent the significant input parameters for the dielectric continuum model. The equilibrium distance of 2.4 Å between adsorbed benzene and the Ag(111) surface calculated by Anderson et al. is used to estimate the thickness of the benzene monolayer [78]. A 5 Å estimate for the thickness of each additional layer is derived from an averaged nearest neighbor distance in crystalline benzene [91]. The use of a bulk benzene dielectric constant and electron affinity is validated by the weak chemical interaction between benzene and the Ag(111) surface. Ideally, the solid state dielectric constant and electron affinity of crystalline benzene would be used, but such values do not appear to exist in the literature. Condensed phase values, such as those of the liquid can be substituted. The dielectric constant and electron affinity of liquid n-heptane were successfully employed to model the binding energy and lifetime

of image states at the n-heptane/Ag(111) interface [65]. The present calculation utilizes a liquid benzene dielectric constant of 2.3 [92]. An attractive electron affinity of 0.6 eV results in the closest agreement to experiment and differs little from the 0.5 eV electron affinity of liquid benzene [93]. Velic et al. used the -1.15 eV gas phase electron affinity of benzene for modelling the benzene/Cu(111) interface. While the gas phase EA agrees with the assignment of the final state resonance as the benzene first electron affinity level, the calculated image potential state lifetimes exceed the experimental lifetimes by many orders of magnitude [74]. The use of a gas phase electron affinity in the dielectric continuum model should not correctly represent the layer electronic structure. The Xe/Ag(111) interface illustrates the importance of using condensed phase parameters when modeling interfacial unoccupied electronic structure. A model of the Xe/Ag(111) interface which uses the attractive electron affinity of solid state Xe reproduces experimentally observed Xe quantum wells [27,87], while the use of the repulsive gas phase electron affinity of Xe in the same model would not account for this result.

The calculated and experimentally measured binding energies and lifetimes of $n = 1$ for 1 to 5 layers of benzene are represented in Figure 4.9. The calculated $n = 1$ binding energies and lifetimes change significantly from a monolayer to a bilayer of benzene, but vary little from 2 to 5 layers. Figure 4.10 shows the calculated $n = 1$ wavefunctions for 1 to 5 layers. Inspection of the wavefunctions in Figure 4.10 and the layer dependent model potential in Figure 4.11 clearly shows the $n = 1$ image potnetial state electron to be trapped in the screened image potential within the benzene layer. The trapped image electron resides primarily within the first 2 benzene layers even when the coverage exceeds a bilayer, while the amplitude of the evanescent wave in the metal varies little with coverage for multilayer benzene. The lack of substantial change in the calculated $n = 1$ image state wavefunctions results in weakly changing binding energies and lifetimes for multilayer benzene. Trapping of the electron in the screened image potential in the layer results in a large image state electron density in the metal and $n = 1$ image potential state lifetimes comparable to those of the clean surface.

While treating the benzene layer as a structureless dielectric successfully models the $n = 1$ image state, which has a binding energy larger than the layer electron affinity, the model does not appear capable of reproducing binding energies for image states above the electron affinity level. The dielectric continuum model predicts that the higher image state binding energies should increase as the coverage increases due to benzene quantum

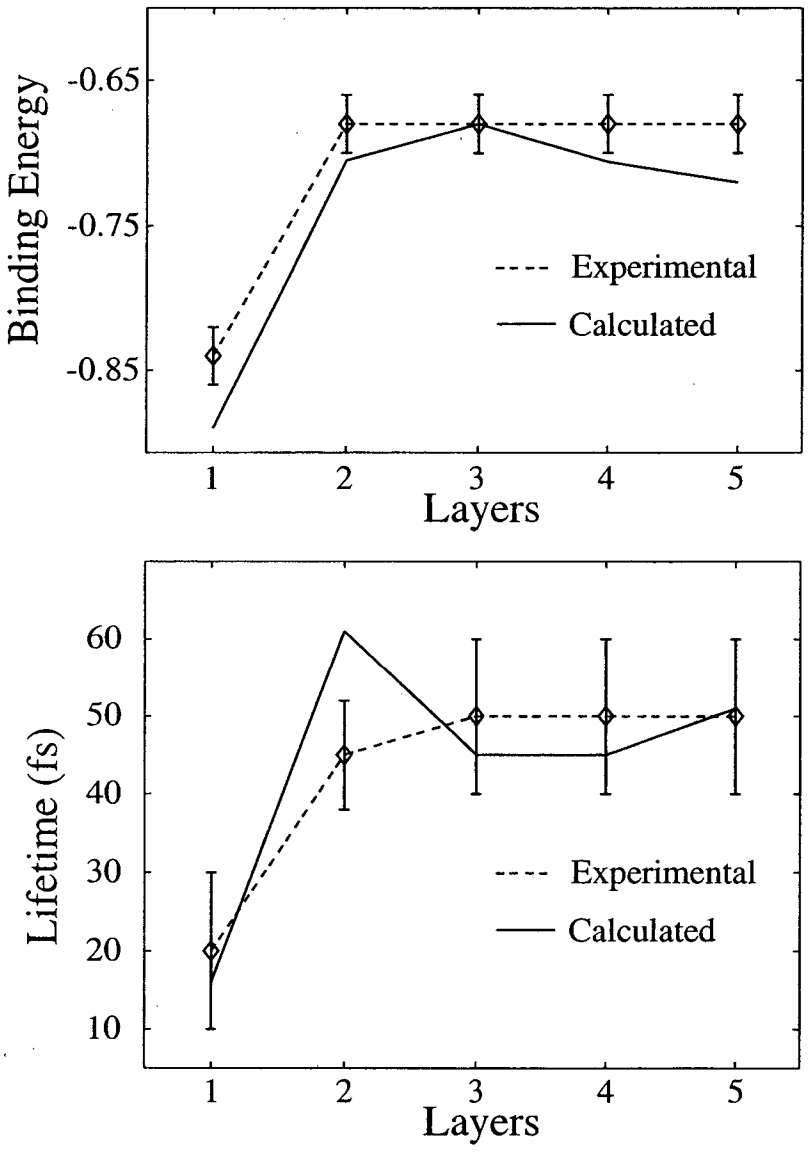

Figure 4.9: Comparison between the calculated and measured $n = 1$ binding energies and lifetimes as a function of layer thickness. The weak oscillation in the calculated lifetime does not occur in the experimental data. The exaggerated layer dependent changes in the calculated lifetimes reflect the abrupt changes in the model potential at the layer/vacuum interface. Calculated image state lifetimes for the Xe/Ag(111) interface also exhibit exaggerated lifetime oscillations [27].

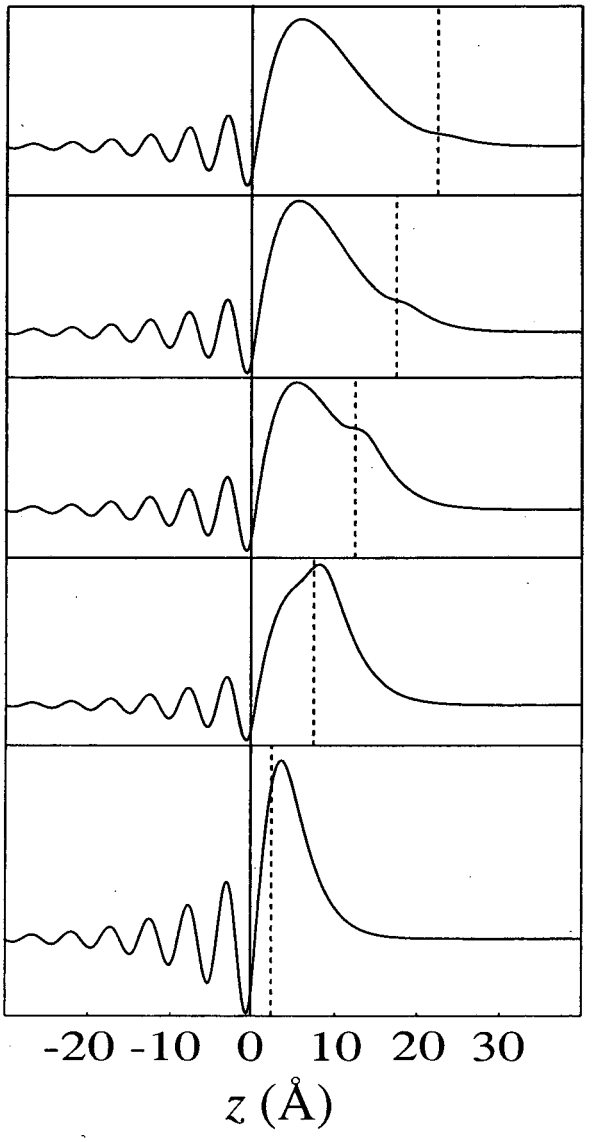

Figure 4.10: The $n = 1$ calculated wavefunction for 1, at the bottom, to 5 layers of benzene, at the top, adsorbed on Ag(111). The abscissa corresponds to the distance from the metal surface, with negative values of z residing in the substrate and positive values of z residing in the layer and vacuum. The straight vertical line represents the substrate/layer interface, while the dashed vertical line represents the layer/vacuum interface. The wavefunctions demonstrate that the electron resides primarily within the screened image potential in the benzene layer (see Figure 4.11), which accounts for the layer independence of the binding energies and lifetimes for multilayer benzene. The sharp variations in the wavefunctions at the substrate/layer and layer/vacuum interfaces reflect the abrupt changes in the model potential and represent a major limitation of the dielectric continuum model.

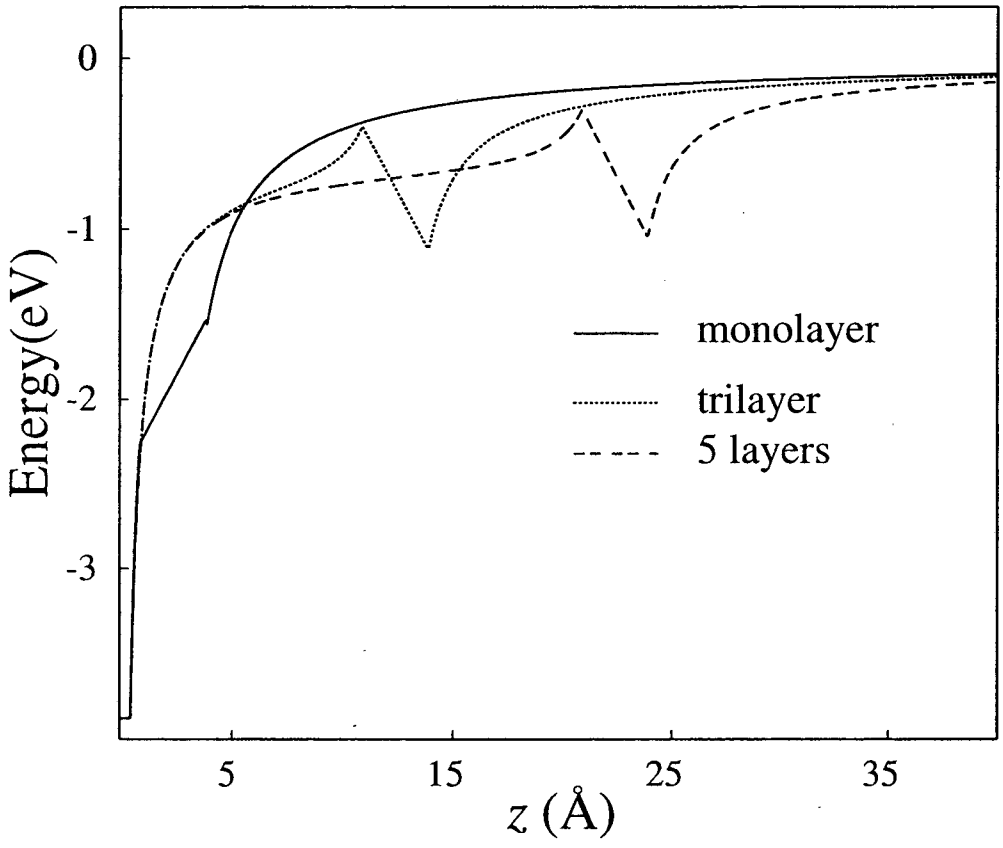

Figure 4.11: The model potential for a monolayer, trilayer, and 5 layers of benzene adsorbed on Ag(111). The odd shape of the monolayer potential results from the narrow layer width, 2.4 Å, and the 3 Å interpolation width. Despite the sensitivity of the monolayer potential to the interpolation width, setting b to 1 Å did not significantly change the calculated binding energy and lifetime for the monolayer.

well formation. The $n = 2$ binding energies, -0.21 eV, -0.19 eV, and -0.19 eV for a monolayer, bilayer, and trilayer of benzene respectively, do not agree with the predicted binding energies. The dielectric continuum model exhibited a related inability to successfully predict the binding energies of image states above the Xe band minimum for the Xe/Ag(111) interface [87]. The band properties of the overlayer influence quantum well formation, as reflected in the superior results for a layer potential that explicitly accounts for the Xe conduction band structure [27, 87]. The inability of the dielectric continuum model to accurately account for the benzene band structure may cause the model to predict quantum well formation for $n = 2$ in the benzene layer when quantum well states do not appear experimentally.

Once the electron affinity used in the dielectric continuum model exceeds 0.5 eV, the $n = 1$ image potential state will be trapped in the screened image potential in the layer, as seen for benzene [28, 86]. While this behavior agrees with the experimental finding for benzene, the model fails to successfully explain the experimental results for anthracene. This can be seen in Figure 4.12, where the experimental and theoretical binding energies and lifetimes for bilayers of a range of molecules appear. The measured $n = 1$ lifetime for a bilayer of anthracene exceeds the calculated lifetime by an order of magnitude, while the calculated binding energy exceeds the measured binding energy by nearly an eV. The two band NFE layer on a two band NFE substrate results in significantly better agreement between experiment and theory, and provides an explanation for the failure of the dielectric continuum model.

The findings of a TPPE investigation of the hexafluorobenzene/Cu(111) interface provide an interesting contrast to the results found for the anthracene/Ag(111) interface [94, 95]. Similar to anthracene, hexafluorobenzene has a large attractive EA level of 1.3 eV that derives from the C-F σ^* orbitals as well as a π^* EA level at about 0.6 eV. Unlike anthracene, a series of image potential states do appear in the layer with larger than hydrogenic binding energies, as predicted by the dielectric continuum model. The first two EA levels of hexafluorobenzene should be about 0.7 eV apart, roughly a half an eV closer than the first two EA levels of anthracene. The closer proximity of the hexafluorobenzene EA levels may result in band overlap between the first two EA levels, while anthracene will have a band gap.

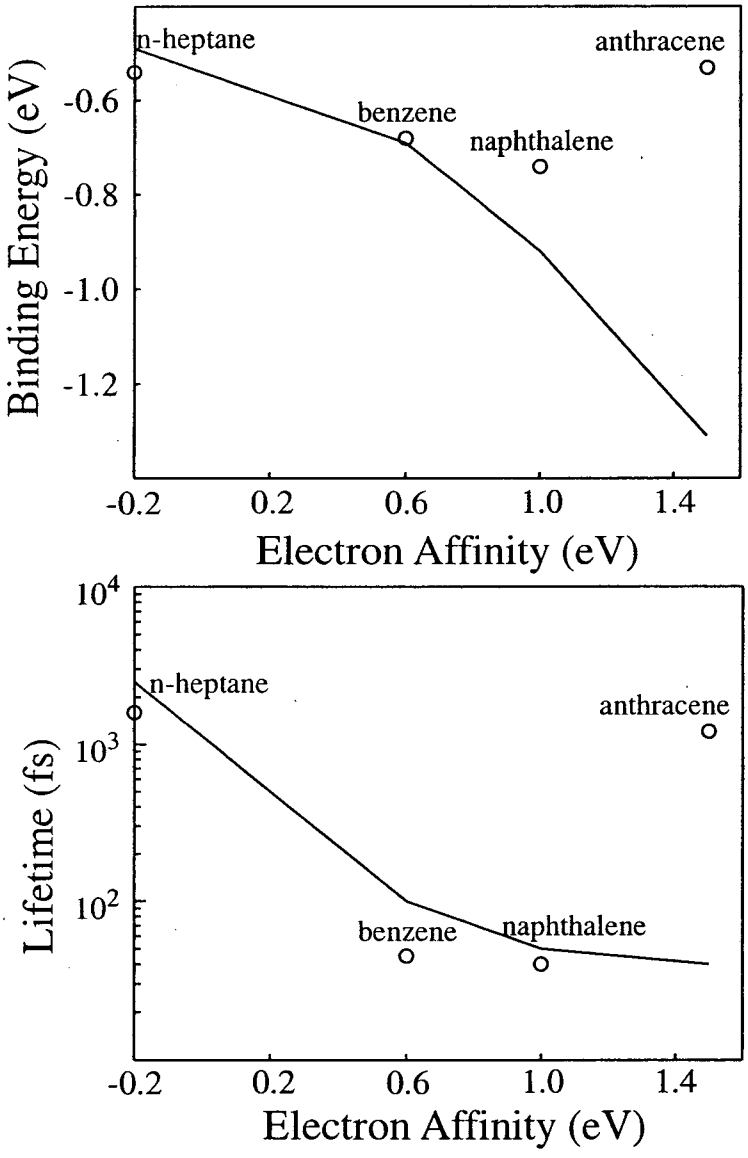

Figure 4.12: Experimental and calculated values for (a) the binding energies and (b) the lifetimes of the $n = 1$ image potential state as a function of EA. These values correspond to bilayer coverages. The calculations use typical values for layer thickness and dielectric constant, with the EA as the only varied parameter. This demonstrates the significant influence of the EA in the dielectric continuum model, but does not necessarily obtain the best agreement with experimental results. By choosing material specific parameters, excellent agreement has been achieved for benzene and n-heptane [28, 65]. The dielectric continuum model does not reproduce experimental values for anthracene when appropriate parameters are chosen.

4.4.3 Applications of a Two Band NFE Model in the Adsorbate Layer

The construction of the overlayer band structure depends critically on the selection of the parameters for the two band NFE model. Significant parameters include the layer crystallographic constant (a), the band minima (EA), m^*, and gap ($2V_g$). Literature values for the overlayer lattice constants and the molecular orientations within the crystal unit cell do not exist for thin layers of naphthalene and anthracene adsorbed on Ag(111). No theoretical value exists for the distance between adsorbed naphthalene or anthracene and the Ag(111) surface, but the similar adsorbate orientation of benzene, naphthalene, and anthracene [72] makes the theoretical value of 2.4 Å for benzene on Ag(111) a reasonable estimate [78]. Less information exists for the multilayer thickness, so an average of the anisotropic nearest neighbor distance in the molecular crystal, 7.5 Å for naphthalene and 8.5 Å for anthracene, provides a reasonable estimate [91]. The lattice constant, a, in the direction normal to the surface determines the Brillouin zone boundary, π/a. The present calculation uses the multilayer lattice constant for a, a choice that will increase in accuracy as the layer thickness increases. The calculation utilized dielectric constants of 3 for naphthalene and 4 for anthracene [96, 97].

The aromatic molecular crystal literature assists in the determination of the band minima and band gap widths [29]. Silinsh and Čápek provide a phenomenological method for calculating the crystal EA levels from the gas phase electron affinity levels and the electronic polarizability of the crystal [29]. The present calculations use the slightly modified values for the band minima of -1.0 eV and -0.2 eV for naphthalene and -1.5 eV and -0.2 eV for anthracene [29, 34, 35]. While the position of the first band minimum can be assigned independently of all other parameters, the position of the second band minimum depends on the band m^* and the band gap width. The model uses m^* of 1.5 m_e for naphthalene and 1.0 m_e for anthracene, consistent with the experimental findings of Schön et al. [33], and band gap widths of 0.5 eV for naphthalene and 1.3 eV for anthracene. These parameters result in a first band width of 0.37 eV for naphthalene and 0.17 eV for anthracene, as can be seen in Figures 4.13 and 4.14.

Tables 4.2 and 4.3 present the experimental and theoretical results for image potential states at the naphthalene/Ag(111) and the anthracene/Ag(111) interfaces. The model successfully reproduces the layer dependent trends in binding energies and lifetimes for both naphtalene and anthracene, as shown in Figure 4.15. Two results of the binding en-

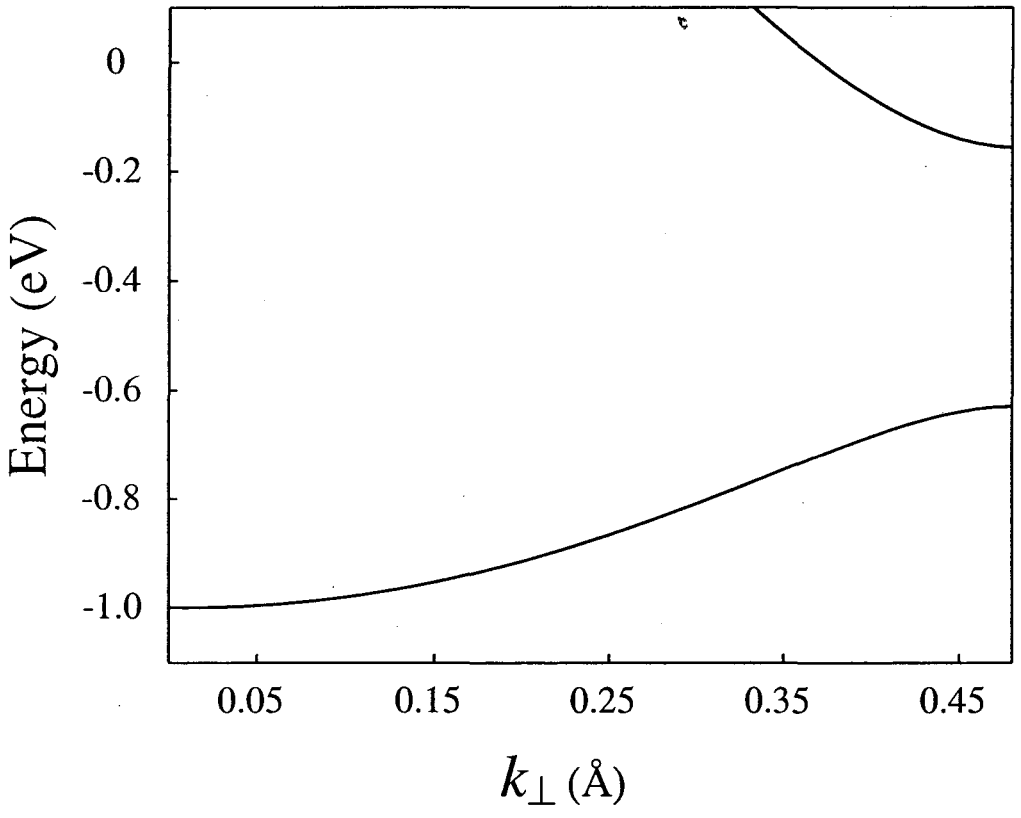

Figure 4.13: The conduction band structure for naphthalene. The Figure depicts the two band nearly free electron band structure of the first two unoccupied conduction bands of naphthalene used in the theoretical calculations.

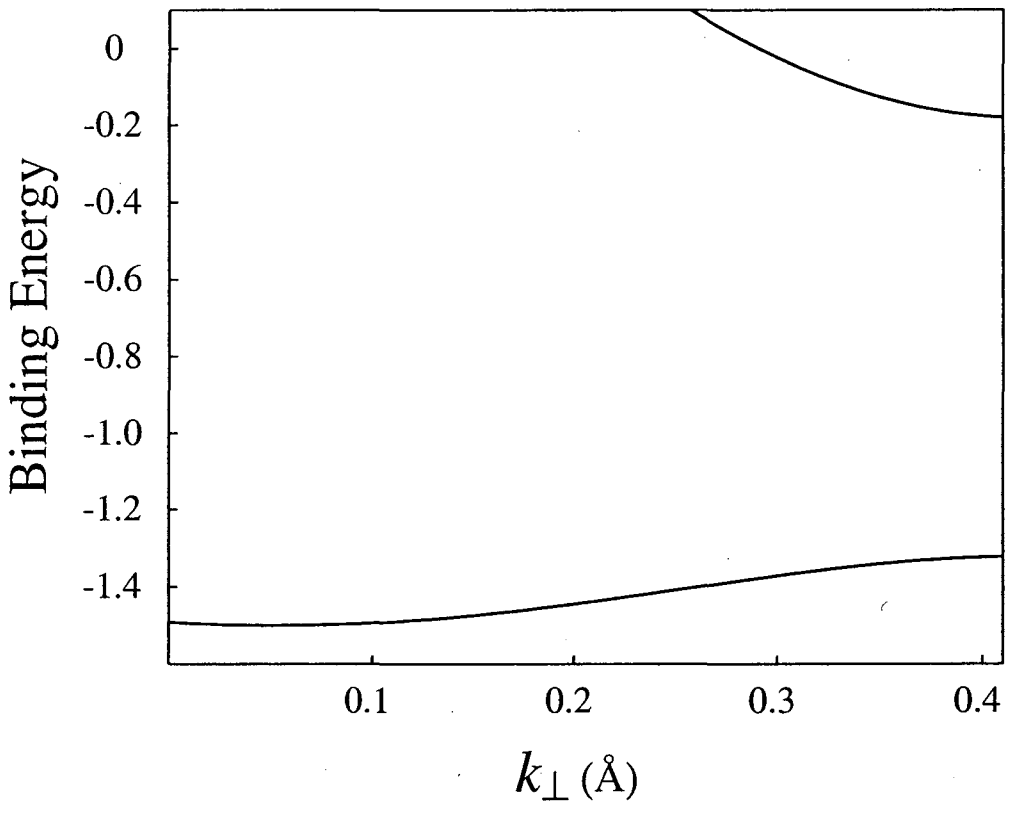

Figure 4.14: The conduction band structure for anthracene. The Figure depicts the two band nearly free electron band structure of the first two unoccupied conduction bands of anthracene used in the theoretical calculations.

ergy calculations should be emphasized. Firstly, the model effectively accounts for both the transition from the hybridized states of the naphthalene monolayer to the image potential states of the naphthalene bi- and trilayer. Secondly, it reproduces smaller $n = 1$ binding energies for anthracene than for naphthalene, despite the larger EA of anthracene. The model accounts for both the layer and adsorbate dependent trends in $n = 1$ lifetimes. It also reproduces the gradual layer dependent increase in $n = 1$ lifetime for naphthalene and the dramatic layer dependent increase in the $n = 1$ lifetime for anthracene. The calculated lifetimes for the higher image potential states vary more strongly from experiment than those for $n = 1$. The model also predicts quantum well formation for $n = 3$, a prediction unsubstantiated by experiment.

The significant variations in image potential state binding energies and lifetimes for benzene, naphthalene, and anthracene layers reflect the variations in the unoccupied electronic structures of the aromatic molecules. The conduction bands of naphthalene and anthracene, pictured in Figures 4.13 and 4.14, dictate the strength of the interaction between the image potential states and the adsorbate EA levels. For image potential states degenerate with the first naphthalene conduction band, the resultant wavefunction will have a large electron density in the layer and the substrate. This can be seen in the calculated $n = 1$ wavefunctions for the naphthalene/Ag(111) interface shown in Figure 4.16. For image potential states degenerate with the layer band gap, like $n = 1$ for anthracene, the wavefunction will be exponentially damped in the layer. This results in a small electron density in the layer and the substrate as shown in Figure 4.17. The experimental $n = 1$ lifetimes for naphthalene dictate that $n = 1$ image potential states with binding energies from -0.96 eV to -0.62 eV be degenerate with the first naphthalene conduction band. Without a relatively large conduction band width, the calculation would not be able to reproduce the short lifetimes observed for multilayer naphthalene.

As mentioned previously, the calculated lifetimes presented in Table 4.3 result from the calculated electron density in the substrate and do not account for image potential state decay into the unoccupied electronic states of the layer. The theory results in calculated lifetimes shorter than the experimental lifetimes for anthracene, even though the model does not account for electron decay into the layer. This suggests a weak interaction between the image potential states and the EA levels of anthracene.

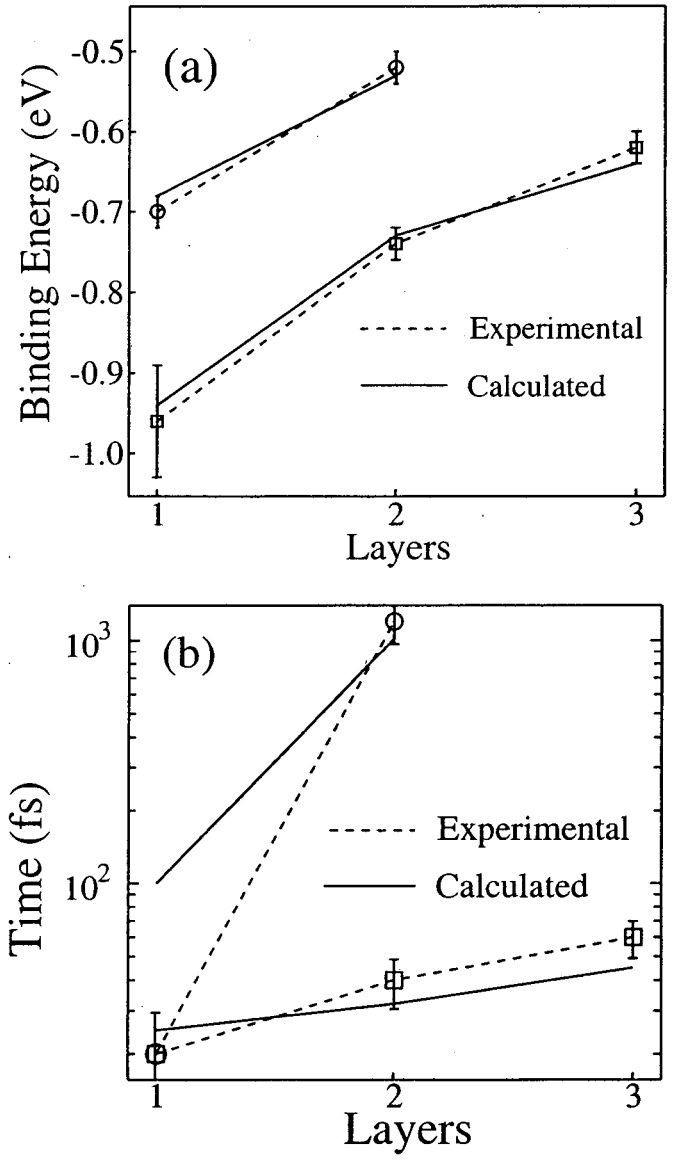

Figure 4.15: Comparison between the calculated and measured $n = 1$ binding energies (a) and lifetimes (b) as a function of layer thickness. The circles correspond to anthracene and the squares to naphthalene. The theoretical calculations successfully reproduce the layer dependent trends in $n = 1$ image potential state binding energies and lifetimes for both naphthalene and anthracene.

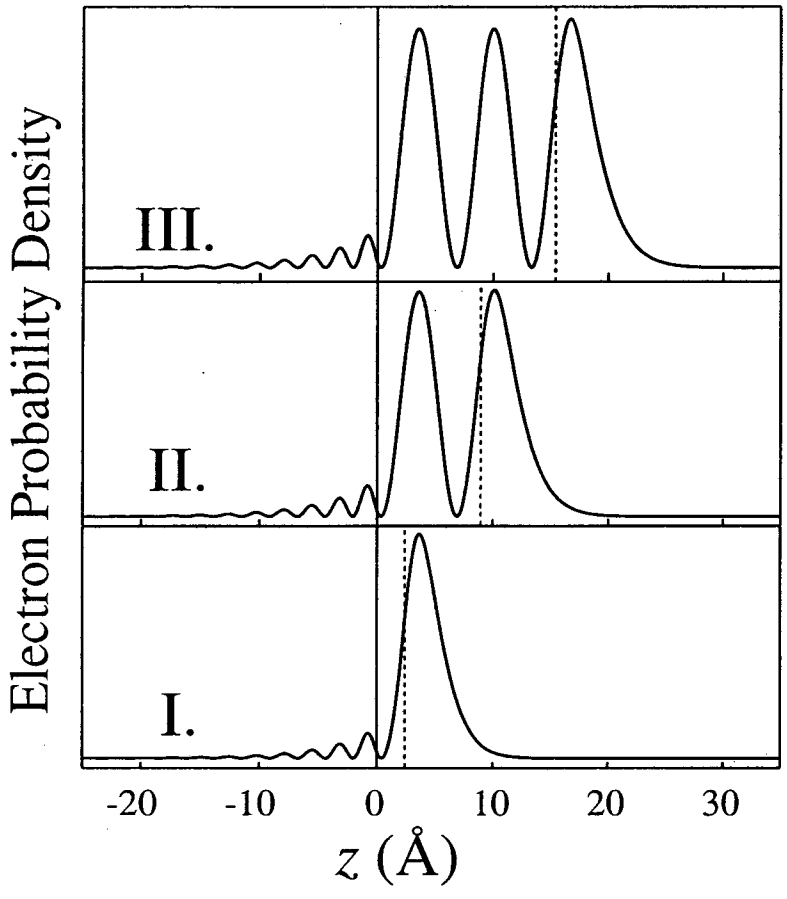

Figure 4.16: The calculated $n = 1$ image potential state probability density for naphthalene. The abscissa corresponds to the distance from the metal surface, with negative values of z residing in the substrate and positive values of z residing in the layer or vacuum. The solid vertical line refers to the substrate/layer interface, while the dashed vertical line refers to the layer/vacuum interface. The $n = 1$ energies for naphthalene reside in the first conduction band of the layer and result in larger $n = 1$ electron densities in both the layer and substrate. The wavevector of the wavefunction in the naphthalene layer determines the distance between the nodes in the layer.

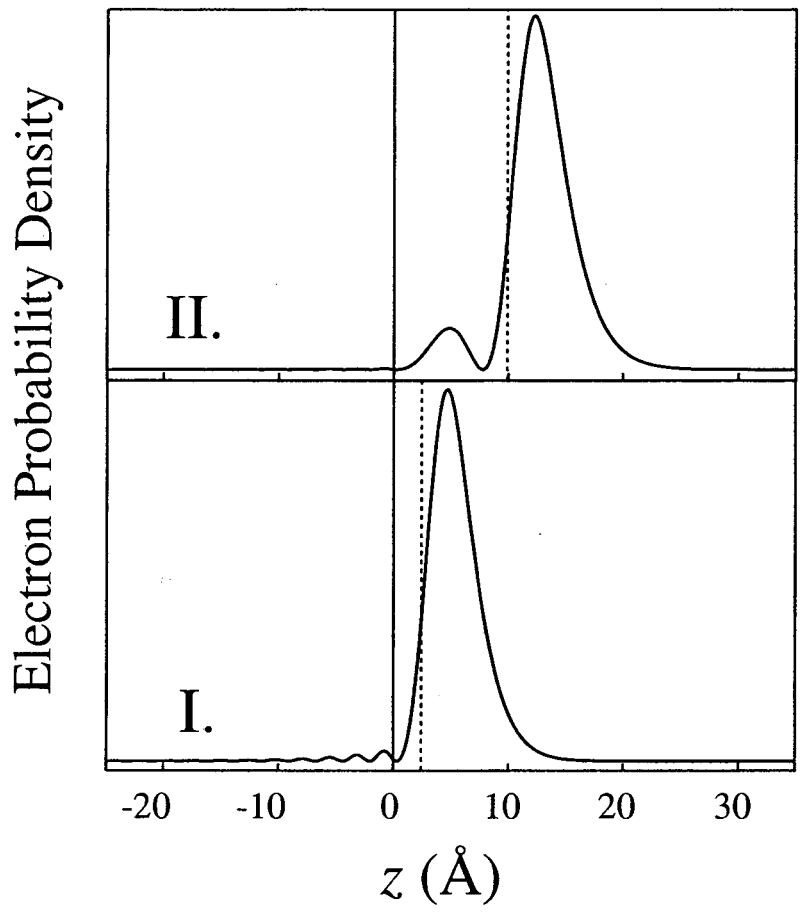

Figure 4.17: The calculated $n = 1$ image potential state probability density for anthracene. The abscissa corresponds to the distance from the metal surface, with negative values of z residing in the substrate and positive values of z residing in the layer or vacuum. The solid vertical line refers to the substrate/layer interface, while the dashed vertical line refers to the layer/vacuum interface. The $n = 1$ energies for anthracene reside in the layer band gap and result in small $n = 1$ electron densities in both the layer and substrate.

4.5 Summary and Conclusions

The layer dependent evolution of the benzene/Ag(111), the naphthalene/Ag(111), and the anthracene/Ag(111) unoccupied electronic structure and electron dynamics have been investigated with time and angle resolved TPPE. Adsorption of a monolayer of benzene moves the $n = 1$ image state electron closer to the metal, as reflected in the increase in the $n = 1$ binding energy and the decrease in the $n = 1$ lifetime. Adsorption of a bilayer decreases the binding energy and increases the lifetime of the $n = 1$ image potential state. The lifetime and binding energy remain constant from a bilayer to 5 layers of benzene. The excitations in the TPPE spectra for a monolayer of naphthalene do not fit a hydrogenic progression, unlike the peaks for benzene and anthracene, as well as higher coverages of naphthalene. The peaks for the naphthalene monolayer result from the hybridization of the image potential states with the electron affinity levels of naphthalene. While the lifetimes and binding energies for benzene and naphthalene do not differ significantly, the multilayer results for napthalene do change with coverage, unlike the multilayer results for benzene. The binding energies and lifetimes for anthracene differ significantly from those seen for benzene and naphthalene. These differences demonstrate the tremendous variation in the coupling between the image potential and the EA levels. Firstly, the $n = 1$ binding energies for benzene and naphthalene exceed those for anthracene, even though anthracene has the largest EA. Secondly, the 1.1 picosecond lifetime for the $n = 1$ state for a bilayer of anthracene exceeds the $n = 1$ lifetimes for bilayers of naphthalene and benzene by over an order of magnitude.

A dielectric continuum model successfully reproduces the trends in $n = 1$ binding energy and lifetime for benzene. Analysis of the model potential and the calculated wavefunctions shows the layer independence of the multilayer $n = 1$ lifetimes and binding energies to result from the trapping of the electron in the screened image potential within the benzene layer. The dielectric continuum model accounts for the influence of the benzene layer on the $n = 1$ image electronic states with a dielectric constant and a first electron affinity level. An attractive electron affinity of 0.6 eV gave the best agreement between experiment and calculation. The dielectric continuum model does a moderately successful job of reproducing the experimental results for naphthalene, but fails for anthracene.

The band structure of anthracene and naphthalene differs from that of benzene. Anthracene and naphthalene have two bound conduction bands separated by a band gap.

This precludes the use of the dielectric continuum model for the theoretical calculations. The calculations instead utilize the two band NFE model for the adsorbate layer unoccupied electronic structure. The general agreement between the experimental and theoretical results indicates that the two band NFE model adequately represents the essential characteristics of the adsorbate layer unoccupied electronic structure. Theoretical calculations demonstrate that the transition from a near resonant to a non-resonant interaction between the image potential and the adsorbate EA levels produces the experimental results. The energy of the first adsorbate EA level with respect to the energy of the image potential states dictates the extent to which the image potential states and the EA levels interact. For benzene and naphthalene, the minor difference between the $n = 1$ binding energy and the first EA level results in a strong interaction. For anthracene, the conduction band minimum differs significantly from the $n = 1$ binding energy, leading to a weak interaction. The band gap in the anthracene layer excludes all electronic states degenerate with it from the layer, producing the long $n = 1$ lifetime observed for the anthracene bilayer. The inability of the dielectric continuum model to reproduce the experimental findings for anthracene can now be explained. The model cannot account for a band gap above the first electron affinity level of the layer.

The model used to describe the unoccupied electronic states of the anthracene and naphthalene layers attributes the allowed energy range in the crystal to be determined by the band structure of the layer. Energy widths comparable to those used in the theoretical calculation could also result from lifetime broadened vibronic structure in the unoccupied electronic levels of the molecule. The influence of molecular vibronic structure on image potential states have not been determined experimentally or theoretically. These effects have been observed for electronic excited states at metal surfaces, and the theoretical description of these excitations by Persson and Avouris address many of the relevant issues [98, 99].

The absence of EA levels in the TPPE spectra and their presence in the IPS spectra indicate that the cross section for exciting image potential states with substrate electrons exceeds the cross section for exciting adsorbate EA levels. A potential means of studying the influence of electronic coupling between the adsorbate and the substrate would be extending the study to more reactive metal substrates on which aromatic molecules chemisorb. The interface that would result from chemisorption to a low workfunction metal such as aluminium would more closely resemble the working interfaces in organic LEDs and provide a system with which to study the influence of strong electronic interaction on

charge injection into molecular electronic materials.

These experimental and theoretical findings lead to two conjectures regarding electron injection at organic semiconductor-metal interfaces. Firstly, the likelihood of photoinjection increases when the organic semiconductor EA levels couple strongly to the image potential. For anthracene, no electron injection occurs as only image potential states weakly coupled to the adsorbate conduction bands appear in the kinetic energy spectra. For naphthalene, strong coupling of the first conduction band to the image potential results in the excitation of electrons from the metal into the organic semiconductor. Secondly, the present account has demonstrated the inability of the dielectric continuum model to explain electron photoinjection into thin films of naphthalene and anthracene. Whether similar limitations exist for continuum model descriptions of thermal electron injection has yet to be determined [13–16].

Chapter 5

Electron Localization at Aromatic-Metal Interfaces

With angle resolve TPPE, the electronic band structure parallel to the interface can be monitored. For electrons in vacuum or periodic solids, the wavefunction will be periodic, with the periodicity being determined by the wavevector, k. This wavevector represents the principle quantum number for electrons in periodic solids. The electronic dispersion, or the wavevector dependence of the electronic energy, characterizes the band structure of periodic solids. In angle resolved photoemission, the relation between the energy and the parallel component of the wavevector, $k_{||}$, can be measured. This represents the parallel dispersion of the electronic band structure. A schematic representation of angle resolved TPPE appears in Figure 2.5.

The photoemission process conserves $k_{||}$, but not the perpendicular wavevector, $k_{\perp}$. During photoemission, the electron must cross a surface. In the direction normal to the surface, $k_{\perp}$ provides a good quantum number for the initial and final states, but does not define the electronic wavefunction at the aperiodic surface. For this reason, photoemission does not conserve $k_{\perp}$. In the direction parallel to the surface, the potential retains its periodicity, with the amplitude of the potential decreasing to zero in the vacuum. For this reason, the photoemission process conserves $k_{||}$. The lack of $k_{\perp}$ conservation limits the ability of photoemission to measure the normal dispersion of the electronic band structure. This does not limit the study of surface electronic states, which have no dispersion perpendicular to the surface.

By measuring the photoelectron kinetic energy, E_{kin}, as a function of the angle, θ, between the surface normal and the detector, the two dimensional band structure parallel to the surface can be measured. The angle dependence of the kinetic energy provides a direct measure of $k_{||}$,

$$k_{||} = \sqrt{\frac{2m_e E_{kin}}{\hbar^2}} \sin\theta, \tag{5.1}$$

where m_e represent the free electron mass. Nearly free electronic states possess parabolic dispersions given by

$$E(k_{||}) = E_{||} + E_0, \tag{5.2}$$

where $E_{||} = \hbar^2 k_{||}^2 / 2m^*$, E_0 is the kinetic energy at zero degrees, and the effective mass, m^*, is a paramaterized measurement of the curvature of the dispersion. The weak interaction of nearly free electrons with the layer parallel to the interface results in two dimensionally delocalized electronic states characterized by an m^*/m_e ratio on the order of unity. For two dimensional systems with translational symmetry, the quantum number $k_{||}$ defines the dispersion of the corresponding band structure. For systems without translational symmetry, the quantum number $k_{||}$ no longer characterizes the electronic state, and has no clear relation to the energy. Non-dispersive electronic states correspond to states with $k_{||}$ independent energies. A lack of dispersion represents a necessary, but insufficient, criteria for electron localization. For a non-dispersive electronic state to be localized, the electron must be trapped in a local potential energy minimum.

The spatial extent of the $n = 1$ image potential state parallel to a metal surface has proven to be sensitive to the structure and chemical identity of the adsorbate layer. For materials with large electron mean free paths, such as Xe and neopentane, image potential state electrons do not localize parallel to the interface [100–102]. For strong electron scatterers, such as n-heptane and benzene, image potential states form localized electronic states parallel to the interface [28, 66]. The presence of defects eliminates the two dimensional translational symmetry and generates an aperiodic potential. The aperiodicity of the system can result in image potential states spatially localized both parallel and perpendicular to the surface, as seen for the benzene/Ag(111) interface [28]. For benzene, localization occurs at the static defects in the layer within the $\approx$ 100 fs time duration of the excitation pulse. In addition to static inhomogeneity in the potential, the image potential electron can

dynamically induce a lattice distortion which results in a time dependent inhomogeneity in the potential. For such a case, electron localization becomes a dynamic process as observed at the anthracene/Ag(111) interface.

The angle resolved TPPE results for image potential states at the benzene/Ag(111), naphthalene/Ag(111), and anthracene/Ag(111) interfaces will be described. After describing the experimental findings, the theoretical model used to explain dynamic localization will be introduced. This model will be applied to the $n = 1$ localization dynamics measured at the anthracene/Ag(111) interface.

5.1 Image Potential State Dispersions

The $n = 1$ experimental dispersions for one to three layers of benzene appear in Figure 5.1. The effective mass of $n = 1$ decreases upon adsorption of benzene. A major cause for the change in the effective mass is the change in workfunction. The decrease in workfunction lessens the image state interaction with the substrate conduction band (see Figure 4.1), which results in the decreased effective mass [103]. This effect cannot, however, account for a monolayer m^*/m_e of less than 1 or the increase in the effective mass for the transitions from monolayer to bilayer benzene and bilayer to trilayer benzene. The $n = 1$ effective mass does not change for coverage above a trilayer of benzene. These subtle variations in effective mass most likely result from the $n = 1$ image state interaction with the adsorbate EA level. The monolayer $n = 1$ effective mass of 0.9 resembles the 1.1 value measured by Velic et al., but the bilayer value of 1.0 differs significantly from the $n = 1$ effective mass of 1.9 found for a bilayer of benzene adsorbed on Cu(111) [74].

The $n = 1$ experimental dispersions for naphthalene and anthracene appear in Figures 5.2 and 5.3. For zero time delay between the pump and probe pulses, all excitations for both naphthalene and anthracene exhibit nearly free electron m^*. For naphthalene, the $n = 1$ m^* increases upon the adsorption of the second layer, while the $n = 1$ binding energy decreases. This indicates that the interaction of the perpendicular and parallel components of the $n = 1$ wavefunction with the adsorbate layer need not exhibit the same layer dependent variation. The smaller deviation of the m^* from m_e for anthracene indicates a weaker interaction between $n = 1$ and the layer, fully consistent with the observed lifetimes and binding energies.

For benzene coverage in excess of a bilayer, a new excited electronic state appears

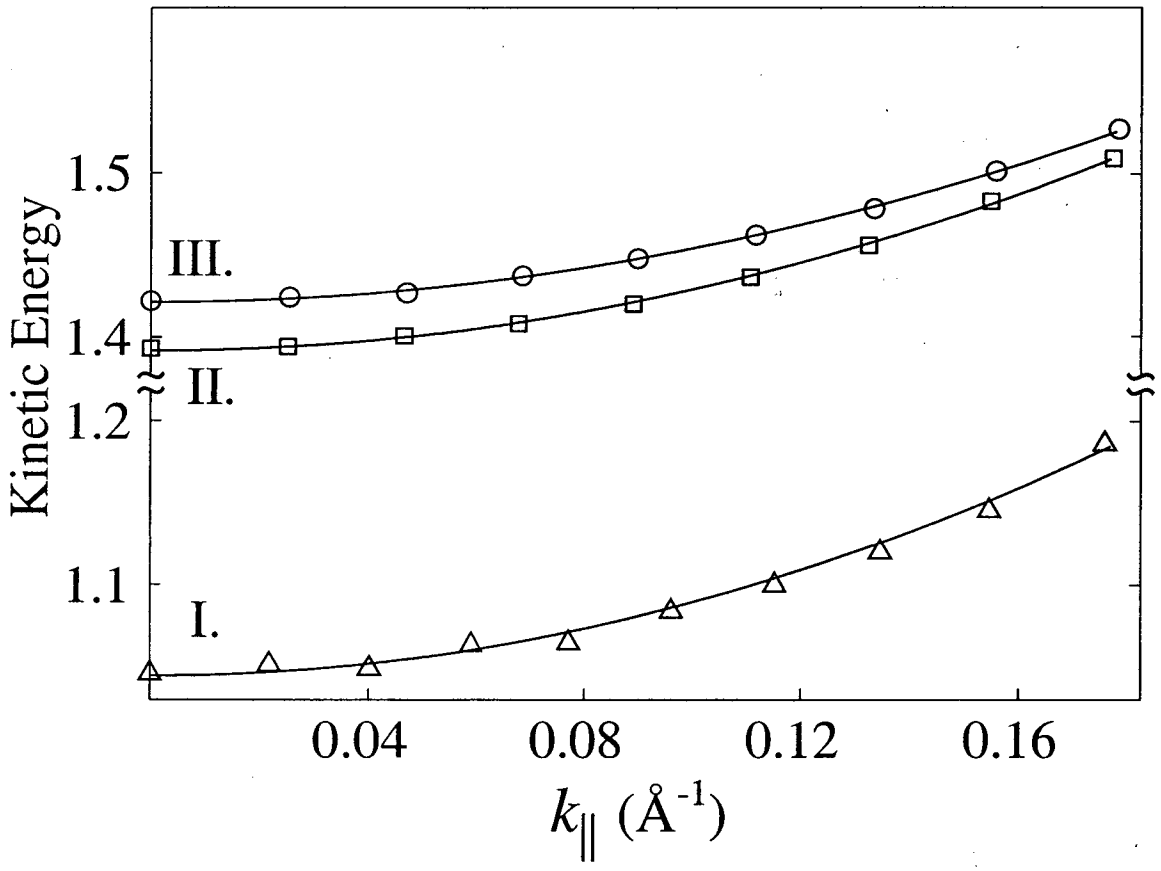

Figure 5.1:

The dispersion of the $n = 1$ image state for a monolayer I., bilayer II., and trilayer III. of benzene adsorbed on Ag(111). The measured m^*/m_e are 0.9 ± 0.1, 1.0 ± 0.1, and 1.2 ± 0.2 for a monolayer, bilayer, and trilayer, respectively. The $n = 1$ image state has an effective mass of 1.3 for the clean Ag(111) surface.

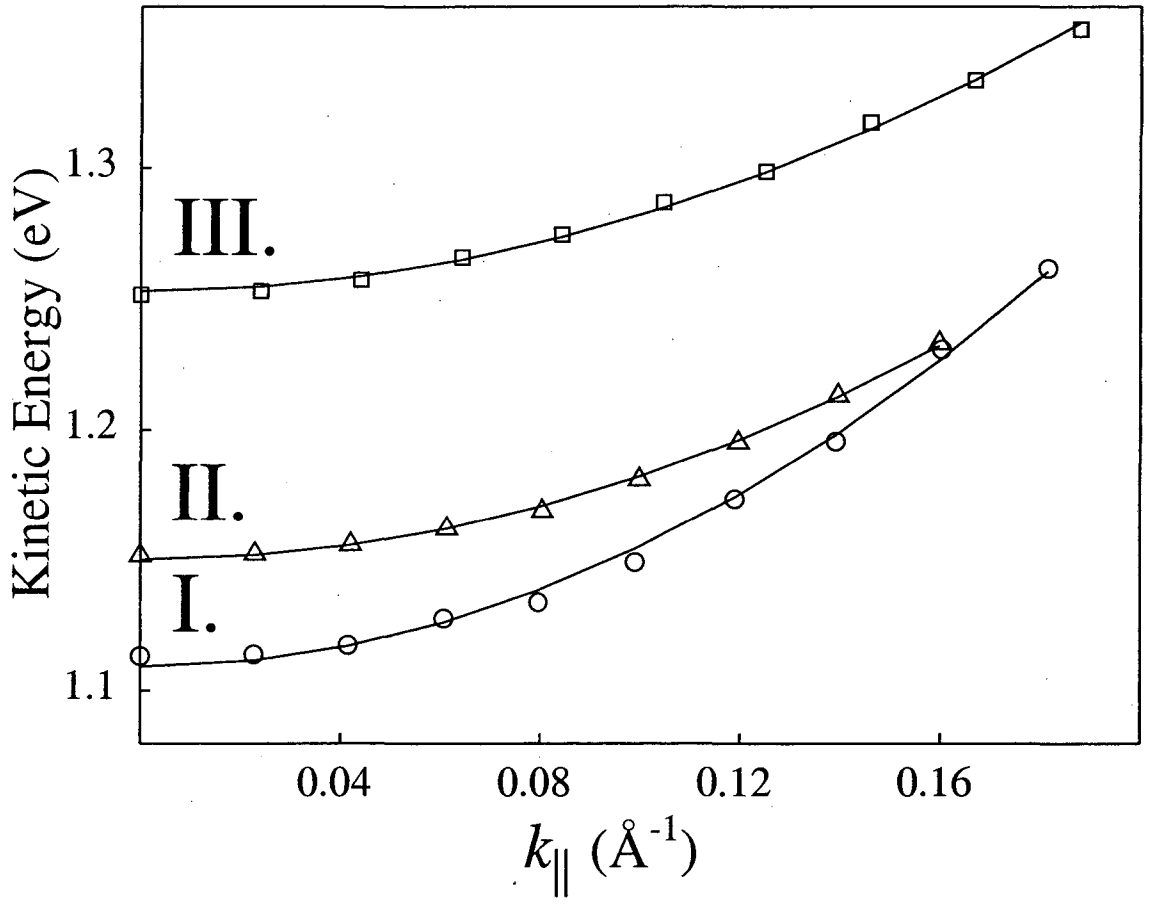

Figure 5.2: The dispersion of the $n = 1$ image potential states for naphthalene. Dispersions labeled I., II., and III. refer to monolayer, bilayer, and trilayer coverages. The measured $n = 1$ m^*/m_e are 0.8 ± 0.1, 1.3 ± 0.2, and 1.2 ± 0.2 for a mono-, bi-, and a trilayer of naphthalene. The measured $n = 2$ m^*/m_e are 1.2 ± 0.2 and 1.0 ± 0.1 for mono- and bilayer naphthalene.

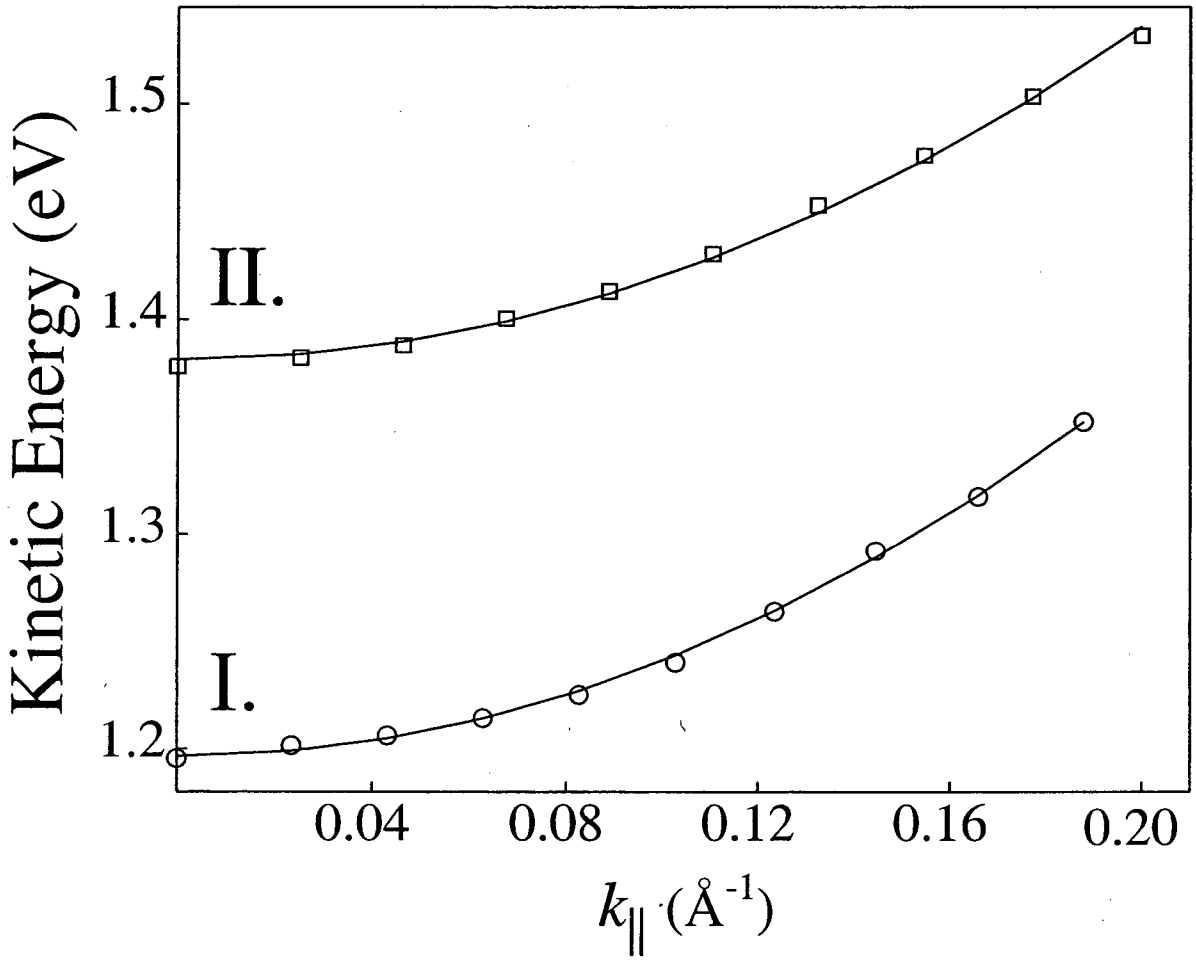

Figure 5.3: The dispersion of the $n = 1$ image potential states for anthracene (b). Dispersions labeled I. and II. refer to monolayer and bilayer coverages. The measured $n = 1$ m^*/m_e are 0.9 ± 0.1 and 1.0 ± 0.1 for a monolayer and a bilayer of anthracene. The measured $n = 2$ m^*/m_e is 1.0 ± 0.1 for monolayer anthracene.

in the kinetic energy spectra, Figure 5.4. The new excitation possesses an momentum independent photoelectron kinetic energy, indicating that the state is spatially localized parallel to the interface. The appearance of the localized state in the kinetic energy spectra coincides with the delocalized $n = 1$ image potential state. The lack of a measurable rise time in the localized state population dynamics indicates that the state localizes at static defects in the potential. Two criteria support the conclusion that the peak results from structural disorder induced localization of the $n = 1$ image potential state. Foremost, the excitation slowly shrinks in magnitude as the layer anneals. This annealing occurs at a temperature too low for benzene desorption, so the localized peak would appear to diminish as the layer disorder diminishes. Secondly, the lower binding energy of the localized $n = 1$ image state, when compared to the dispersive $n = 1$ image state, is consistent with the effect of disorder induced quantum confinement parallel to the interface. A similar increase in energy was found for image potential states localized on Ag(111) islands adsorbed on a Pd(111) surface [104].

Electron localization for a bilayer of anthracene on Ag(111) occurs dynamically. For zero time delay between the pump and probe pulses, the $n = 1$ image potential state has a nearly free electron dispersion as shown in Figure 5.5(a). After a delay time of 1 ps, the dispersive $n = 1$ states at higher $E_{||}$ have decayed and a new series of non-dispersive peaks appear in the kinetic energy spectra (see Figure 5.5(b)). The dynamics of this localization process can be seen more clearly in Figure 5.6, which depicts the dynamic evolution of the kinetic energy spectra taken at 20°. A series of three peaks appear in the spectrum with binding energies of -0.93 eV, -0.71 eV, and -0.55 eV. The least bound localized state has binding energy 15 meV larger than the -0.54 eV energy of the delocalized $n = 1$ at $E_{||} = 0$. Before discussing the experimental finding for the anthracene bilayer,the theoretical description of electron localization dynamics will be presented.

5.2 Theory of Dynamic Image Potential State Localization

The dynamic localization of image potential states for a bilayer of n-heptane adsorbed on a Ag(111) surface have been explained with a theoretical model based on quantum mechanical representation of Marcus electron transfer theory that accounts for both high frequency vibrational modes and all orders in the electronic coupling [105–111]. Within this theoretical framework, the electron localizes in a self induced lattice distortion, with the

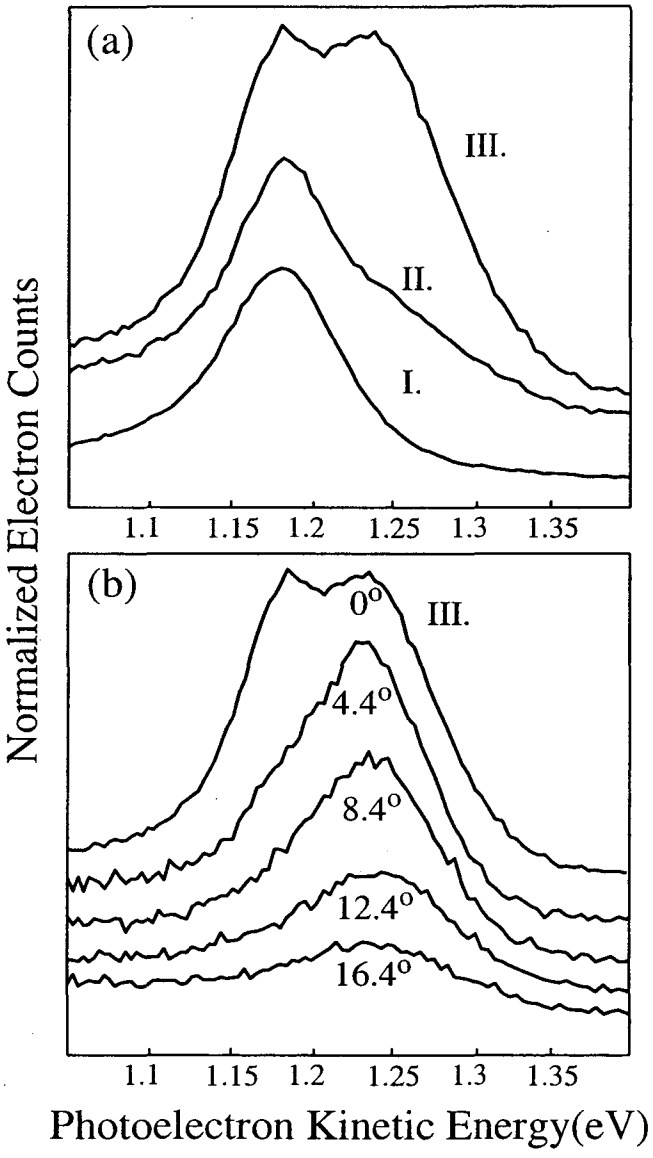

Figure 5.4: The development of the localized $n = 1$ image state as a function of coverage appears in (a) with I. corresponding to a bilayer, II. 3.5 layers, and III. 4 layers of benzene. The two peaks in III., from right to left, correspond to the localized state and the delocalized $n = 1$ image state. The photoelectron kinetic energy spectra of 4 layers of benzene adsorbed on Ag(111) as a function of angle appear in (b). The delay time between the excitation and probe pulses is 70 fs for the 0° spectra and 170 fs for all other angles. The longer delay time allows the localized state, which possesses a slightly longer lifetime, to dominate the kinetic energy spectra. The invariance of the photoelectron kinetic energy of the primary peak in (b) confirms the state to be localized parallel to the interface.

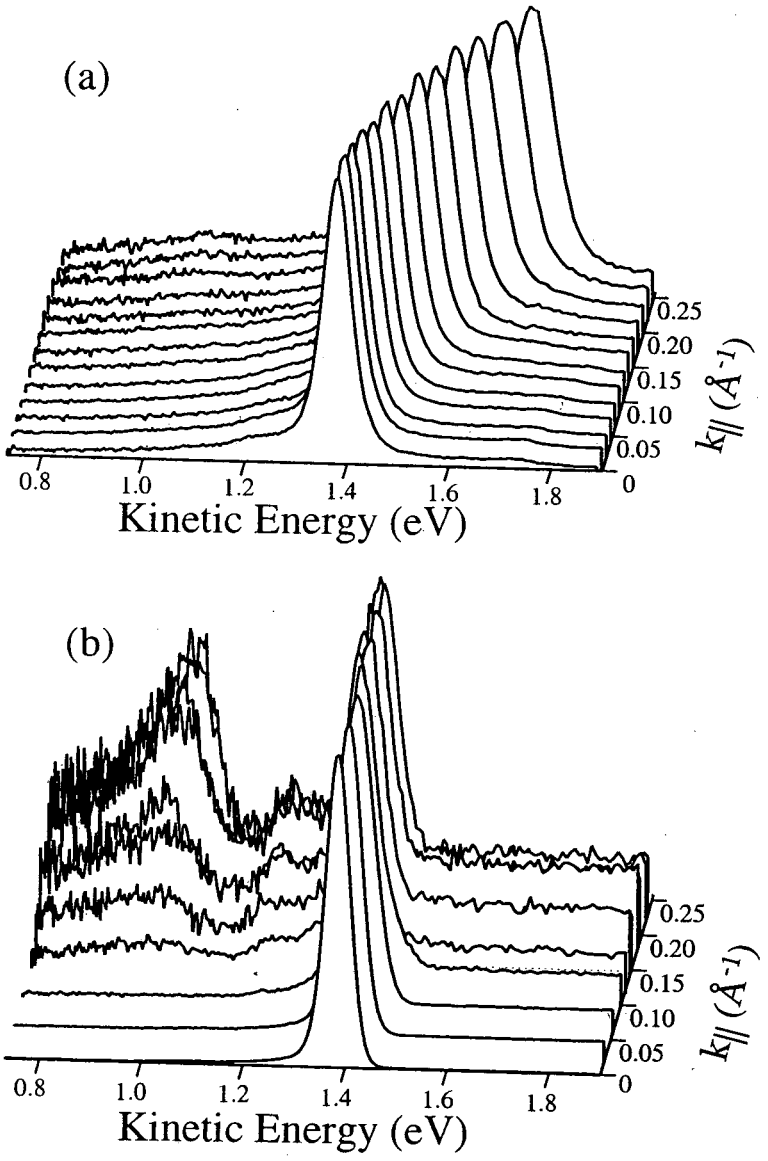

Figure 5.5: Femtosecond angle resolved kinetic energy spectra for a bilayer of anthracene adsorbed on Ag(111). (a) Plot of energy versus $k_{||}$ for zero pump-probe time delay. The dispersive $n = 1$ dominates the spectra. (b) Plot of the energy versus $k_{||}$ for a one picosecond pump-probe delay. Non-dispersive features dominate the spectra, with three peaks clearly present at higher $k_{||}$. All spectra are normalized to the highest intensity peak in each spectrum. The absolute amplitude of the highest energy non-dispersive feature decreases with increasing $k_{||}$, while the other two non-dispersive features have amplitudes that increase with increasing $k_{||}$.

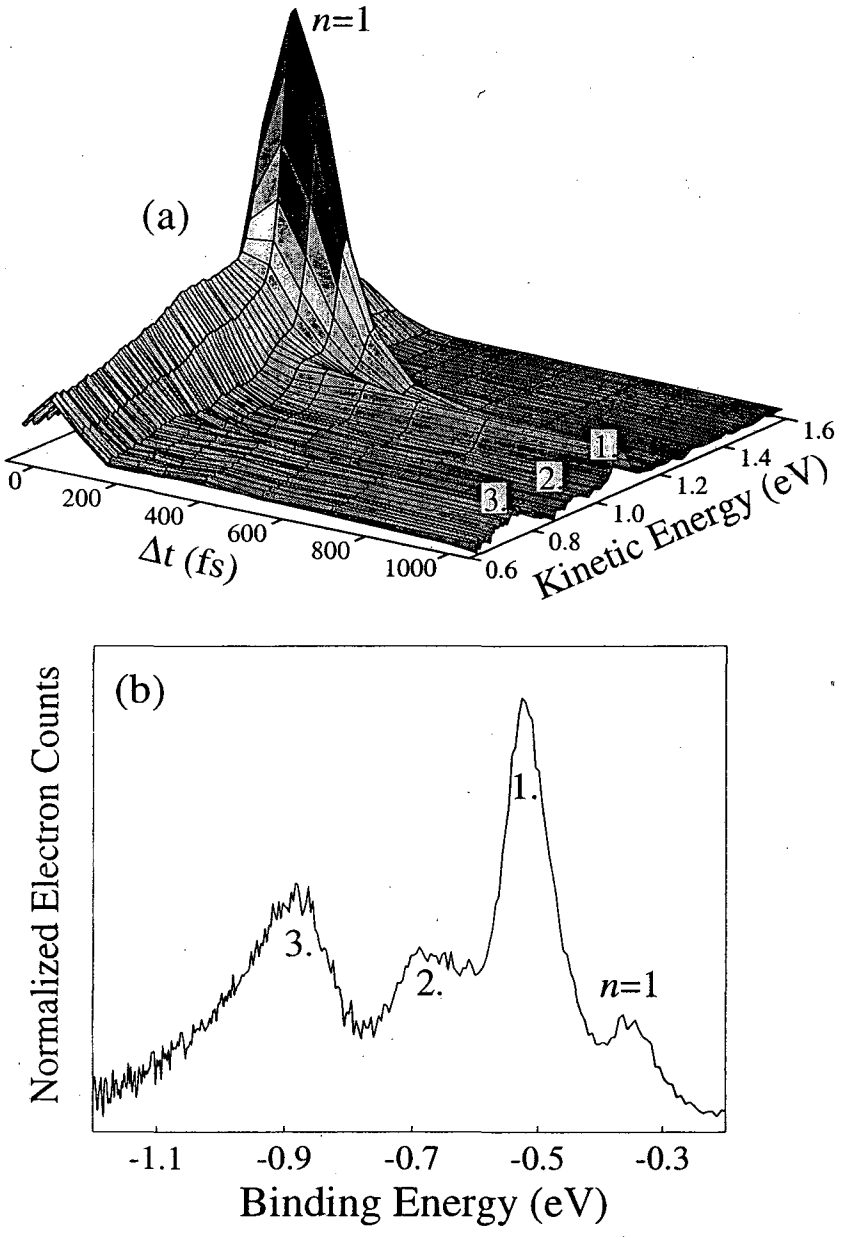

Figure 5.6: (a) Photoelectron kinetic energy spectra as a function of pump-probe time delay at 20° for a bilayer of anthracene. The highest energy peak corresponds to the delocalized $n = 1$, which decays with a time constant of 50 fs. The three features to lower energy correspond to a vibronic progression in the localized electronic state. The localized states decay with a time constant of 1.1 ps. (b) Photoelectron kinetic energy spectrum at a time delay of 366 fs for a bilayer of anthracene at 20°. Four peaks can clearly be seen, the three lower kinetic energy peaks all being non-dispersive.

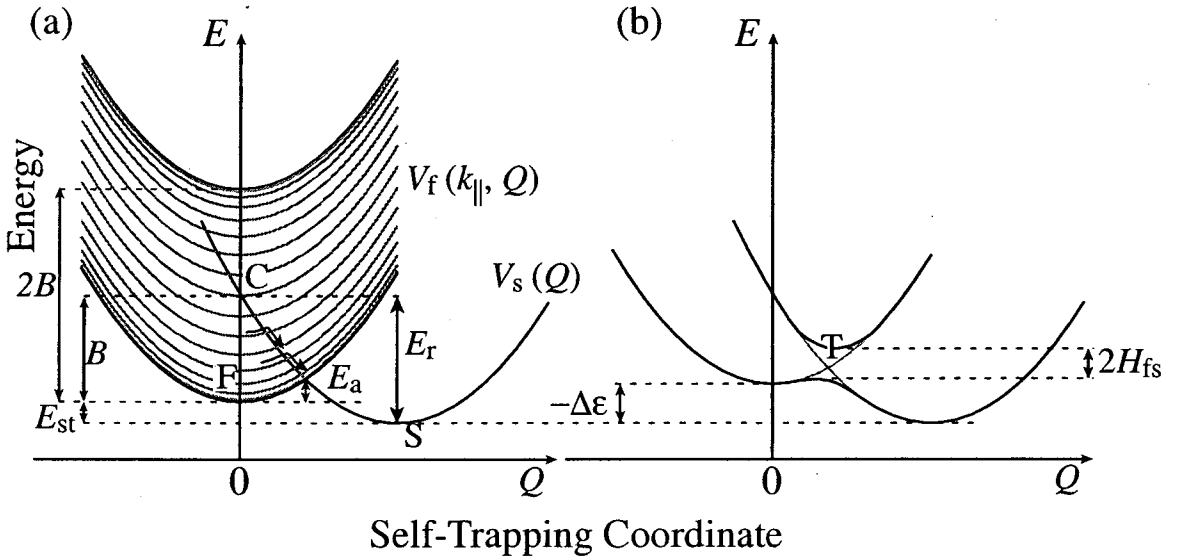

Figure 5.7: (a) Schematic representation of electron localization. Curves $V_f(k_{||}, Q)$ and $V_s(Q)$ correspond to the delocalized and localized states, respectively. Each $V_f(k_{||}, Q)$ corresponds to a different $k_{||}$ state with a band energy of $E_{||}$. For definitions of the other parameters, see the text. (b) A schematic representation of the influence of electronic state coupling (H_{fs}) in electron localization. For large H_{fs}, the electron adiabatically follows the lowest energy curve, while for small H_{fs} only a fraction of the electrons that reach the transition state transfer from the delocalized donor to the localized acceptor state.

electron dressed by the lattice distortion called a small polaron [112].

The energetics that govern electron localization can be understood within a simple framework. The spatial extent of an electron in a crystal reflects the energetic competition between delocalizing and localizing tendencies. Delocalization reduces the curvature of the electronic wavefunction, leading to a reduction in the electron kinetic energy (Figure 5.7(a), point F). To localize an electron at a single lattice site without allowing the lattice to distort requires energy (Figure 5.7(a), point C). Due to the position momentum uncertainty relation, the momentum space wavefunction for an electron localized to a single lattice site will correspond to an electron wavepacket constructed from all the Bloch waves within the band. The average energy of such a wavepacket will be the band midpoint energy. The energy difference between the band minimum and the band midpoint represents the energetic cost of electron localization, termed the localization energy, E_{loc}, and equals half of the band width. The driving force behind electron localization is the energetic benefit of localizing in a self-induced potential energy minimum, termed the reorganization energy,

E_r (Figure 5.7(a), point S). Due to the self-induced nature of the localizing potential, the electron can be described as self-trapped. The electron will localize when E_r exceeds E_{loc}, with the difference referred to as the self-trapping energy, E_{st}:

$$E_{st} = E_r - E_{loc} > 0. \tag{5.3}$$

The self-trapping energy provides the thermodynamic driving force for electron localization, but does not provide an explanation for the dynamics of electron localization. The dynamics of small polaron formation can be quantitatively modeled with electron transfer theory. Electron transfer theory provides a flexible and sophisticated description of localization. Figure 5.7 demonstrates pictorially many of the important aspects of electron transfer theory and will facilitate the following discussion. As in transition state theory, the electron transfer rate depends critically on the probability of reaching the transition state between the two electronic potential energy surfaces. For polaron formation that must overcome an energy barrier, the electron self-trapping rate, k_{st}, depends exponentially on the barrier height, E_a, in Figure 5.7(a):

$$k_{st} \propto e^{-\frac{E_a}{k_B T}}. \tag{5.4}$$

Within the harmonic approximation, E_a depends quadratically on the reaction exothermicity $\Delta\varepsilon$,

$$k_{st} = \kappa e^{-\frac{(\Delta\varepsilon + E_r)^2}{4E_r k_B T}}. \tag{5.5}$$

The exponential prefactor κ will be discussed shortly. The $E_{||}$ dependence of the exothermicity, $\Delta\varepsilon = -E_{||} - E_{st}$, causes the $k_{||}$ dependence of the delocalized states' lifetimes. For the localization of the $E_{||} = 0$ image potential state, the delocalized electron must cross an energy barrier to localize, resulting in the slowest rate of small polaron formation. As $E_{||}$ increases, the size of the barrier decreases and k_{st} increases until $-\Delta\varepsilon = E_r$, where no energetic barrier impedes electron localization (Figure 5.7(a), point C). Further increase in $E_{||}$ results in a decrease in k_{st}. In short, the localization rate will first increase with an increase in $-\Delta\varepsilon$ until it reaches a maximum and then proceeds to decrease in the Marcus inverted region.

Once the system reaches the transition state (Figure 5.7(b), point T), the electron localization rate k_{st} depends on H_{fs}, the Hamiltonian matrix element between the delocal-

ized and the localized electronic states. The influence of the coupling strength enters the rate equation via the exponential prefactor, κ. For a non-adiabatic interaction, characterized by $H_{fs} \ll k_B T$, the nuclear configuration can reach the transition state without having the electron transfer from the reactant potential energy surface to the product potential energy surface. For weakly coupled electronic states, the non-adiabatic expression for κ must be used for k_{st}:

$$\kappa = \sqrt{\frac{\pi}{\hbar^2 E_r k_B T}}\, H_{fs}^2. \tag{5.6}$$

Within the non-adiabatic limit, the exponential prefactor depends quadratically on the electronic coupling strength. For an adiabatic electronic interaction, characterized by $H_{fs} \gg k_B T$, the electron always resides on the lowest potential energy surface for a given nuclear configuration. For strongly coupled electronic states, the adiabatic expression for κ must be used for k_{st}:

$$\kappa = \omega_0 / 2\pi. \tag{5.7}$$

Within the adiabatic limit, the localization rate depends on the attempt rate determined by the characteristic frequency, ω_0, of the harmonic potential. Only recently have expressions been derived that accurately interpolate between non-adiabatic and adiabatic limits [110,111,113]. These new quantum mechanical expressions have been derived with path integral techniques that involve all orders in the coupling. Their value is two-fold; an a priori knowledge of the coupling strength is no longer necessary, and intermediate coupling strengths can be accurately modeled as well.

The preceeding description of electron transfer theory applies when the relevant nuclear motions behave classically. Within the harmonic approximation, a characteristic frequency, ω, defines all nuclear motions. The motions that follow classical mechanics can be classified as those for which $\hbar\omega < k_B T$. For low temperatures and high frequencies, nuclear tunneling determines the rate of electron transfer due to the prohibitively large excitation energies. A schematic diagram of the influence of high frequency vibrations in electron transfer reactions appears in Figure 5.8. Small polaron formation in a molecular crystal can involve both inter- and intramolecular vibrations. The low frequency intermolecular phonons can be treated classically when T excedes the Debye temperature of the lattice, while the high frequency molecular vibrations cannot be accessed thermally and

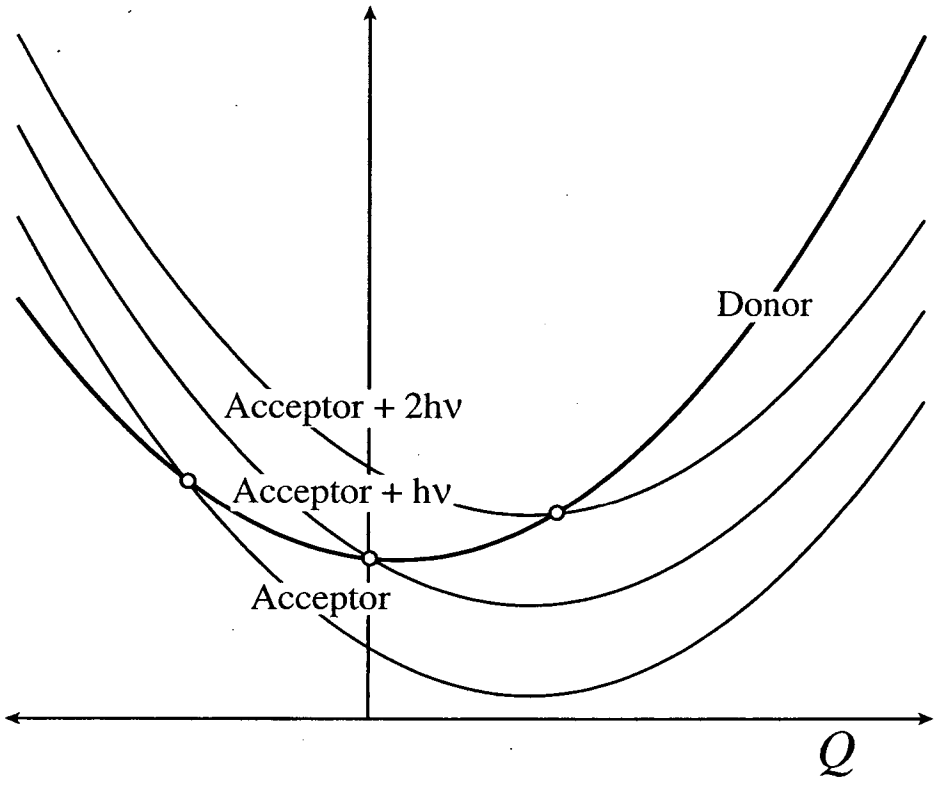

Figure 5.8: Schematic potential energy surfaces for nuclear motion along the self-trapping coordinate. The electron donor resides in the ground vibrational state of a high frequency vibration, while the ground and first two vibrational excited states of the acceptor appear. Electron transfer can occur from the vibrational ground state of the donor to a vibrationally excited acceptor state. While the electron transfer reaction from the ground state of the donor to the ground state of the acceptor must cross an energy barrier, the electron transfer reaction to the first vibrational excited state has no barrier.

require a quantum mechanical treatment. The nuclear tunneling rate depends critically on the Franck-Condon factor, the square of the overlap integral between the vibrational wavefunctions of the delocalized state and the localized state. For harmonic potentials, the Franck-Condon factor can be determined analytically to get a rate expression that accounts for both thermally activated barrier crossing and quantum mechanical nuclear tunneling. The non-adiabatic expression for k_{st} with one quantum mechanical vibrational mode, ω_q, demonstrates many of the important manifestations of nuclear tunneling in electron transfer [108,109]. When $\hbar\omega_q \gg k_B T$,

$$k_{st} = \sqrt{\frac{\pi}{\hbar^2 E_{rc} k_B T}}\, H_{fs}^2 \sum_{m=0}^{\infty} \left[e^{-\frac{E_{rq}}{\hbar\omega_q}} \frac{1}{m!} \left(\frac{E_{rq}}{\hbar\omega_q} \right)^m \right] e^{-\frac{(\Delta\varepsilon + E_{rc} + m\hbar\omega_q)^2}{4E_{rc}k_B T}}, \tag{5.8}$$

where m represents the vibrational quanta in the localized state and E_{rc} and E_{rq} correspond to the classical and quantum mechanical reorganization energies. The term in square brackets corresponds to the Franck-Condon factor, $|\langle 0|m\rangle|^2$. The preceeding expression assumes the donor state to be in the ground state of the high frequency mode.

As seen for the classical expression for the electron transfer rate, much of the significant physics lies in the final exponential term. In the classical description of electron transfer, the rate reaches a maximum when $-\Delta\varepsilon = E_r$. The exponential factor in the rate equation that contains a single quantum mode reaches a maximum whenever $-\Delta\varepsilon = E_{rc} + m\hbar\omega_q$. Thus, the exponential factor has an infinite number of maxima. The Franck-Condon factor also reaches a maxium, which occurs when $m\hbar\omega_q = E_{rq}$. The overall rate increases as the magnitude of $\Delta\varepsilon$ increases until the rate reaches a maximum at roughly $-\Delta\varepsilon = E_{rq} + E_{rc}$. Further increases in the magnitude of $\Delta\varepsilon$ result in a decrease in the rate, though the drop does not occur as quickly as it does in the classical limit, and the dependence of k_{st} on $\Delta\varepsilon$ is no longer symmetric about the maximum. The presence of oscillations in k_{st} as a function of $-\Delta\varepsilon$ also indicates the importance of high frequency mode reorganization during small polaron formation. The magnitude of the oscillations increase as the fraction $\hbar\omega_q/4E_{rc}k_B T$ increases, meaning they should become more prominent as the temperature decreases.

While the limiting cases of adiabatic and non-adiabatic electron transfer rates do describe a wide range of reactions, a theoretical description that accurately treats all electron coupling strengths represents a clear improvement. The theory describing the electron localization dynamics at the n-heptane/Ag(111) interface utilized the theory of

Stuchebrukhov and Song [113]. An alternative theory derived by Rips and Jortner also treats all electronic coupling strengths [110]. The comparative ease of implementation, makes the Rips and Jortner electron transfer theory an appealing alternative to the theory of Stuchebrukhov and Song. Bixon and Jortner extended the work of Rips and Jortner to account for high frequency vibrational modes [111]. This formulation of electron transfer theory provides a powerful tool with which to analyze the dynamics of electron localization.

In the Rips and Jortner formulation, the electron transfer rate depends upon an adiabaticity parameter [110],

$$\mathcal{H} = \frac{4\pi H_{fs}^2 \tau_l}{\hbar E_{rc}}. \tag{5.9}$$

where τ_l reprsents the longitudinal dielectric relaxation time. This electron transfer rate can be expressed in terms of the non-adiabatic rate, k_{na}, and $\mathcal{H}$:

$$k_{st} = \frac{k_{na}}{\mathcal{H}+1}. \tag{5.10}$$

The non-adiabatic electron transfer rate, k_{na}, appears in Equations 5.5 and 5.6. For small H_{fs}^2, $\mathcal{H} \ll 1$, and the rate will reduce to the non-adiabatic rate. For large H_{fs}^2, $\mathcal{H} \gg 1$, and the rate will be

$$k_{st} = \sqrt{\frac{E_r}{16\pi k_B T \tau_l^2}}\, e^{-\frac{(\Delta\epsilon + E_r)^2}{4E_r k_B T}}. \tag{5.11}$$

For the case of a barrierless electron transfer, the adiabatic rate will be limited by the dynamics of the lattice response, $1/\tau_l$.

Bixon and Jortner extended this theoretical approach to include high frequency quantum modes [111]. Now the adiabaticity parameter will depend on the Franck-Condon factor,

$$\mathcal{H}^{(0m)} = \mathcal{H}|\langle 0|m\rangle|^2. \tag{5.12}$$

With the inclusion of a quantum mechanical vibration, the adiabaticity of the reaction must be determined for each $n \leftarrow 0$ vibronic transition. The total rate will be a sum over all vibronic transitions,

$$k_{st} = \sum_{m=0}^{\infty} k^{(0m)} \tag{5.13}$$

$$k^{(0m)} = \frac{k_{na}^{0m}}{1+\mathcal{H}^{(0m)}}, \tag{5.14}$$

where,

$$k_{na}^{0m} = \sqrt{\frac{\pi}{\hbar^2 E_r k_B T}}\, H_{fs}^2 |\langle 0|m\rangle|^2\, e^{-\frac{(\Delta\epsilon + E_r + m\hbar\omega_q)^2}{4E_r k_B T}}. \tag{5.15}$$

For those modes with $\mathcal{H}^{(0m)} \ll 1$, k_{na}^{0m} will reduce to Equation 5.8 without the summation over m. For those modes with $\mathcal{H}^{(0m)} \gg 1$, k_{na}^{0m} will become Equation 5.11, with $\Delta\varepsilon$ replaced by $\Delta\varepsilon + m\hbar\omega_q$.

This formulation of the electron transfer rate assumes that the donor will be in the vibrational ground state, and that only one quantum mechanical vibration contributes to the rate. As will be discussed in Section 5.3.2, the fit of the experimental data requires two high frequency modes. Multiple quantum modes can be accounted for without significantly increasing the complexity of the rate expressions. Multiple quantum modes require the modification of the adiabaticity parameter and the non-adiabatic rate constant, as well as the summation over a new set of vibrational levels. For two quantum modes,

$$\mathcal{H}^{(0m,0n)} = \mathcal{H}|\langle 0|m\rangle|^2|\langle 0|n\rangle|^2. \tag{5.16}$$

The rate will now be summed over both m and n, with

$$k_{st} = \sum_{m=0}^{\infty}\sum_{n=0}^{\infty} k^{(0m,0n)} \tag{5.17}$$

$$k^{(0m,0n)} = \frac{k_{na}^{0m,0n}}{1+\mathcal{H}^{(0m,0n)}}, \tag{5.18}$$

where,

$$k_{na}^{0m,0n} = \sqrt{\frac{\pi}{\hbar^2 E_r k_B T}}\, H_{fs}^2 |\langle 0|m\rangle|^2 |\langle 0|n\rangle|^2\, e^{-\frac{(\Delta\varepsilon + E_r + m\hbar\omega_m + n\hbar\omega_n)^2}{4E_r k_B T}}. \tag{5.19}$$

5.3 Application of Electron Transfer Theory to Localization Dynamics

Electron localization dynamics at the n-heptane/Ag(111) interface have been explained with the electron transfer theory just described in Section 5.2. Before applying the theory to the results at the anthracene/Ag(111) interface, an brief description of the n-heptane/Ag(111) results will provide context and address some of the limitations of the theory.

5.3.1 Electron Localization at the n-Heptane/Ag(111) interface

Electron localization occurs dynamically for n-heptane adsorbed on Ag(111) [66]. For zero time delay, the $n = 1$ image potential state possesses a nearly free electron dispersion, as expected for a crystalline adsorbate layer. A new, non-dispersive feature appears

for a 1670 fs time delay, while the majority of the signal from the dispersive feature has decayed. This non-dispersive feature corresponds to a two dimensionally localized image potential state on the n-heptane surface. The dynamics of both the delocalized and localized states have been studied as a function of $k_{||}$. The localized state rise time of 360 ± 140 fs and decay time of 1600 ± 200 fs do not vary as a function of $k_{||}$, while the delocalized state rise and decay times exhibit significant parallel momentum dependence. The rise time for the non-dispersive feature reflects the dynamic nature of localization, while the decay time reflects the rate at which the localized state tunnels through the n-heptane layer [65].

The analysis assumes that the $k_{||}$ dependent decay rate of a delocalized image potential state, $1/\tau_d(k_{||})$, can be represented as a sum of the decay rate to the metal, $1/\tau_t$, and the decay rate to the localized state, $1/\tau_{st}(k_{||})$:

$$\frac{1}{\tau_d(k_{||})} = \frac{1}{\tau_t} + \frac{1}{\tau_{st}(k_{||})} \tag{5.20}$$

$$k_{st} = \frac{1}{\tau_{st}}. \tag{5.21}$$

The decay time for the localized state provides τ_t. Subtraction of $1/\tau_t$ from each delocalized state decay rate gives the $k_{||}$ dependent localization rate. This assumes that delocalized states only have two decay channels; they can tunnel through the alkane layer and decay in the substrate or they can localize. This assumption should be viewed with caution due to the signicant rate of intraband relaxation in systems that do not localize electrons [48,114]. The validity of this assumption could be verified by determining both the initial population as a function of $k_{||}$ in the two dimensional $n = 1$ image potential state band and the $k_{||}$ dependent decay rate. The $k_{||}$ dependent decay rate for the delocalized states, in conjuction with the the $k_{||}$ dependent initial population, will give you the measured rise time of the localized state, if localization dominates.

An alternative approach to the problem would be greatly limiting the range of $k_{||}$ initially populated. The peculiarities of the Ag(111) projected bulk band structure make this difficult. At the Ag(111) surface the valence band crosses the Fermi level at $k_{||} \approx 0.2$ Å^{-1}, as shown in Figure 2.2. The valence band has a smaller m^* than the image potential state, so as $k_{||}$ increases the energy spacing between the valence band and the $n = 1$ band decreases. In the light adsorption process, $k_{||}$ should be conserved. This means that the lowest energy transition from the valence band to the $n = 1$ image potential state occurs at $k_{||} \approx 0.2$ Å^{-1}. At this photon energy, states with lower $k_{||}$ must be accessed via a phonon

assisted transition, where the phonon supplies the necessary parallel momentum. These phonon assisted transitions will result in the population of all $k_{||}$ states up to 0.2 $Å^{-1}$. Since significant population at lower $k_{||}$ can occur with no appreciable rise time at the Ag(111) surface, these phonon assisted transitions do appear to be happening. This makes controlling the initial distribution in the $n = 1$ band unfeasible at the Ag(111) surface. At the Ag(100) surface, the valence band crosses the Fermi level at $k_{||} = 0$. By varying the photon energy, the range of $k_{||}$ populated can be changed from just populating the image potential state band at very low $k_{||}$ to exciting the entire band. The rise time of the localized state as a function of the initial distribution in the delocalized state band could be monitored. For the excitation of a narrow range of $k_{||}$, the rise time of the localized state should equal the decay time of the delocalized state, if localization provides the primary decay channel.

The weak temperature dependence of the localization rate provides another defining feature of electron self-trapping at the n-heptane/Ag(111) interface. This weak temperature dependence indicates that nuclear tunneling, in addition to thermally activated barrier crossing, occurs during electron localization. The reorganization of high frequency vibrations, $\hbar\omega_q \gg k_B T$, requires nuclear tunneling. How the reorganization of quantum mechanical vibrations enters the theory of electron transfer reactions has been discussed in Section 5.2. The parameters used to fit the localization dynamics for n-heptane indicate that the reorganization of a 750 cm^{-1} vibration dominates the self-trapping process. The maximum in the localization rate occurs for delocalized electronic states that have enough energy to excite two quanta of vibration in this mode. The maximum in the electron transfer rate occurs because of a maximum in the Franck-Condon factor for the $|\langle 0|2\rangle|^2$ transistion.

5.3.2 Electron Localization at the Anthracene/Ag(111) Interface

The presence of three localized states at larger parallel momentum distinguishes electron localization at the anthracene/Ag(111) surface from electron localization at the n-heptane/Ag(111) surface (Figure 5.6). These peaks have binding energies of −0.55 eV, −0.71 eV, and −0.93 eV, corresponding to energy spacings of 1300 ± 300 cm^{-1} and 1700 ± 300 cm^{-1}. This series of peaks appears to be a vibronic progression in a single localized electronic state. Before discussing this assignment, the mechanisms by which a vibronic progression could occur in the TPPE kinetic energy spectrum must be discussed. High

frequency modes can be excited during electron photodetachment and electron transfer, as mentioned in Sections 5.2 and 5.3. How this vibrational excitation can result in a vibronic progression appears schematically in Figures 5.9 and 5.10. For a delocalized state to excite a high frequency vibration during localization, $\Delta\varepsilon = E_{st} - E_{||}$ must exceed the energy of the vibration. As long as readsorption of the emitted quantum of vibration does not occur during photoemission, this will result in a localized peak in the kinetic energy spectrum at the same energy as the localized peak that did not have enough energy to excite a vibration (see Figure 5.10). The emission of a quantum of vibration during localization requires a resonance between a delocalized electronic state and the vibrationally excited electronic state of the localized state. The energy conservation criteria for the emission of a quantum of vibration during photoemission can be more easily achieved due to the continuum of final electronic states. To emit a phonon during photoemission, the photon energy needs to exceed the electron binding energy by at least a quantum of vibration. Since the experimental photon energies exceed the image potential states binding energies by over an eV, the Franck-Condon factor will determine the probability of vibrational excitation during photoemission.

For these reasons, vibrational excitation during photoemission provides a more likely explanation for the appearance of multiple peaks in the photoelectron kinetic energy spectrum. The dynamics of the states in the vibronic progression provide a test of this hypothesis. If the progression results from the localization of a single $k_{||}$ state to multiple vibrational levels, $\Delta\varepsilon$ would be different for each vibrational level. These variations in the $\Delta\varepsilon$ would likely result in significant variation in the localization rates. A series of three different localized electronic states would also have three different $\Delta\varepsilon$, with an equally likely variation in the rate of localization for each state. As shown in Figure 5.11, the highest and lowest kinetic energy peaks in the vibronic progression have the same dynamics, further supporting the conclusion that the series of peaks result from phonon emission during photoemission, not localization.

The probability of exciting a vibration during the photoemission step enters via the Franck-Condon factor between the vibrational wavefunction for an excess electron in a localized state and the vibrational wavefunction for the excess electron in the vacuum [115],

$$P \cong \frac{2\pi}{\hbar}|V_{if}|^2, \tag{5.22}$$

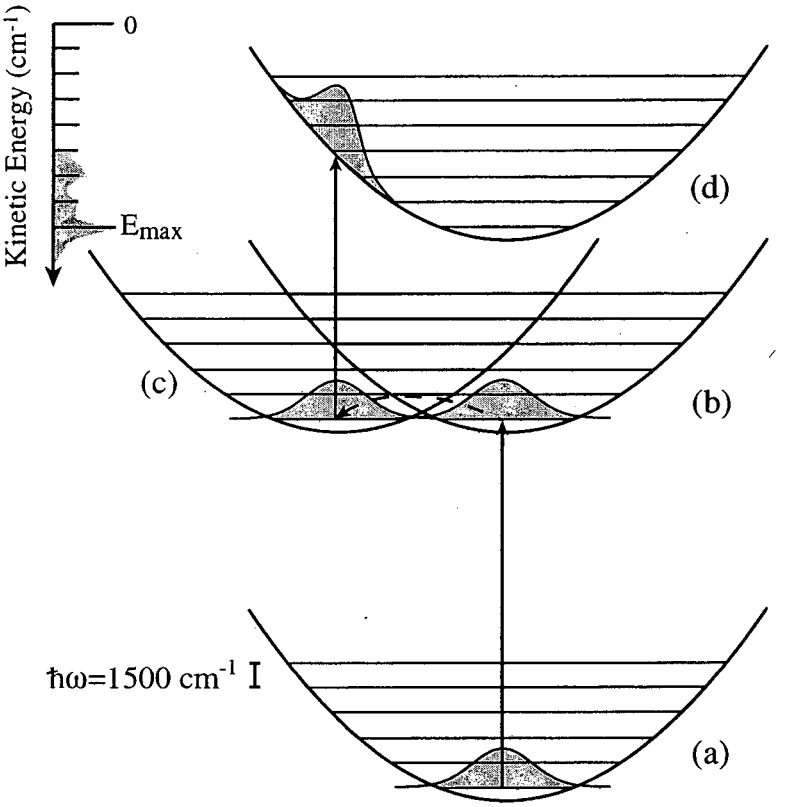

Figure 5.9: Schematic diagram of vibrational excitation during a two photon photoionization. The abscissa represents the vibrational normal coordinate, while the ordinate represents the energy. The vertical lines correspond to photon adsorption and the dashed horizontal line to electron transfer. (a) The electron resides in the metal before excitation. (b) The electron resides in a delocalized $n = 1$ image potential state. Excitation from the metal to the image potential state does not result in vibrational excitation because the equilibrium position for the vibrational coordinate is the same for the electron in the metal and the electron in the image potential state. (c) The electron resides in the vibrational ground state of the localized state. Excitation from the localized state to the final free electron state can result in vibrational excitation because the localized state does have a displaced equilibrium position. (d) The electron has been photoemitted to a free electron in vacuum. The photoelectron kinetic energy spectrum has a 1500 cm^{-1} vibronic progression, where the Franck-Condon factor determines the relative applitudes of the peaks in the vibronic progression. The appearance of this frequency in the vibrational spectrum suggests that a vibration with a frequency of roughly 1500 cm^{-1} functions as a promoter mode for electron localization.

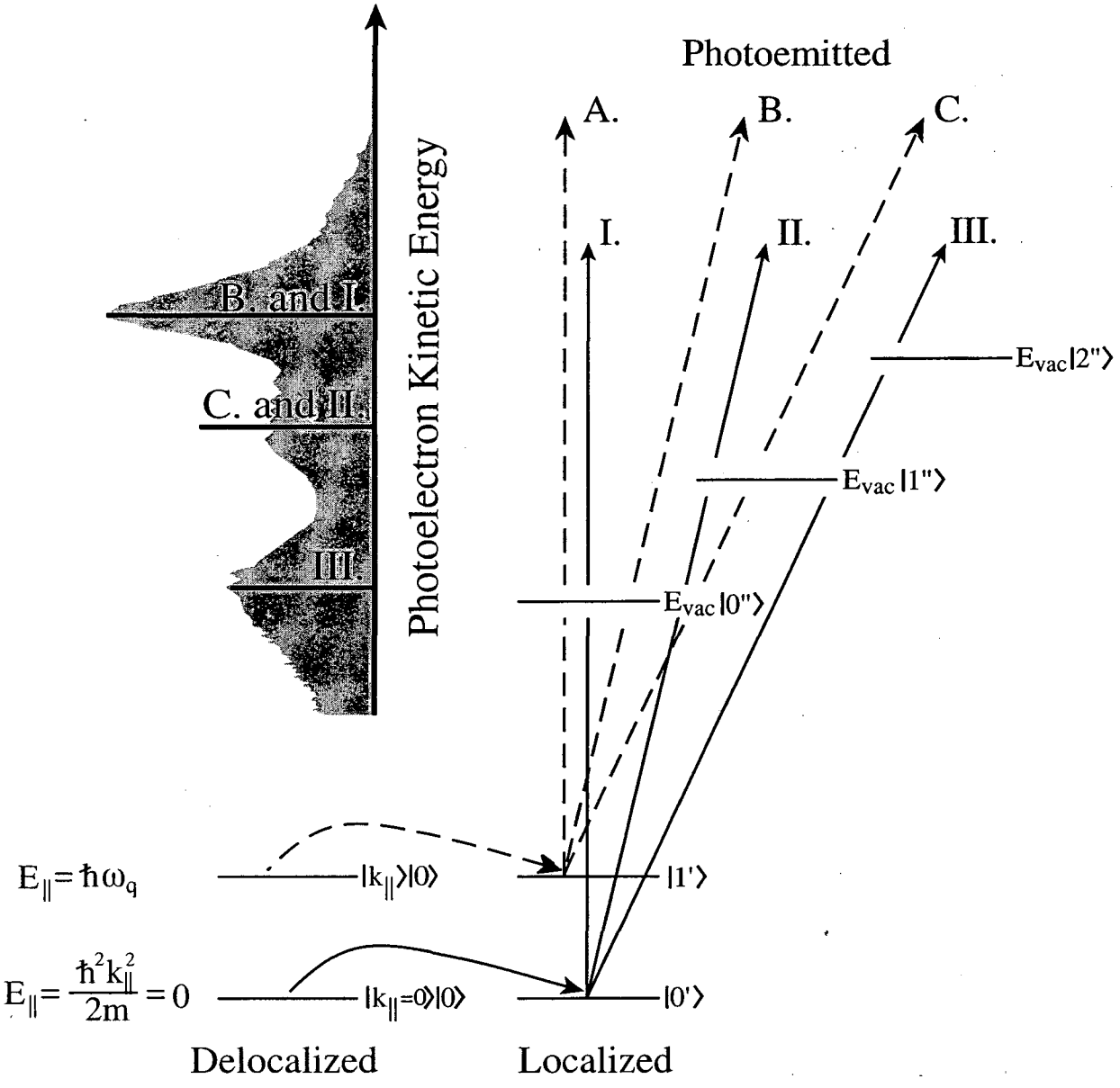

Figure 5.10: Schematic diagram of vibrational excitation during two photon photoemission. Electron localization can result in vibrational excitation $\Delta\varepsilon = E_{st} - E_{||}$ exceeds the energy of the vibration. This will result in an extra peak in the spectrum at an energy above the delocalized band minimum if the quantum of vibration emitted during localization can be adsorbed during photoemission. This process corresponds to mechanism A. The absence of a localized peak above the delocalized band minimum in the experimental kinetic energy spectrum indicates this mechanisms does not occur for anthracene. Vibrational excitation can also occur during photoemission. This process corresponds to mechanisms II., III., and C. These would result in multiple peaks at energies below the bottom of the delocalized band of states, consistent with the anthracene kinetic energy spectrum shown in the Figure.

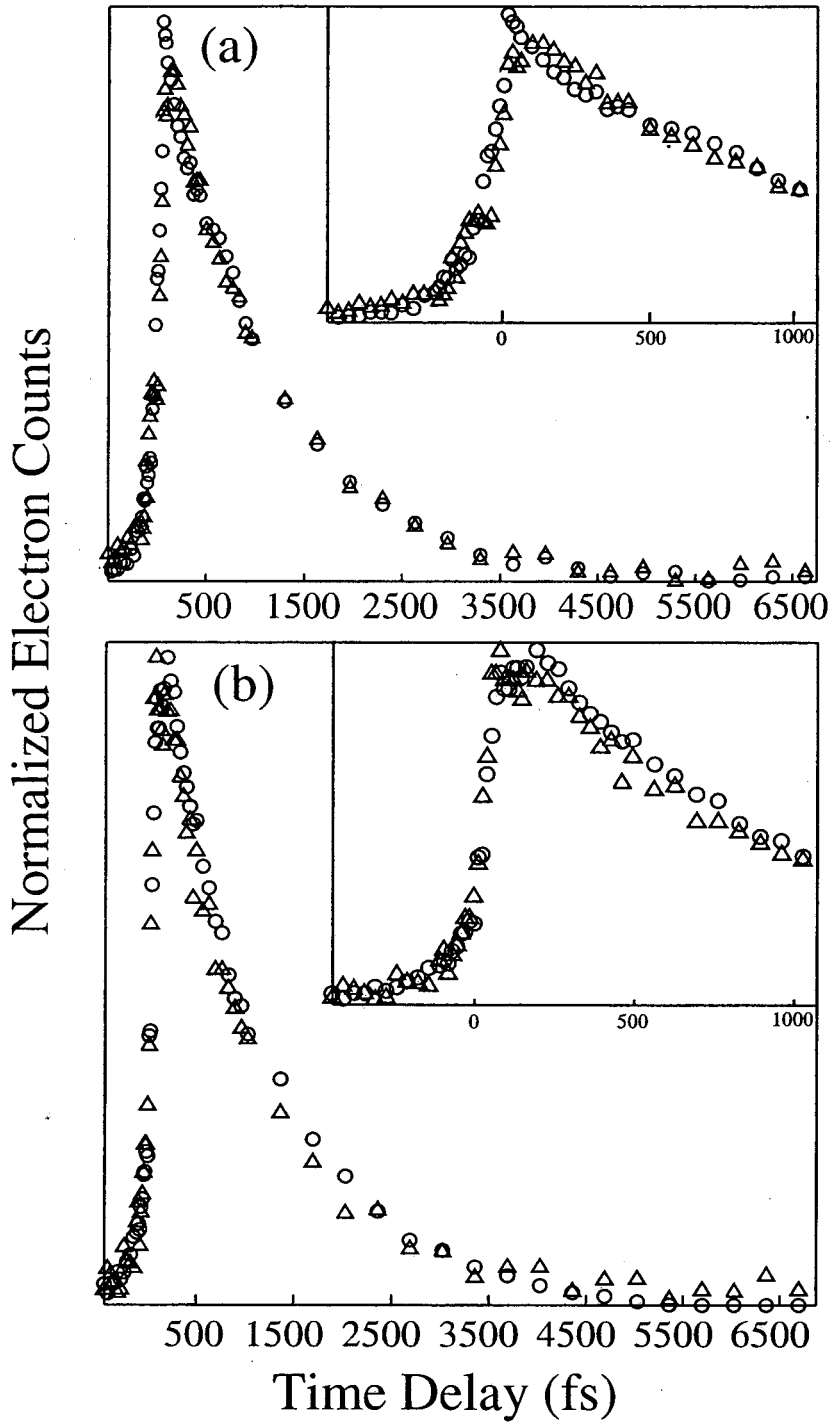

Figure 5.11: Dynamics of the localized states at 20° (a) and 16° (b). The circles correspond to the localized state with the highest kinetic energy and the triangles to the localized state with the lowest kinetic energy. All four traces have the same dynamics.

where

$$V_{if} = \langle n_f | n_i \rangle \langle \phi_f | \mu | \phi_i \rangle. \tag{5.23}$$

The $|n\rangle$ represent the nuclear wavefunctions, $|\phi\rangle$ the electronic wavefunctions, and μ the dipole moment operator. The square of the first term gives the Franck-Condon factor and the latter term the electronic transition moment. Since the equilibrium position for the lattice with a localized electron differs from that without a localized electron, a Franck-Condon progression can be observed. This process appears schematically in Figure 5.9.

The appearance of a vibronic progression indicates the likely importance of a $\approx 1500\,\mathrm{cm}^{-1}$ mode in the localization process. The intensity of the peak that corresponds to the emission of two quanta of vibration significantly exceeds the intensity of the single quantum emission peak, and no three quanta peak appears. The Franck-Condon factor must be larger for the $|\langle 0|2\rangle|^2$ transition, than for the $|\langle 0|1\rangle|^2$ transition. The quantum mechanical reorganization energy of this vibration should be should be on the order of $E_{rq} \approx 3000\,\mathrm{cm}^{-1}$, or larger. The fit of the delocalized states dynamics to the electron transfer theory of Bixon and Jortner uses an $E_{rq} = 3000\,\mathrm{cm}^{-1}$. A similar vibronic progression has also been observed for electron photoemission through an anthracene functionalized molecular layer adsorbed on a metal surface [116]. Descriptions of inner sphere electron transfer in aromatic dye molecules often utilize a $1500\,\mathrm{cm}^{-1}$ mode to account for the influence of ring skeletal modes [117–119].

To indentify the localization exothermicity $\Delta\varepsilon$, the energy of the localized state in the vibrational ground state must be determined. The presence of three localized peaks makes this determination more challenging. Take the $k_{||} = 0$ delocalized state. The series of three peaks would indicate it could resonantly transfer to the vibrational second excited state of the localized state. If no further excitation occured during photoemission, such a process would result in a peak in the photoelectron kinetic energy spectrum with two quanta of energy less than the delocalized $k_{||} = 0$ state. Alternatively, this same state could resonantly transfer to the vibrational ground state, and excite two quanta of vibration during photoemission. Both hypothesized processes produce spectra consistent with those measured experimentally, but give $\Delta\varepsilon$ that differ by roughly a third of an eV. The delocalized state dynamics support the conclusion that vibrational excitation occurs during photoemission.

The population dynamics at 0° and 4° have significant rise times, 350 ± 150 fs

and 200 ± 50 fs, and slow decay dynamics. The decay time at 0° of 1100 ± 200 fs equals the decay time of the localized peaks. The decay dynamics at $E_{||} = 0$ indicate that the localization rate occurs too slowly to be measured. The rise time reflects the appearance of the localized state at energies similar to those of the delocalized states at 0° and 4° as shown in Figure 5.12. The rise in population may also indicate that these states do undergo relaxation within the $n = 1$ band before decaying to the localized state and the metal. The slow localization dynamics at $E_{||} = 0$ can only be described by the theory discussed in Section 5.2 if $\Delta\varepsilon$ approaches zero as $E_{||}$ approaches zero. This corresponds to a small E_{st}. For this to be true, the localized peak with the highest kinetic energy peak must provide the energy of the localized electronic state in the vibrational ground state, resulting in an $E_{st} = -15$ meV. The energy difference between this highest energy localized state and the energy of each $k_{||}$ state determines the electron localization exothermicity, $\Delta\varepsilon$, for that particular delocalized state.

The localized state energy changes as a function of time delay, as shown in Figure 5.12. This shift results from the dynamic reorganization of the anthracene layer. This provides direct access to the classical reorganization energy and dynamics central to electron transfer theory, with the magnitude of the shift providing E_{rc} and the dynamics of the shift provides τ_l. The energy of the delocalized image potential states have no time dependence. This demonstrates that the equilibrium geometry of the adsorbate layer with a delocalized electron does not differ from the geometry without a delocalized electron, as shown in Figure 5.9. The molecular and lattice relaxation that results in localization also causes the time dependence of the localized states energies. At the time of electron excitation from the substrate, the lattice will be undistorted by the excited electrons. The energy difference between the localized state and the $k_{||} = 0$ delocalized state at zero lattice distortion provides the classical reorganization energy, E_{rc}. Thus, by measuring the energy of the delocalized state at $k_{||} = 0$ and the energy of the localized electronic state at zero time delay, the energy of the crossing point between the localized state and the band of delocalized states can be determined. The initial energy of the localized state can be determined directly from the spectrum or by extrapolating the fit at longer time delays back to zero time delay. The spectra give a reorganization energy of $0.08 - 0.12$ eV, while the extrapolation back to time zero give a reorganization energy of $0.10 - 0.18$ eV. The relaxation of the localized state energy fits a single exponential with a time constant of $\tau_l = 190 \pm 40$ fs. The width of the localized state also has significant time dependence, as shown in Figure 5.13. This can also

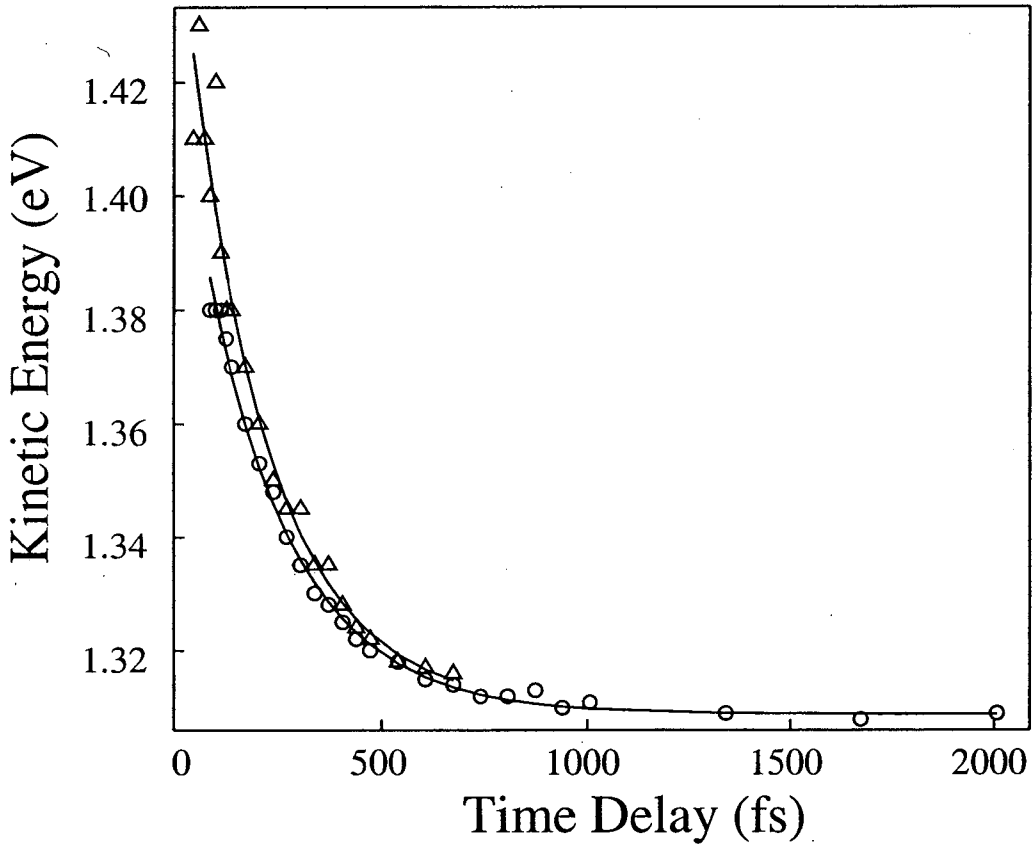

Figure 5.12: Plot of the highest kinetic energy localized state peak maximum versus pump-probe time delay. The triangles correspond to data taken at 24°, while the circles correspond to data taken at 16°. This time dependent energy results from localized state motion along the self-trapping coordinate depicted in Figure 5.7. The lines represent the fits to the data. The energy at zero time delay provides the energy at which the localized state crosses the delocalized band at zero lattice distortion, while the time scale of the energetic shift provides a direct measure of the solvation time, τ_l, utilized in the Bixon-Jortner theory. The fits give an initial energy of 1.45 ± 0.04 eV and an exponential solvation time of 190 ± 40 fs.

Table 5.1: Energy Dependent Dynamics of $n = 1$ at the Anthracene/Ag(111) Interface

Angle	$E_{\|\|}$ (meV)	Rise Time (fs)	Decay Time (fs)
0°	0	350 ± 150	1100 ± 200
4.4°	10	200 ± 50	800 ± 200
8.4°	30	–	200 ± 30
12.4°	71	–	130 ± 15
16.4°	124	–	75 ± 15
20.4°	181	–	50 ± 10
22.4°	222	–	45 ± 10
24.4°	264	–	40 ± 10

be fit to a single exponential of 160 ± 30 fs. Why the peak has a time dependent width has yet to be determined.

The delocalized state population dynamics at multiple angles appear in Figure 5.14, while Table 5.3.2 lists the decay constants. As mentioned above, the decay dynamics of low $k_{||}$ states differ little from those of the localized state, indicating that these delocalized states have a slow rate of localization. For larger values of $E_{||}$, the decay rate increases significantly. Increasing $E_{||}$ from 10 meV to 30 meV, results in a 15 fold increase in the decay rate. This indicates that electron localization represents an efficient decay channel that dominates the delocalized state decay for $E_{||} > 50$ meV. The validity of this hypothesis has been tested by comparing the measured decay dynamics with a theoretical prediction of the electron transfer rate.

The effective fitting of the experimental data to electron transfer theory requires the use of two high frequency modes to eliminate the $\Delta\varepsilon$ dependent oscillations in the localization rate. The electron photodetachment from the gas phase anthracene anion has a single Franck-Condon active vibration, appearing as a 384 cm^{-1} vibronic progression in the photoelectron spectrum. This vibration provides a likely canidate for an electron transfer promoting mode. While only one vibronic progression appears in the photoelectron kinetic energy spectrum, the significant widths of the localized peaks could reflect the presence of lower frequency vibronic structure obscured by inhomogeneous broadening and the instrument energy resolution.

The Bixon and Jortner formulation of electron transfer theory with two quantum mechanical degrees of freedom has been utilized to describe the delocalized state decay

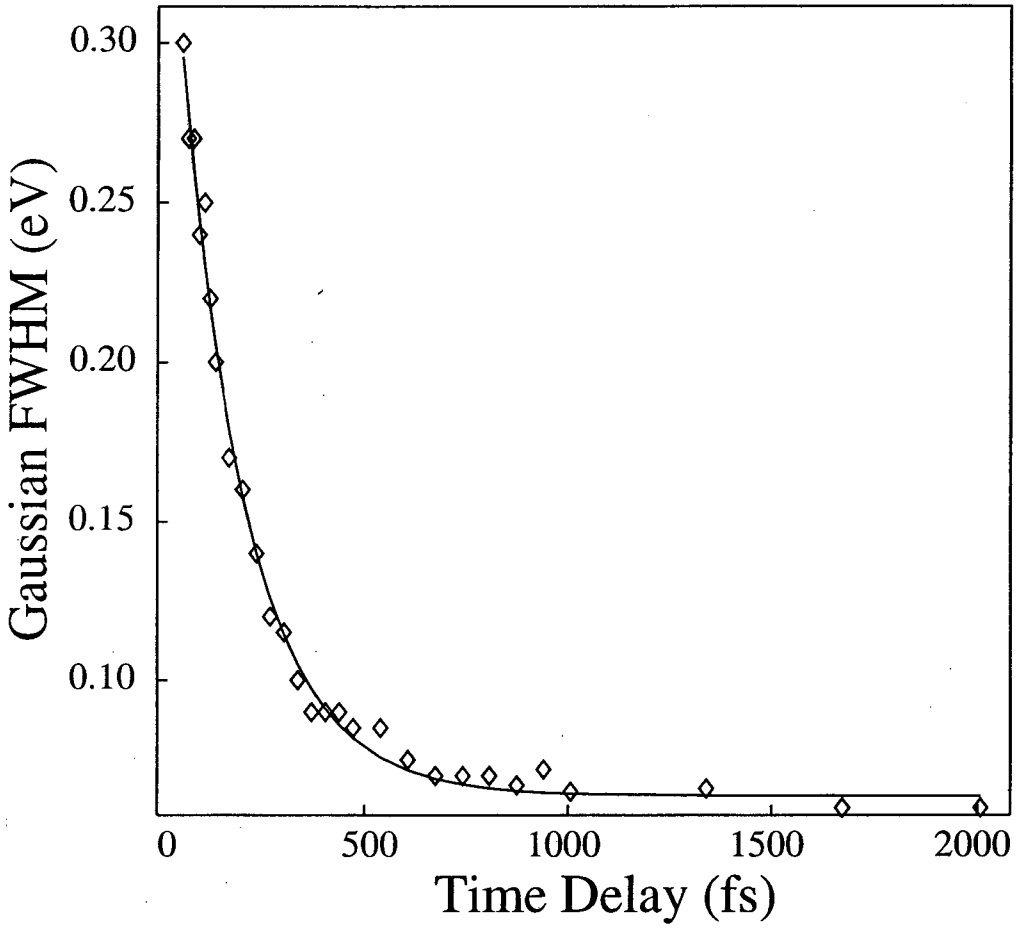

Figure 5.13: Plot of the Gaussian full width at half maximum (FWHM) for the highest kinetic energy localized state at 20°. The diamonds represent the experimental data, while the line corresponds to the fit. The time dependence of the width has an exponential time constant of 160 ± 30 fs. This strongly resembles the energy shift dynamics. The width of the peak should reflect the energetic range of delocalized states that can strongly interact with the localized state. The narrowing of the localized peak indicates that the interaction between the localized state and the delocalized band of states decreases as the lattice distortion increases.

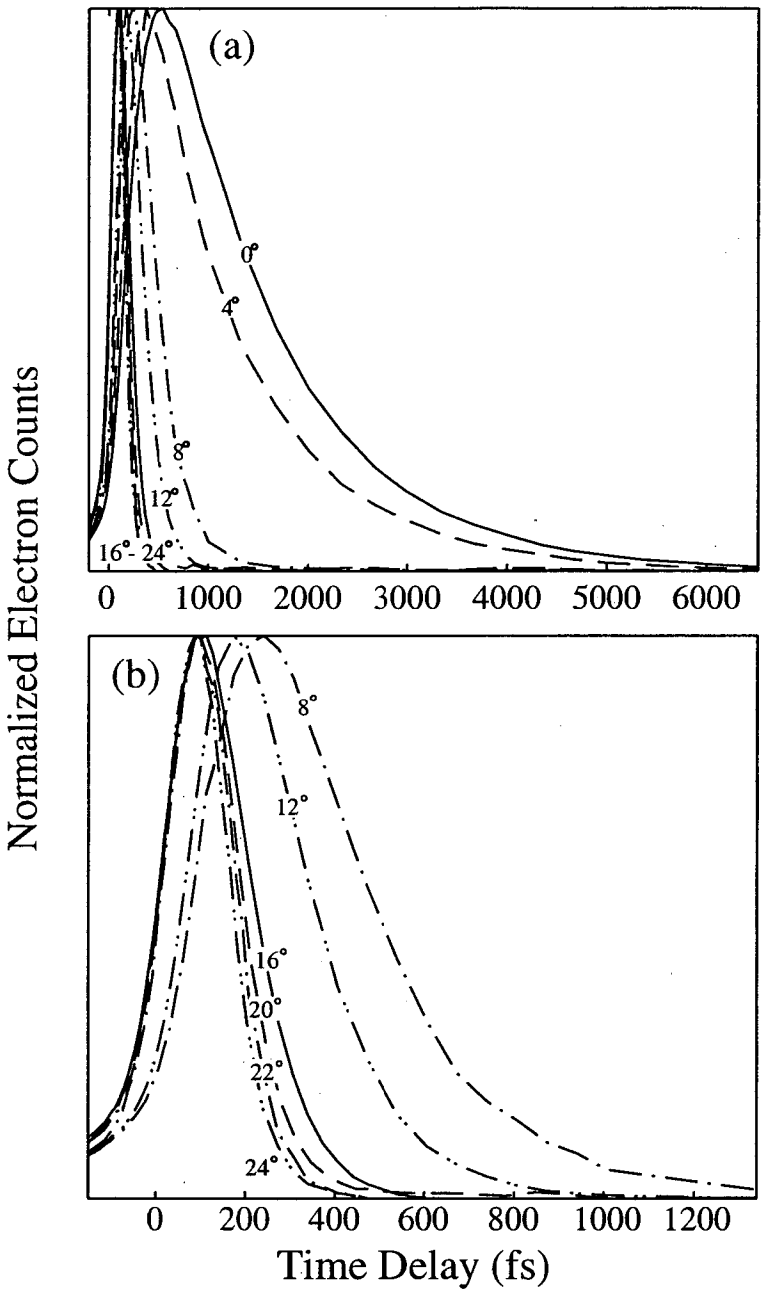

Figure 5.14: Delocalized $n = 1$ dynamics at multiple angles. (a) The decay of $n = 1$ at 0° and 4° proceeds much more slowly than at the higher angles. The delocalized $n = 1$ also exhibits significant rise time at these angles. (b) Dynamics of $n = 1$ at the higher angles only. The lifetimes of the delocalized states at different angles can be found in Table 5.3.2.

dynamics. As discussed above, the classical reorganization energy, the dielectric relaxation time, as well as the frequency and reorganization energy of one of the quantum modes have been measured with time and angle resolved TPPE. A reasonable choice for a second frequency has been choosen from the literature. Of the parameters allowed to vary, the electronic coupling strength, H_{fs}, has the most significant influence on the results of the calculation. The calculated and experimental rates appear in Figure 5.15 and the parameters used in the fit can be found in the caption. While a reasonable agreement has been achieved, the experimental rate consistently exceeds the calculated rate. This difference in theory and experiment may result from the intraband relaxation ignored in the calculated rate.

Two other experimental results deserve mention as well. The population dynamics of the localized states have also been measured, and appear in Figure 5.11. Suprisingly, the localized states dynamics can be fit without a rise time. For time delays of less than 100 fs, the photoelectron kinetic energy spectra appears featureless in the energetic range of the localized state as shown in Figure 5.6. While this makes the extraction of a rise time from the experimental dynamics difficult, a rise time of 100 fs would be clearly measurable. The $k_{||}$ dependence of the localized peak intensities also warrant mention. The localized peak with the highest kinetic energy has an intensity that decreases with increasing $k_{||}$, while the two lower states have intensities that increase with increasing $k_{||}$. These lower kinetic energy peaks can only be observed in spectra above 4°. No satisfactory explanation for this behavior has yet to be identified.

5.4 Conclusion

The experimental characterization of two dimensional localization at the anthracene/Ag(111) interface has been initiated. Delocalized image potential states excited with large parallel momentum relax on a 100 fs time scale to either low $k_{||}$ delocalized image potential states or a localized states. These highly excited electrons strongly couple to the layer vibrations, and energetically relax via the emission of phonons. The appearance of a vibronic progression in the localized state indicates that the localized electrons interact strongly with a high frequency vibration of $\approx 1500\ \mathrm{cm}^{-1}$. This would appear to be a ring breathing mode of anthracene. A similar vibronic progression has been seen for electron transmission through an anthracene functionalized monolayer [116], and descriptions of inner sphere electron transfer in aromatic dye molecules often utilize a $1500\ \mathrm{cm}^{-1}$ mode to

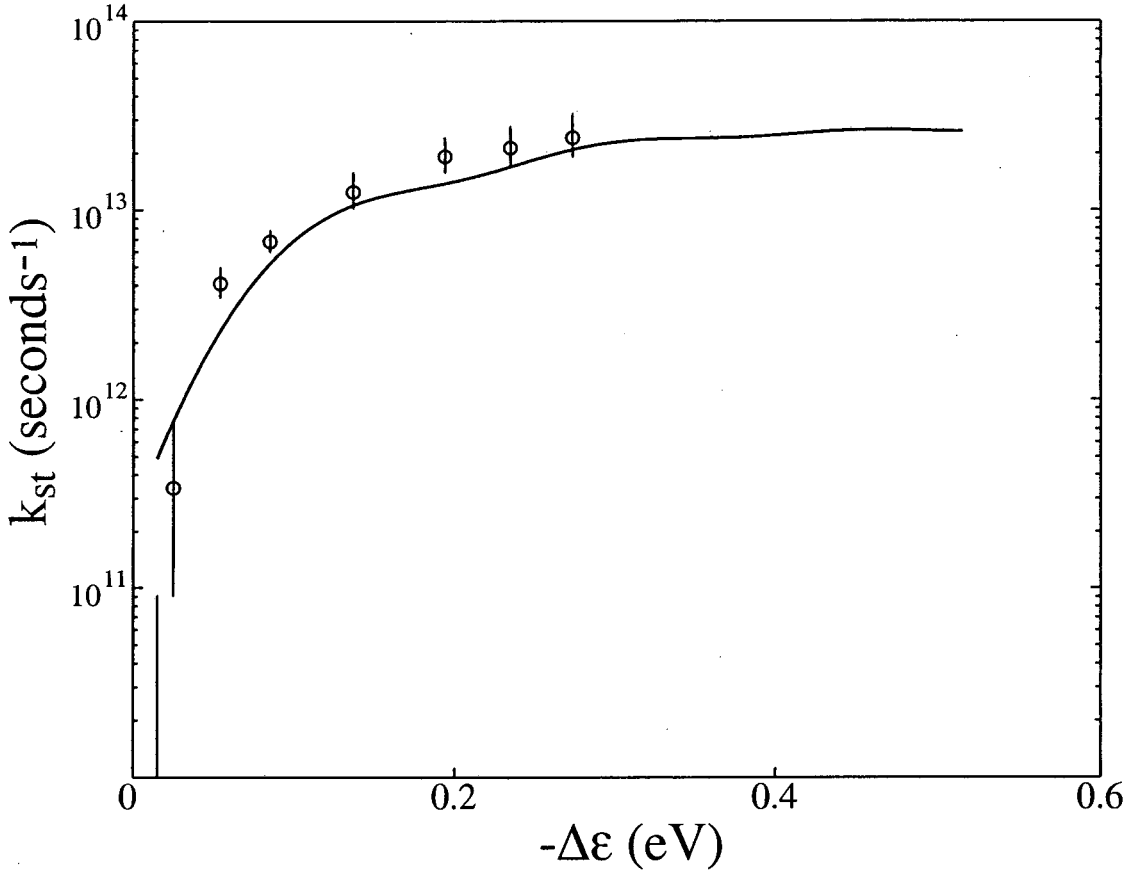

Figure 5.15: Delocalized state decay rate as a function of localization exothermicity, $-\Delta\varepsilon$. The circles correspond to the experimental data, while the line represents the calculated electron transfer rate. The calculations utilized the theory of Bixon and Jortner [111], adapted to include two high frequency vibrations. The fit used the following parameters: $H_{if}^2 = 0.09$ eV, $\tau_l = 150$ fs, $E_{rc} = 0.12$ eV, $T = 110$ K, $\omega_1 = 1300\,\mathrm{cm}^{-1}$, $E_{rq}^{(}1) = 0.32$ eV, $\omega_2 = 380\,\mathrm{cm}^{-1}$, and $E_{rq}^{(}2) = 0.07$ eV. A discussion of the implementation of the theory can be found in the text.

account for the influence of ring skeletal modes on the electron transfer rate [117–119]. Once the electron localizes, the energy and Gaussian width of the state decreases exponentially. This provides a direct measure of the electron dynamics along the classical self-trapping coordinate, with the magnitude of the shift giving the classical reorganization energy and the exponential time constant giving the dielectric relaxation time.

Electron transfer theory has been used to describe the dynamics of electron localization. Many of the important parameters in the theory can be directly accessed with time and angle resolved TPPE. While the population dynamics of the delocalized image potential state band and the localized state provide the central measurement, the appearance of a vibronic progression in the kinetic energy spectrum and the time dependent energy of the localized state greatly reduce the number of unknown parameters needed for the theory.

The Bixon and Jortner formulation of electron transfer theory has been utilized to understand the decay dynamics of the delocalized $n = 1$ image potential band. Three nuclear coordinates must be used for a reasonable fit to be acquired, two corresponding to high frequency vibrations and the third being the classical reorganization coordinate. The frequency of the second vibration could not be accessed from the experiment directly. The fit shown in Figure 5.15 used a second frequency of 384 cm^{-1}, The frequency of the vibronic progression observed in the photoelectron detachment spectrum for the anthracene anion [35]. While a second high frequency vibration must be used to get an electron transfer rate that does not oscillate, a reasonable fit could be achieved for a wide range of vibrational frequencies and reorganization energies for this coordinate. The fit of the data suggests that electron localization at the anthracene/Ag(111) interface occurs adiabatically.

Two issues remain unresolved at present; the absence of a rise time in the localized state dynamics and the use of a two state electron transfer theory to describe the transition from a continuum to a single localized resonance. For delocalized states with low $E_{||}$, such as those accessed at 0° and 4°, the rate of electron localization occurs slowly enough that a rise in the localized state population should be observable, but no such rise occurs. The adsence of a rise time may indicate that these low $E_{||}$ states make a small contribution to the total localized state signal. Under these conditions, the amplitude of the rise would be small and difficult to detect. For an exothermic two state electron transfer reaction, once the electron crosses from the donor to the acceptor, back electron transfer to the donor will occur with a lower probability due to the larger energy barrier. For the electron transfer from a continuum to a resonance, the electron can undergo numerous electron transfers between

the localized resonance and the continuum of delocalized states, until the distortion of the lattice reaches the critical point where a localized state can be formed. While the two state theory may provide a reasonable estimate of the rate for the first electron transfer, the back transfer of the localized electron to a different continuum state can occur.

Bibliography

[1] M. Bonn, S. Funk, C. Hess, D.N. Denzler, C. Stampfl, M. Scheffler, M. Wolf, and G. Ertl. *Science*, 285(5430):1042, 1999.

[2] W. Ho. *J. Phys. Chem.*, 100(31):13050, 1996.

[3] D.G. Busch and W. Ho. *Phys. Rev. Lett.*, 77(7):1338, 1996.

[4] W. Ho. *Acc. Chem. Res.*, 31(9):567, 1998.

[5] J.A. Prybyla, H.W.K. Tom, and G.D. Aumiller. *Phys. Rev. Lett.*, 68(4):503, 1992.

[6] Q.-B. Lu and T.E. Madey. *Phys. Rev. Lett.*, 82(20):4122, 1999.

[7] E.P. Marsh, T.L. Gilton, W. Meier, M.R. Schneider, and J.P. Cowin. *Phys. Rev. Lett.*, 61(23):2725, 1988.

[8] F. Budde, T.F. Heinz, M.M.T. Loy, J.A. Misewich, F. de Rougemont, and H. Zacharias. *Phys. Rev. Lett.*, 66(23):3024, 1991.

[9] J.A. Misewich, A. Kalamarides, T.F. Heinz, U. Höfer, and M.M.T. Loy. *J. Chem. Phys.*, 100(1):736, 1994.

[10] M. Brandbyge, P. Hedegård, T.F. Heinz, J.A. Misewich, and D.M. Newns. *Phys. Rev. B*, 52(8):6042, 1995.

[11] Y.H. Huang, C.T. Rettner, D.J. Auerbach, and A.M. Wodtke. *Science*, 290(5489):111, 2000.

[12] I.H. Campbell, T.W. Hagler, D.L. Smith, and J.P. Ferraris. *Phys. Rev. Lett.*, 76(11):1900, 1996.

[13] Yu.N. Gartstein and E.M. Conwell. *Chem. Phys. Lett.*, 255(1-3):93, 1996.

[14] E.M. Conwell and M.W. Wu. *Appl. Phys. Lett.*, 70(14):1867, 1997.

[15] M.N. Bussac, D. Michoud, and L. Zuppiroli. *Phys. Rev. Lett.*, 81(8):1678, 1998.

[16] J.C. Scott and G.G. Malliaras. *Chem. Phys. Lett.*, 299(2):115, 1999.

[17] R.H. Friend et al. *Nature*, 397(6715):121, 1999.

[18] T. Kugler, M. Lögdlund, and W.R. Salaneck. *Acc. Chem. Res.*, 32(3):225, 1999.

[19] J.H. Schön, Ch. Kloc, E. Bucher, and B. Batlogg. *Nature*, 403(6768):408, 2000.

[20] J.H. Schön, S. Berg, Ch. Kloc, and B. Batlogg. *Science*, 287(5455):1022, 2000.

[21] Y. Shen, M.W. Klein, D.B. Jacobs, J.C. Scott, and G.G. Malliaras. *Phys. Rev. Lett.*, 86(17):3867, 2001.

[22] W.R. Merry. *Image Potential States at Dielectric-Metal Interfaces.* PhD thesis, University of California at Berkeley, 1992.

[23] P.M. Echenique and J.B. Pendry. *Prof. Surf. Sci.*, 32(2):111, 1989.

[24] J.D. McNeill. *Ultrafast Dynamics of electrons at Interfaces.* PhD thesis, University of California at Berkeley, 1999.

[25] Th. Fauster, C. Reuß, I.L. Shumay, and M. Weinelt. *Chem. Phys.*, 251(1-3):111, 2000.

[26] I.L. Shumay, U. Höfer, U. Thomann, W. Wallauer, and Th. Fauster. *Phys. Rev. B*, 58(20):13974, 1998.

[27] J.D. McNeill, R.L. Lingle, N.-H. Ge, C.M. Wong, and C.B. Harris. *Phys. Rev. Lett.*, 79(23):4645, 1997.

[28] K.J. Gaffney, C.M. Wong, S.H. Liu, A.D. Miller, , J.D. McNeill, and C.B. Harris. *Chem. Phys.*, 251(1-3):99, 2000.

[29] E.A. Silinsh and V. Čápek. *Organic Molecular Crystals: Interactions, Localization, and Transport Phenomena.* American Institute of Physics, New York, New York, 1994.

[30] M. Pope, P. Magnante, and H.P. Kallmann. *J. Chem. Phys.*, 38(8):2042, 1963.

[31] J.H. Schön, Ch. Kloc, and B. Batlogg. *Nature*, 406(6797):702, 2000.

[32] J.H. Schön, Ch. Kloc, A. Dodabalupur, and B. Batlogg. *Science*, 289(5479):599, 2000.

[33] J.H. Schön, Ch. Kloc, and B. Batlogg. *Science*, 288(5475):2338, 2000.

[34] P.D. Burrow, J.A. Michejda, and K.D. Jordan. *J. Chem. Phys.*, 86(1):9, 1987.

[35] J. Schiedt and R.Weinkauf. *Chem. Phys. Lett.*, 266(1-2):201, 1997.

[36] C. Kittel. *Introduction to Solid State Physics.* Wiley, New York, New York, 1996.

[37] J.H. Schön, Ch. Kloc, and B. Batlogg. *Phys. Rev. Lett.*, 86(17):3843, 2001.

[38] E.A. Silinsh, A. Klimkāns, S. Larsson, and V. Čápek. *Chem. Phys.*, 198(3):311, 1995.

[39] V.M. Kenkre, J.D. Andersen, D.H. Dunlap, and C.B. Duke. *Phys. Rev. Lett.*, 62(10):1165, 1989.

[40] M. Lee, J.H. Schön, Ch. Kloc, and B. Batlogg. *Phys. Rev. Lett.*, 86(5):862, 2001.

[41] J.D. Jackson. Private communication.

[42] M.W. Cole. *Phys. Rev. B*, 3(12):4418, 1971.

[43] E.W. Plummer and W. Eberhardt. *Adv. Chem. Phys.*, 49:533, 1982.

[44] N.V. Smith and D.P. Woodruff. *Prog. Surf. Sci.*, 21(4):295, 1986.

[45] H. Petek and S. Ogawa. *Prog. Surf. Sci.*, 56(4):239, 1998.

[46] E. Knoesel, A. Hotzel, and M. Wolf. *J. Electron Spectrosc.*, 88:577, 1998.

[47] U. Höfer, I.L. Shumay, Reuß, U. Thomann, W. Wallauer, and Th. Fauster. *Science*, 277(5331):1480, 1997.

[48] C.M. Wong. *Femtosecond Studies of Interband and Intraband Electron Dynamics at Dielectric-Metal Interfaces.* PhD thesis, University of California at Berkeley, 2000.

[49] F.A. Cotton. *Chemical Applications of Group Theory.* Wiley, New York, New York, 1990.

[50] J.D.E. McIntyre. in: Advances in Electrochemistry and Electrochemical Engineering. Wiley, New York, New York, 1973. edited by P. Delahay and C.W. Tobias.

[51] R. Haight. *Surf. Sci. Reports*, 21(8):277, 1995.

[52] S. Ogawa, H. Nagano, and H. Petek. *Phys. Rev. B*, 55(16):10869, 1997.

[53] H. Petek, H. Nagano, and S. Ogawa. *Phys. Rev. Lett.*, 83(4):832, 1999.

[54] E. Knoesel, A. Hotzel, and M. Wolf. *Phys. Rev. B*, 57(20):12812, 1998.

[55] M. Aeschlimann, M. Bauer, S. Pawlik, R. Burgermeister, D. Oberli, and H.C. Siegmann. *Phys. Rev. Lett.*, 79(25):5158, 1997.

[56] S. Ogawa, H. Nagano, and H. Petek. *Phys. Rev. Lett.*, 78(7):1339, 1997.

[57] H. Petek, A.P. Heberle, W. Nessler, H. Nagano, S. Kubota, S. Matsunami, N. Moriya, and S. Ogawa. *Phys. Rev. Lett.*, 79(23):4649, 1997.

[58] S. Ogawa, H. Nagano, and H. Petek. *Phys. Rev. Lett.*, 82(9):1931, 1999.

[59] H. Petek, M.J. Weida, H. Nagano, and S. Ogawa. *Science*, 288(5470):1402, 2000.

[60] L. Bartels, G. Meyer, K.-H. Rieder, D. Velic, E. Knoesel, A. Hotzel, M. Wolf, and G. Ertl. *Phys. Rev. Lett.*, 80(9):2004, 1998.

[61] M. Wolf, A. Hotzel, E. Knoesel, and D. Velic. *Phys. Rev. B*, 59(8):5926, 1999.

[62] Ch. Reuß, I.L. Shumay, U. Thomann, M. Kutschera, M. Weinelt, and Th. Fauster. *Phys. Rev. Lett.*, 82(1):153, 1999.

[63] Th. Fauster. Private Communication.

[64] C.B. Harris, N.-H. Ge, R.L. Lingle, J.D. McNeill, and C.M. Wong. *Ann. Rev. Phys. Chem.*, 48:711, 1997.

[65] R.L. Lingle, N.-H. Ge, R.E. Jordan, J.D. McNeill, and C.B. Harris. *Chem. Phys.*, 205(1-2):191, 1996.

[66] N.-H. Ge, C.M Wong, R.L. Lingle, J.D. McNeill, K.J. Gaffney, and C.B. Harris. *Science*, 279(5348):202, 1998.

[67] N.-H. Ge. *Ultrafast Studies of Electron Dynamics at Metal-Dielectric Interfaces.* PhD thesis, University of California at Berkeley, 1998.

[68] Ph. Avouris and J.E. Demuth. *J. Chem. Phys.*, 75(10):4783, 1981.

[69] R. Dudde, K.-H. Frank, and E.-E. Koch. *Surf. Sci.*, 225(3):267, 1990.

[70] L.E. Firment and G.A. Somorjai. *Surf. Sci.*, 84(2):275, 1979.

[71] M. Xi, M.X. Yang, S.K. Jo, B.E. Bent, and P. Stevens. *J. Chem. Phys.*, 101(10):9122, 1994.

[72] K.-H. Frank, P. Yannoulis, and R. Dudde. *J. Chem. Phys.*, 89(12):7569, 1988.

[73] P. Yannoulis, K.-H. Frank, and E.-E. Koch. *Surf. Sci.*, 241(3):325, 1991.

[74] D. Velic, A. Hotzel, M. Wolf, and G. Ertl. *J. Chem. Phys.*, 109(20):9155, 1998.

[75] W.R. Merry, R.E. Jordan, D.F. Padowitz, and C.B. Harris. *Surf. Sci.*, 295(3):393, 1993.

[76] X.L. Zhou, M.E. Castro, and J.M. White. *Surf. Sci.*, 238(1-3):215, 1990.

[77] T. Munakata, T. Sakashita, M. Tsukakoshi, and J. Nakamura. *Chem. Phys. Lett.*, 271(4-6):377, 1997.

[78] A.B. Anderson, M.R. McDevitt, and F.L. Urbach. *Surf. Sci.*, 146(1):80, 1984.

[79] H.F. Wang, G. Dutton, and X.Y. Zhu. *J. Phys. Chem. B*, 104(44):10332, 2000.

[80] A. Baltuška, M.F. Emde, M.S. Pshenichnikov, and D.A. Wiersma. *J. Phys. Chem. A*, 103(49):10065, 1999.

[81] S. Mukamel. *Principles of Nonliner Optical Spectroscopy.* Oxford University Press, New York, New York, 1995.

[82] J.T. Fourkas and M. Berg. *J. Chem. Phys.*, 98(10):7773, 1993.

[83] J. Ma, D. Vanden Bout, and M. Berg. *J. Chem. Phys.*, 103(21):9146, 1995.

[84] E.V. Chulkov, I. Sarría, V.M. Silkin, J.M. Pitarke, and P.M. Echenique. *Phys. Rev. Lett.*, 80(22):4947, 1998.

[85] J. Osma, I. Sarría, J.M. Pitarke, and P.M. Echenique. *Phys. Rev. B*, 59(16):10591, 1999.

[86] K.J. Gaffney, S.H. Liu, A.D. Miller, P. Szymanski, and C.B. Harris. *J. Chin. Chem. Soc.*, 47(4A):759, 2000.

[87] J.D. McNeill, R.L. Lingle, R.E. Jordan, D.F. Padowitz, and C.B. Harris. *J. Chem. Phys.*, 105(9):3883, 1996.

[88] A. Hotzel G. Moos, K. Ishioka, M. Wolf, and G. Ertl. *Appl. Phys. B*, 68(3):615, 1999.

[89] P.L. de Andres, P.M. Echenique, and F. Flores. *Phys. Rev. B*, 39(14):10356, 1989.

[90] A. Goldmann, W. Altmann, and V. Dose. *Solid State Commun.*, 79(6):511, 1991.

[91] Y.L. Xiao and D.E. Williams. *Acta Cryst. A*, 49(1):1, 1993.

[92] D.R. Lide, editor. *CRC Handbook of Chemistry and Physics.* CRC Press, Boca Raton, Florida, 1990-1991.

[93] Y. Nakato, M. Ozaki, and H. Tsubomura. *J. Phys. Chem.*, 76(15):2105, 1972.

[94] K. Ishioka, C. Gahl, and M. Wolf. *Surf. Sci.*, 454:73, 2000.

[95] C. Gahl, K. Ishioka, Q. Zhong, A. Hotzel, and M. Wolf. *Faraday Discuss.*, 117:191, 2000.

[96] R.W. Munn and D.F. Williams. *J. Chem. Phys.*, 59(4):1742, 1973.

[97] R.W. Munn, J.R. Nicholson, H.P. Schwob, and D.F. Williams. *J. Chem. Phys.*, 58(9):3828, 1973.

[98] P. Avouris and B.N.J. Persson. *J. Phys. Chem.*, 88(5):837, 1984.

[99] B.N.J. Persson and P. Avouris. *J. Chem. Phys.*, 79(10):5156, 1983.

[100] R.L. Lingle, D.F. Padowitz, R.E. Jordan, J.D. McNeill, and C.B. Harris. *Phys. Rev. Lett.*, 72(14):2243, 1994.

[101] Z.H. Liu and B.J. Berne. *J. Chem. Phys.*, 99(11):9054, 1993.

[102] D. Chandler and K. Leung. *Ann. Rev. of Phys. Chem.*, 45:557, 1994.

[103] K. Giesen adn F. Hage, F.J. Himpsel, H.J. Riess, W. Steinmann, and N.V. Smith. *Phys. Rev. B*, 35(3):975, 1987.

[104] R. Fischer, Th. Fauster, and W. Steinmann. *Phys. Rev. Lett.*, 48(20):15496, 1993.

[105] R.A. Marcus and N. Sution. *Biochim. Biophys. Acta*, 811(3):265, 85.

[106] B. Bagchi and N. Gayathri. *Adv. Chem. Phys.*, 107:1, 1999.

[107] P.F. Barbara, T.J. Meyer, and M.A. Ratner. *J. Phys. Chem.*, 100(31):13148, 1996.

[108] N.R. Kestner, J. Logan, and J. Jortner. *J. Phys. Chem.*, 78(21):2148, 1974.

[109] J. Ulstrup and J. Jortner. *J. Chem. Phys.*, 63(10):4358, 1975.

[110] I. Rips and J. Jortner. *J. Chem. Phys.*, 87(4):2090, 1987.

[111] J. Jortner and M. Bixon. *J. Chem. Phys.*, 88(1):167, 1987.

[112] T. Holstein. *Ann. Physics*, 8:325,343, 1959.

[113] A.A. Stuchebrukhov and X.Y. Song. *J. Chem. Phys.*, 101(11):9354, 1994.

[114] A. Hotzel, M. Wolf, and J.P. Gauvacq. *J. Phys. Chem.*, 104(35):8438, 2000.

[115] R.E. Ballard. *Photoelectron Spectroscopy and Molecular Orbital Theory.* Wiley, New York, New York, 1978.

[116] K. Ray, A. Shanzer, D.H. Waldeck, and R. Naaman. *Phys. Rev. B*, 60(19):13347, 1999.

[117] P.F. Barbara, G.C. Walker, and T.P. Smith. *Science*, 256(5059):975, 1992.

[118] R. Doolen and J.D. Simon. *J. Am. Chem. Soc.*, 116(3):1155, 1994.

[119] G.C. Walker, E. Åkesson, A.E. Johnson, N.E. Levinger, and P.F. Barbara. *J. Phys. Chem.*, 96(9):3728, 1992.

Ernest Orlando Lawrence Berkeley National Laboratory
One Cyclotron Road | Berkeley, California 94720

Prepared for the U.S. Department of Energy under Contract No. DE-AC03-76SF00098